The Fundamental Interactions Between Hydrogen and group III-VI and IV-VI van der Waals Crystals

Thesis submitted to the University of Nottingham for the degree of
Doctor of Philosophy, September 2022.

James Felton

14342319

Supervised by

Amalia Patanè
Gavin Walker
Zakhar Kudrynskyi

Signature ____________________

Date: 28 / 09 / 2022

Abstract

Eighteen years since the exfoliation of graphene was first demonstrated, van der Waals (vdW) materials have attracted incredible fundamental and applied research interest. The sustained level of interest can be attributed to the unique properties and the diversity of vdW crystals, which can be readily exfoliated via the simple method first used for graphene. Over the same period, a renewed wave of hydrogen research has emerged with the aim of reducing greenhouse gas emissions. As such, the two fields have often intersected, with the properties of vdW materials often well suited to applications in hydrogen storage, sensing, generation and purification. This PhD considers the fundamental interactions of vdW materials with hydrogen. Specifically, the focus of this work is on the interactions with the vdW semiconductors SnS_2, SnS, γ-InSe and ϵ-GaSe. It was found that SnS_2 can be converted to SnS upon hydrogen exposure, producing a heterostructure with surprising uniformity and a step-like interface. Exposure of γ-InSe to H-ions modifies its optical and vibrational properties, whilst theoretical studies reveal an exciting modification to the phonon modes upon H_2 incorporation. Finally, water exposed ϵ-GaSe is partially oxidised, modifying its electronic band structure, relevant to solar water splitting applications. These results are of fundamental interest and relevant to both hydrogen and semiconductor technologies, ranging from engineered vdW heterostructures and optoelectronics, to hydrogen storage and generation.

Acknowledgements

This PhD is part of the Fuel Cells and their Fuels centre for doctoral training, funded by the Engineering and Physical Sciences Research Council [grant number EP/L015749/1].

I would like to thank my supervisors Prof. Amalia Patanè, Dr. Zakhar Kudrynskyi and Prof. Gavin Walker for their guidance, advice and assistance throughout the course of this PhD.

Collaboration has been a vital component of this PhD. As such, I would like to acknowledge and thank some of the individuals who have assisted in its completion: Elena Blundo, Prof. Antonio Polimeni and Dr. Giorgio Pettinari (Sapienza University of Rome) have all been of great help in conducting exposures of both InSe and SnS_2 to hydrogen ions and the study of some of their optoelectronic properties; Prof. Zakhar Kovalyuk (National Academy of Sciences of Ukraine) for the growth of SnS_2, InSe and GaSe used over the course of this PhD; Dr. Sanliang Ling (University of Nottingham) for providing DFT simulations of SnS_2 and InSe systems; Dr. Vladimir Korolkov (Park Systems) for the AFM measurements of large area GaSe samples; similarly, Dr. Jonathan Bradford (University of Nottingham) for the AFM on SnS_2 and GaSe samples. NAP-XPS studies of GaSe have been conducted thanks to the assistance of Jack Hart and Dr. James O'Shea (University of Nottingham). Dr. Timothy Cooper, Dr. Matthew Wadge and Prof. David Grant (University of Nottingham) have made available a system in Nottingham for the exposure to hydrogen at low pressures. Dr. Fumin Huang and Anna Casey (Queen's University Belfast) have provided large area GaSe samples used for oxidation studies. The facilities at the Nanoscale and Microscale Research Centre (University of Nottingham) have been used for the study of materials via SEM, TEM and XPS.

Contents

List of Publications

James Felton, Elena Blundo, Sanliang Ling, Joseph Glover, Zakhar R. Kudrynskyi, Oleg Makarovsky, Zakhar D. Kovalyuk, Elena Besley, Gavin Walker, Antonio Polimeni, Amalia Patanè "The Interaction of Hydrogen with the van der Waals Crystal γ-InSe." *Molecules 25*, no. 11 (2020): 2526.

Zhuo Yang, Xueting Wang, James Felton, Zakhar Kudrynskyi, Masaki Gen, Toshihiro Nomura, Xinjiang Wang, Laurence Eaves, Zakhar D Kovalyuk, Yoshimitsu Kohama, Lijun Zhang, Amalia Patanè "Heavy carrier effective masses in van der Waals semiconductor Sn(SeS) revealed by high magnetic fields up to 150 T. "*Physical Review B 104*, no. 8 (2021): 085206.

James Felton, Elena Blundo, Zakhar Kudrynskyi, Sanliang Ling, Jonathan Bradford, Giorgio Pettinari, Timothy Cooper, Matthew Wadge, Zakhar Kovalyuk, Antonio Polimeni, Peter Beton, David Grant, Gavin Walker, Amalia Patanè. "Hydrogen-Induced Conversion of SnS_2 into SnS or Sn: A Route to Create SnS_2/SnS Heterostructures." *Small*, Jul no. 4 (2022): 2202661.

Chapter 1

Introduction: Motivation, Literature & Scope

This chapter provides the context in which the PhD was conducted. Specifically, the significance of hydrogen and layered van der Waals (vdW) materials, the rationale behind investigating their interactions and previous studies on the topic. As such, this chapter is divided into three sections. The first section describes the motivation for the work, addressing the fundamental and applied interest in the topic. The second section considers the literature on previous theoretical and experimental works in this field. The third section discusses the scope of the investigations for each of the considered vdW materials and introduces the thesis structure.

Contents

1.1 Motivation

The establishment of a hydrogen economy is one response to the need to decarbonise the sectors of energy, transportation, steel production and ammonia production, together contributing to 58.8 % of global greenhouse gas emissions (Change (2014); Levi et al. (2020); David (2020)). These emissions can be averted by the introduction of green hydrogen as an energy vector in the energy and transportation sectors, as a feedstock for the reduction of iron ore and by the substitution of green hydrogen for grey hydrogen in the Haber-Bosch process (IEA (2019)). However, realising these potential applications requires technological innovations in: fuel cells, hydrogen storage, hydrogen purification, hydrogen production and hydrogen sensing (Tashie-Lewis and Nnabuife (2021); Buttner et al. (2017); El-Shafie et al. (2019)).

Targets have been set for many of the required technologies, including some of the key technologies listed below. Commercially available fuel cells currently have efficiencies of 35-40 % (Badwal et al. (2014)), short of the 60 % target proposed by the United States Department of Energy (DOE (2016)). Hydrogen storage for mobile applications can currently achieve 4.4 wt.% with compressed storage, with targets set at 7.5 wt.% (DOE (2016)). In the field of hydrogen purification, pressure swing adsorption is the dominant technology, accounting for 85 % of global supply (Schorer et al. (2019)). However, for high purity applications, such as in fuel cells, its efficiency is poor, recovering only 65-90% of the input hydrogen (Peramanu et al. (1999)). In hydrogen production, electrolyser efficiencies need to be improved from 67 % to 75 % (DOE (2016)). Finally, the field of hydrogen sensing requires improvement in response times and hydrogen specific sensitivity (Buttner et al. (2017)).

Just as hydrogen-based technologies seek to supplant mature technologies due to their incompatibility with the goal of global emissions reduction, a similar trend is occurring in the semiconductor industry. Mature silicon-based technology is approaching its physical limit and new semiconducting materials must be sought (Hassan et al. (2010)). One family of materials that has come to offer great promise in addressing this challenge are the van der Waals (vdW) materials and their corresponding quantum confined two-dimensional (2D) counterparts. The first exfoliation of graphene in 2004 demonstrated a simple method for the preparation of these materials and has spurred the experimental research in this field (Novoselov et al. (2004)). The quantum confinement resulting from the reduced dimensionality of 2D materials radically modifies their optical and electronic properties, giving access to a wide range of new quantum phenomena of both fundamental and applied interest, including low-power electronics, broad-band photo-detection and nanophotonics (Bernardi et al. (2017); Zhang et al. (2017); Hong et al. (2017); Kang et al. (2020)). These properties exist alongside the good flexibility and strength inherent to 2D materials (Gao (2017); Zou et al. (2018); Liu et al. (2017)), with tuneability possible through strain engineering, alloying, and surface modification (Kudrynskyi et al. (2020); Weng et al. (2018); Deng et al. (2018); Guo et al. (2015)). Given these properties, it is unsurprising that researchers are investigating 2D and 3D vdW materials for a wide range of applications.

Even before its first experimental exfoliation in 2004, theoretical papers emerged predicting the hydrogen adsorption capability of graphene (Arellano et al. (2000)). This was followed by experimental results quantifying its hydrogen adsorption capacity (Srinivas et al. (2010)). The short delay between the first exfoliation of graphene and papers describing its suitability for hydrogen storage is hardly surprising; carbon nano-tubes had previously been investigated for their hydrogen storage potential and the properties of vdW materials lend themselves to this application (Cheng et al. (2001)). vdW materials don't only have advantageous properties in hydrogen storage applications. Their large surface areas, electronic properties tuneable through alloying and exfoliation, excellent opto-electronic properties and functionalisation ability through surface modification make the vdW materials excellent candidates when considering improvements to the applications of purification, sensing and hydrogen production (Alekseeva et al. (2020); Blackstone and Ignaszak (2021)).

There is a two-way advantage to studying the interaction between hydrogen and vdW materials as not only are they promising to hydrogen technologies, hydrogen also offers promising options for vdW material modification. It is desirable to use hydrogen in this application due to its ubiquity in the semiconductor industry and environmentally minimal impacts. Additionally, the small size of the hydrogen molecule opens up the prospect of modifying vdW materials in ways not attainable by other means.

For either the hydrogen technology or semiconductor processing applications of vdW materials to be evaluated and realised, their fundamental interactions with hydrogen must first be understood. This work has been undertaken for many of the most popular vdW materials (graphene, MoS_2, hBN and MXenes), but the family of vdW materials is incredibly diverse and an understanding of this interaction for more of them would be greatly beneficial. It is for this reason that the interaction between hydrogen and the vdW materials InSe, GaSe and SnS_2 was explored.

1.2 Literature Review

Scientific knowledge of both vdW materials and hydrogen stretches back centuries with the first isolation of hydrogen made in 1766 and the first demonstration of the planar structure of graphite taking place in 1859 (Cavendish (1766); Brodie (1859)). Investigations of interactions between the two are also not new, with the reaction between graphite and hydrogen reported in 1965 (Gulbransen et al. (1965)). It might therefore seem strange that these two areas are currently seeing a renewed interest both individually and in conjunction. This renewed interest has been driven by independent developments in both fields. Enthusiasm has grown for hydrogen research as technological solutions are sought to reduce greenhouse gas emissions, and vdW materials have gained new attention since the first experimental demonstration of the mechanical exfoliation of graphene (Novoselov et al. (2004)). This second achievement opened up investigation into a class of materials with unique properties and has motivated researchers in a variety of fields, including those interested in their interactions with hydrogen.

This section covers the literature of investigations into the interactions between vdW materials and hydrogen and is divided into the following sections: physisorption, chemisorption and intercalation of hydrogen, the diffusion and permeability of hydrogen in vdW materials, the chemical conversion and etching of vdW materials by hydrogen, vdW materials for photocatalysis, and hydrogen as a dopant. It then goes on to discuss the specific vdW materials of GaSe, InSe and SnS_2, and previous studies of their interaction with hydrogen.

1.2.1 Modes of interaction: Physisorption, Chemisorption and Intercalation

Physisorption is the adsorption of molecules or atoms on a surface due to non-bonding dispersive forces. Chemisorption is the adsorption of molecules or atoms on a surface due to bond formation. These processes have relevance to the field of hydrogen storage. Hydrogen storage in mobile applications requires a high hydrogen wt.% for the entire storage system. In mobile applications, pressurised storage alone utilises high pressures of 700 bar to reach the volumetric densities required. This necessitates the use of heavy pressure vessels and safety equipment and results in up to 4.4 wt.% hydrogen storage (DOE (2016)). By placing an adsorbate material into a pressure vessel, the volumetric density is increased without requiring a corresponding increase in the pressure, as would be the case for compressed storage. For activated carbon materials, the volumetric density is increased by 23 % over compressed storage at the same pressure and achieves a material gravimetric density of 5.8 wt.% (Ramirez-Vidal et al. (2021)). By finding materials with sufficient volumetric and gravimetric hydrogen adsorption densities, the performance of the hydrogen storage system can be further improved to meet targets.

Carbon-based structures have long been considered as potential materials for hydrogen storage (Cheng et al. (2001)). As such, it was natural for researchers to begin with graphene when investigating the properties of hydrogen adsorption on bulk and 2D vdW materials. In fact, before even the first exfoliation of graphite to form graphene in 2004, theoretical predictions of the hydrogen adsorption abilities of graphene were made (Arellano et al. (2000)). In this prediction, hydrogen was found to preferentially locate above the centre of the hexagon in the graphene lattice with the hydrogen molecule lying parallel to the basal plane of the material. When considered experimentally, graphene is found to achieve a 1.2 wt.% hydrogen adsorption at 77 K and 10 bar (Srinivas et al. (2010)). This value is below the value obtained by pressured storage but can be improved further via the functionalisation of graphene, either to increase the number of available adsorption sites or their occupation. For example, mesoporous graphene oxide has achieved a 4.65 wt.% hydrogen adsorption at 40 bar at room temperature (Kim et al. (2016)).

The nature of the investigations into graphene offers a template by which the hydrogen adsorption properties of other materials can be explored. Theoretical studies have indicated hydrogen storage capabilities in other 2D materials greater than that of graphene. For example, reversible storage of 7.2 wt.% in Sc_2C (Le et al. (2020)). However, the literature on the wider range of vdW materials is far more limited than with graphene and is typically restricted to well known materials families like MXenes (Kumar et al. (2021)).

Chemisorption studies present a more complicated picture. It is not immediately obvious whether a material can successfully chemisorb hydrogen as chemisorption is often achieved only with hydrogen exposure under more reactive conditions (higher temperature or with atomic hydrogen). Under more reactive conditions, other alternative methods for interaction such as etching also become more favourable. In some materials, both chemisoprtion and etching are possible under different conditions. For example, graphene will be etched in the presence of H_2 gas at 1000 °C and undergo chemisorption at 27 °C in the presence of H-atoms dissociated from hydrogen silsesquioxane by an e-beam (Papon et al. (2015); Ryu et al. (2008)).

One unique mode of interaction between vdW materials and hydrogen is intercalation, the process by which chemical species are introduced to the vdW interlayer space. This was first demonstrated for graphite in 1840 when it was successfully intercalated electrochemically from a solution of sulphuric acid (Schafhaeutl (1840)). Intercalation of graphene has also been demonstrated under hydrogen gas exposure at <140 K (Grånäs et al. (2016)). Hydrogen intercalation has been demonstrated in other vdW materials including GaSe, In_2Se_3 and InSe, typically via electrochemical means (Kaminskii et al. (2005); Boledzyuk et al. (2011); Zhirko et al. (2007)).

More complicated behaviour can also be observed. For example, when exposed to H-ions it might be expected that a 2D material can interact via chemisorption, physisorption, intercalation or perhaps exhibit no interaction altogether. However, for the material MoS_2, it was shown that hydrogen ions can penetrate into the inter-layer vdW gap and form molecular hydrogen. This hydrogen then diffuses through the inter-layer space to form hydrogen filled bubbles under the surface of the material (Tedeschi et al. (2019)). This phenomenology demonstrates the complexity of interactions possible between hydrogen and vdW materials.

1.2.2 Diffusion and Permeability

The roles played by diffusion and permeability must be considered when investigating the interaction phenomenologies of hydrogen with vdW materials. In this instance, diffusion refers to the ability for species to move within the layer planes of a material, whilst permeability refers to the ability for the species to move between them.

The permeability of hydrogen across atomic membranes is assessed via the sealing of a small volume of gas by the membrane. The gas outside the volume is then evacuated and the deflection in the membrane is probed via atomic force microscopy. This process has been used to demonstrate that graphene is impermeable to the majority of gases, including helium but is slightly permeable to hydrogen (Bunch et al. (2008); Sun et al. (2020)). However, hBN and MoS_2 are not permeable to hydrogen (Sun et al. (2020)). The picture is different for protons and atomic hydrogen to which graphene and hBN are both permeable (Hu et al. (2014); Lozada-Hidalgo et al. (2016)). This is not true for all vdW materials. Notably, MoS_2 is impermeable to thermal protons (Hu et al. (2014)). When sufficient kinetic energy is imparted to the protons, it is possible for them to cross the vdW layers, as in the case for MoS_2, where bubble formation after proton beam exposure is only possible due to protons penetrating the uppermost MoS_2 layer (Tedeschi et al. (2019)).

Diffusion within the vdW gap is far more favourable than the permeation of hydrogen across vdW layers. In this instance, the diffusion of atomic hydrogen within the layers has been demonstrated for graphite, hBN and MoS_2 (Hu et al. (2018); An et al. (2019)), where atomic hydrogen is introduced into the material from palladium and exhibits differential diffusion rates for hydrogen and deuterium species.

1.2.3 Chemical Conversion and Etching

The chemical reactivity of hydrogen must be considered as part of any interaction. In addition to the chemisorpton of hydrogen, more transformative interactions are possible whereby the oxidation state, structure or composition of the vdW material are modified. Graphite can react with hydrogen to form methane when held at elevated temperatures (>1200 °C) and when the products are continually removed (Gulbransen et al. (1965)).

When properly utilised, this reaction can be used to anisotropically etch graphene (Yang et al. (2010)).

Reactions with vdW materials that produce stable hydrogen compounds can be particularly pronounced. This is most notable with selenide and sulphide compounds with which hydrogen can react to form the relatively stable molecules H_2S and H_2Se. For these materials the presence of hydrogen has proved particularly useful in controlling material growth. Hydrogen assisted chemical vapour deposition processes for MoS_2, WS_2, WSe_2 and In_2Se_3 exhibit strong morphological and stoichiometric hydrogen dependencies (Li et al. (2015); Sheng et al. (2017); DeGregorio et al. (2020); Chang et al. (2006)).

1.2.4 Photocatalysis

Photocatalysis describes a process of using the energy of an incoming photon to overcome a kinetic barrier to a reaction and thus catalysing it. In the instance of solar water splitting, the energy carried by the photon also provides some or all of the thermodynamic impetus for the reaction. The first demonstration of solar water splitting was made in 1972 utilising TiO_2 connected to a platinum electrode and illuminated by ultraviolet light (Fujishima and Honda (1972)). Whilst successfully generating hydrogen, this process produces a low solar to hydrogen efficiency owing to the wide band-gap of TiO_2 at 3.2 eV, meaning that 97 % of solar radiation energy is unused (Eidsvåg et al. (2021)). Recent motivation to increase the efficiency of green hydrogen production has seen renewed interest in this field with the primary interest in finding materials capable of greater solar to hydrogen efficiencies. Currently, the highest efficiencies have been achieved for Rubidium decorated TiO_2 in a tandem architecture with an efficiency of 19 % (Cheng et al. (2018)).

In this application, vdW materials show promise. This is due to their high surface areas, good opto-electronic properties and tuneable band edges. As such, research on vdW materials for solar water splitting has seen considerable interest. Currently, $MoSe_2$ holds the record for hydrogen production at 62,000 μmol h^{-1} g^{-1} (Li et al. (2017b)). Additionally, theory predicts potential efficiencies of 15 % in a single junction MoS_2/WSe_2 heterostructure (Dalla Valle and Cavassilas (2022)).

1.2.5 Hydrogen Doping

Atomic hydrogen has long been used as a dopant in semiconducting materials for the modification of optoelectronic properties. Typically introduced via implantation from a beam of hydrogen ions or from a hydrogen plasma. The incorporation of hydrogen can introduce hydrogen associated sates into the material or passivate already existing states. In the case of the traditional semiconductor Si, the introduction of hydrogen has been shown to suppress the contribution of existing impurities due to its ability to act as either a donor or acceptor (Van de Walle and Neugebauer (2006)).

In vdW materials the effect of hydrogen on the doping of a semiconductor has also been investigated. In MoS_2, the exposure to hydrogen has been demonstrated to reduce the n-type doping due to sulphur vacancies becoming occupied by hydrogen (Pierucci et al. (2017)). Unlike in traditional semiconductors, for 2D vdW materials the substrate response to hydrogen treatment must also be considered. For example, the passivisation of Si dangling bonds by hydrogen greatly improves the carrier mobility of graphene (Pallecchi et al. (2014)).

1.2.6 Material Selection

The vdW materials γ-InSe, ϵ-GaSe and SnS_2 were selected for investigation. They were chosen for a number of factors, some of which were common to all three, such as ready availability, and others specific to each material, as detailed in the review of the literature for each material below.

γ-InSe

γ-InSe is a layered group III-VI semiconductor, which crystallises in the R3m space-group with lattice constants $a = b = 4.002$ Å and $c = 24.946$ Å (Rushchanskii (2004)). The structure of γ-InSe is shown in Figure (1.1). A number of attributes make γ-InSe an interesting material for hydrogen interactions. The first is the nature of the vdW gap, which is large (3.6 Å) and comprises approximately 40 % of the internal crystal volume between the centre of neighbouring Se planes (Zhirko et al. (2007)). This large internal volume has previously been exploited in electrochemical intercalation studies, which introduced hydrogen into the vdW gap up to $x = 5$, where x is the number of hydrogen atoms per stoichiometric formula unit (Zhirko et al. (2007)). It was suggested that this hydrogen is incorporated as a monolayer of molecular hydrogen within the vdW gap. There is also significant scope for the modification of the optoelectronic properties of γ-InSe via hydrogen incorporation due to the high interlayer electron density in γ-InSe owing to the projection of P_z orbitals from the Se atoms into the vdW gap (Li et al. (2019); Sun et al. (2018)). Experiments on hydrogen intercalated γ-InSe demonstrate this with an intercalation induced modification to the exciton absorption spectra (Zhirko et al. (2007)).

The demonstration of successful electrochemical hydrogen intercalation of

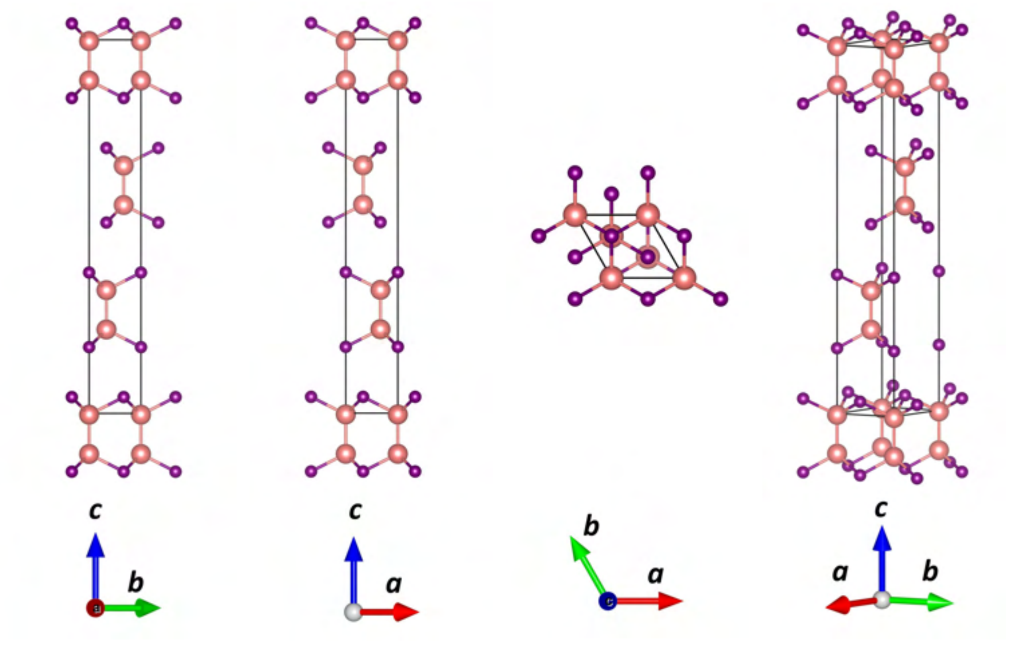

(a) (b) (c) (d)

Figure 1.1: Unit cell of γ-InSe along the (a) a-axis, (b) b-axis, (c) c-axis and (d) at a slight angle. The pink and purple atoms are indium and selenium, respectively. The structure was generated using literature results (Rushchanskii (2004)).

γ-InSe raises the possibility of the stability of intercalated hydrogen from the gas phase and from accelerated hydrogen ions. This, coupled with the low Young's modulus and interlayer adhesion energy of γ-InSe (Zhao et al. (2019)), points to γ-InSe as being relatively stable to molecular hydrogen incorporation within the vdW gap. The presence of Se in γ-InSe is important here and the ability for hydrogen to bond to Se must also be considered.

ϵ-GaSe

Much like γ-InSe, ϵ-GaSe is a layered group III-VI semiconductor. ϵ-GaSe crystallises in a P$\bar{6}$m2 space-group with unit cell parameters of $a = b =$ 3.749 Å and $c = 15.907$ Å (Wang et al. (2018)). The structure of ϵ-GaSe is shown in Figure (1.2). Much like γ-InSe, successful electrochemical intercalation of hydrogen into ϵ-GaSe has been demonstrated previously (Kaminskii et al. (2005)). This intercalation modifies the adsorption spectra and dielectric properties of the material (Kaminskii et al. (2005, 2007)). As with γ-InSe, the successful intercalation of ϵ-GaSe raises the possibility of stable intercalation via molecular and atomic hydrogen.

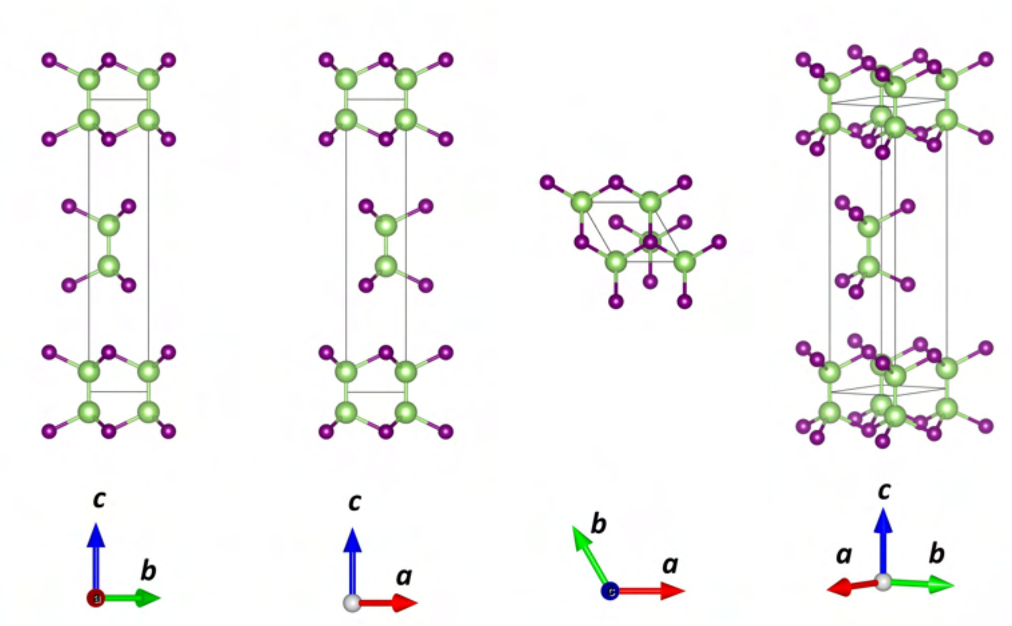

(a) (b) (c) (d)

Figure 1.2: Unit cell of ϵ-GaSe along the (a) a-axis, (b) b-axis, (c) c-axis and (d) at a slight angle. The green and purple atoms are gallium and selenium, respectively. The structure was generated using literature results (Wang et al. (2018)).

The primary interest in ϵ-GaSe in this PhD arises from its photocatalytic properties. Namely, the size of its band gap at 2.02 eV and the optimal position of its band edges for hydrogen and oxygen evolution (Ferrer-Roca et al. (1999)). These properties of ϵ-GaSe have led to multiple demonstrations of GaSe as a phtotocatalytic material (Zappia et al. (2020); Meng et al. (2022)). The improvement in phtotocatalytic performance of ϵ-GaSe has also been demonstrated via modification by oxidation and the creation of local catalytic centres (D'Olimpio et al. (2020)).

The band structure of ϵ-GaSe grown by molecular beam epitaxy has been reported previously via angle resolved photoemision electron spectroscopy (Eremeev et al. (2020)). These measurements demonstrate the Mexican hat like valence band in single tetralayer GaSe (Chen et al. (2018b)). This is of interest as ring shaped valence band maxima are expected to produce a singularity in the electronic density of states. These singularities have the potential to for wide application such as in thermoelectrics (Wickramaratne et al. (2014)). The measurements also indicate the valence band structure of bulk GaSe with a hole effective mass of 0.9 m_e (Eremeev et al. (2020)).

SnS_2

SnS_2 is a IV-VI semiconductor with a structure notably different to that of InSe and GaSe. SnS_2 has a structure resembling MoS_2 and crystallises in a P-3m1 space-group with lattice constants $a = b = 3.64$ Å and $c = 5.92$ Å (Yang et al. (2002)). The structure of SnS_2 is shown in Figure (1.3). Unlike InSe and GaSe, the unit cell of SnS_2 only extends over one vdW layer and within each layer all of the Sn atoms lie in the same plane.

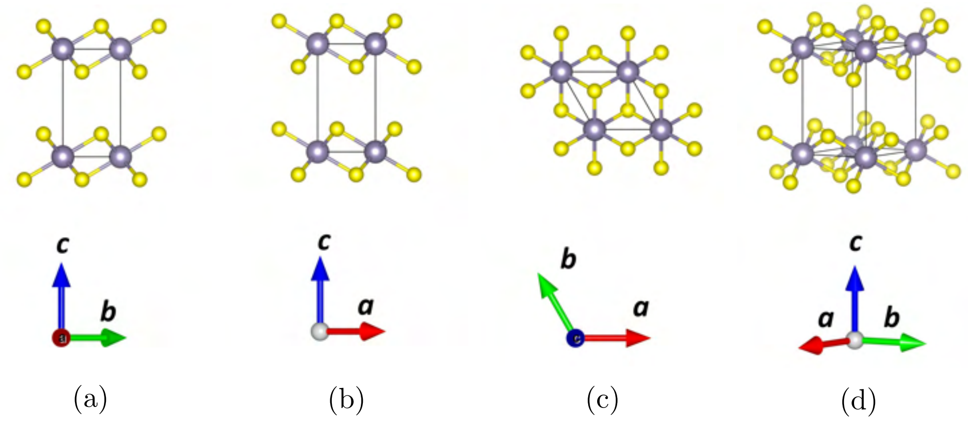

(a) (b) (c) (d)

Figure 1.3: Unit cell of SnS_2 along the (a) *a*-axis, (b) *b*-axis, (c) *c*-axis and (d) at a slight angle. The purple and yellow atoms are tin and sulphur, respectively. The structure was generated using literature results (Yang et al. (2002)).

The chemical reactivity of hydrogen with sulphur is important in the case of

SnS_2. The ability for Sn to exist in multiple different stable oxidation states means that multiple vdW systems are present in the tin-sulphur system. This includes SnS, a vdW material which forms in the Pnma space-group. This quality of the tin-sulphur system has been used to produce SnS/SnS_2 heterosructures via a variety of different methods. One method involves sulphurisation whereby sulphur is introduced to SnS to convert it into SnS_2 (Li et al. (2021)). Alternatively, the reverse is also possible, whereby sulphur is removed from SnS_2 to convert it into SnS (Kim et al. (2018)). The SnS/SnS_2 heterostructures resulting from these conversions have seen successful application as heterojunction diodes (Kim et al. (2018)), NO_2 detectors (Sun et al. (2019)), and as other opto-electronic devices (Li et al. (2018)).

Hydrogen has been shown to modify the electronic properties of SnS. When treated with H-plasma, there is a marked reduction in the hole carrier density of SnS and an increase in hole mobility (Xiao et al. (2018)). This change is a result of H atoms compensating for Sn vacancies.

1.3 Scope

The Motivation and Literature Review sections discuss the context of hydrogen vdW materials interactions both in fundamental and applied contexts. The scope section covers the new results gained over the course of this PhD and describes the thesis structure as follows. Chapters 2 and 3 describe the relevant theoretical concepts and experimental methods, respectively. The results of the conducted research are then described in Chapters 4, 5 and 6, and briefly summarised in sections 1.3.1 (Chapter 4), 1.3.2 (Chapter 5) and 1.3.3 (Chapter 6). A summary of the results and future prospects are then provided in Chapter 7.

1.3.1 Hydrogen - Tin Sulphides Interaction

It is known that hydrogen has the ability to reduce the vdW material SnS to Sn, altering the oxidation state of Sn and decreasing the S content (Sneed and Brasted (1958)). This raises the prospect of utilising hydrogen to modify the stoichiometry of other Sn-S materials. Notably, the vdW semiconductors SnS_2 and SnS.

To assess whether hydrogen can modify the properties of SnS_2 and SnS, samples of SnS_2 were exposed to both H_2 and H-ions. The resulting interactions were found to modify the crystal stoichiometry and the oxidation state of Sn. In the instance of H-ion exposure, SnS_2 was reduced to both SnS and Sn. With H_2 exposure, only SnS was produced.

Remarkably, the conversion of SnS_2 to SnS by H_2 resulted in the formation of a well ordered SnS/SnS_2 heterostructure. The SnS and SnS_2 layers are well aligned, continuous, and have a uniformity stretching across ~ 10 μm, whilst retaining a strong optical response. This presents a new and highly scalable approach to producing SnS/SnS_2 heterostructures and was reported in Felton et al. (2022).

1.3.2 Hydrogen - Indium Selenide Interaction

The high flexibility, low interlayer adhesion energy, and high electron density in the vdW gap of γ-InSe suggests it should be notably modified by hydrogen intercalation. To investigate this and overcome barriers to hydrogen entering the vdW gap, InSe was exposed to hydrogen from a Kaufman ion source. The resulting samples were found to contain atomic hydrogen bonded to the Se in InSe, which induced a corresponding change in its phonon modes. Molecular hydrogen exposure of InSe was also conducted to test for hydrogen intercalation from the gas phase. In bulk InSe samples, no hydrogen uptake was observed. However, in powdered InSe samples hydrogen uptake of up to 0.2 wt% was measured.

Theoretical investigations describe the extent to which the InSe inter-layer space would have to expand in the case of hydrogen incorporation and the resulting phonon modifications. In the case of molecular hydrogen incorporation, the vdW gap would need to expand by 2.5 Å. The increased interlayer separation reduces the strength of the interlayer coupling and as such the phonon modes take on a more monolayer like character, suggesting an exciting means to modify the properties of γ-InSe. The work regarding the H-ion exposure and theoretical results is reported in Felton et al. (2020).

1.3.3 Gallium Selenide for Photocatalysis

Preliminary experiments of the interaction between GaSe and both atomic and molecular hydrogen yielded no pronounced changes. Instead, given the favourable band gap and band edge positions of GaSe for photocatalysis, investigations into its photocatalytic ability for solar water splitting were conducted. Namely, water exposure of GaSe induces its oxidation. This has been shown to improve its photocatalytic performance but without consideration on how the electronic band structure of GaSe is modified by the oxidation.

The oxidation of GaSe was observed by near ambient pressure X-ray photoelectron spectroscopy and atomic force microscopy. The valence band structure of oxidised GaSe was then observed in both thick and thin flakes using angle resolved photoemission spectroscopy. Experiments to-date have established the carrier effective masses in both bulk and 6-layer thick GaSe. Additionally, 3 relatively flat bands were observed near the valence band maximum in 6-layer thick GaSe, an observation relevant to the application of photocatalysis.

Chapter 2

Theoretical Concepts

This chapter covers the theoretical concepts relevant to the phenomena investigated in the course of this PhD. These concepts include: The origin of the electronic and phonon dispersions in semiconducting materials, the rules governing the electronic band alignment in heterostructures and photocatalytic systems, and key thermodynamic and kinetic theories.

Contents

2.1 Electronic and Phonon Dispersions of vdW Materials

The opto-electronic properties of a semiconductor are governed by its electronic band structure and phonon dispersion. The first of these describes the electronic energy-momentum relation for a material and is relevant when considering its effective carrier masses, the size of its band gap and its electronic density of states. The phonon dispersion of a material instead describes its structural vibrational modes, as determined by the crystal lattice and its symmetries. This section describes the origin of both of these dispersions and describes their behaviour in vdW materials.

2.1.1 Electronic Band Structure

A neutral atom held in isolation contains an equal number of protons and electrons. The protons are concentrated in the atom's nucleus and the electrons are distributed in concentric shells around it. As fermions, the electrons cannot all occupy the same lowest energy state and instead they fill up, in sequence, the concentric shells, following the Aufbau principle (Atkins et al. (2014)). The electronic orbitals are spherical harmonic solutions of the Schrödinger equation, modified by the interaction with the other atomic orbitals (Elliott (1998)).

The atomic picture of electrons doesn't hold for solid materials as it confines the electrons to an individual atom and as such fails to account for macroscopic properties, such as the electrical conductivity. One approximation to the behaviour of electrons in bulk material is the free electron model. This model considers the electrons as existing in a uniform potential with a parabolic electronic energy dispersion given by

$$E(\mathbf{k}) = \frac{\hbar^2\mathbf{k}^2}{2m^*}, \tag{2.1}$$

where $E(\mathbf{k})$ is the energy of an electron with wavevector $\mathbf{k}$, $\hbar$ is the reduced Planck's constant and m^* is the electron effective mass (Klingshirn (2012)). This model is successful in describing some of the behaviours of electrons within a material, especially for metals. However, it fails to explain the conductivity behaviour of non-metallic materials such a silicon, or to take into account the influence of the crystallographic lattice on electronic properties.

A more accurate description of semiconductors is given by the Bloch approach. In this model, the electrons experience a periodic spatially-varying potential due to the presence of a crystallographic lattice. The electronic wavefunction is then given by the product of a plane wave and a function with the same periodicity as the lattice (Elliott (1998)). The Bloch approach considers a periodic lattice with atoms positioned at $\mathbf{R} = u\mathbf{a}$, where u is an integer. A translation from point $\mathbf{r}$ to $\mathbf{r} + \mathbf{a}$ is then given by

$$\psi_k(\mathbf{r} + \mathbf{a}) = e^{i\mathbf{k}\cdot\mathbf{a}}\psi_k(\mathbf{r}), \tag{2.2}$$

where $\psi(\mathbf{r})$ is the wavefunction and $\mathbf{k}$ describes the reciprocal space vector. For this translational relation to hold, the wavefuntion must share a periodicity with the underlying lattice. The wavefunction at point $\mathbf{r}$ is then given by

$$\psi_k(\mathbf{r}) = e^{i\mathbf{k}\cdot\mathbf{r}}u_k(\mathbf{r}), \tag{2.3}$$

where $u_k(\mathbf{r})$ is a function with the same periodicity as the underlying lattice (Elliott (1998)).

In the nearly free electron model, the interaction between the electrons and atoms is assumed very weak. In this instance, the free electron model is modified so that the solutions are consistent with the Bloch description. At the edge of the Brillouin zone, solving for the electron wavefunction at position x gives two solutions,

$$\psi^{+} \propto (e^{iGx/2} + e^{-Gx/2}) \propto \cos(Gx/2), \tag{2.4}$$

$$\psi^{-} \propto (e^{iGx/2} - e^{-Gx/2}) \propto \sin(Gx/2), \tag{2.5}$$

where G is the reciprocal lattice vector. In a periodic potential, which shares periodicity with the wavefunction, these two solutions are separated in energy. Physically this is due to one having a greater electron density positioned on the atoms, whilst the other has a greater electron density between them. The separation in energy of the two wavefunctions corresponds to a band gap within the material. The size of the band gap is composition and temperature dependent. The temperature dependence arises due to the changing atomic separations with temperature. At lower temperatures the material contracts, the inter-atomic space reduces and the band gap increases. Additionally, the reduced thermal fluctuations of the lattice at lower temperatures modifies the band gap.

Generally, in bulk vdW materials there is a significant structural anisotropy with covalent bonds directed along the a and b axes whilst vdW interactions dominate along the c-axis. Correspondingly, the unit cell along the c-axis is typically larger than along either the *a* or *b* axes. This is reflected in both an anisotropy in the electrical conductivity and in the Brillouin zone. Upon exfoliation to produce 2D vdW materials, the lattice periodicity is broken once the dimensions of the crystal are of a comparable scale to the coherent electron wavefunction. By analogy to an infinite quantum well, the energy gaps between allowed standing waves of the electron increases as the well thickness decreases. In a real vdW system, the reduction in electronic screening also plays a role in the band gap energy and the stability of phenomena such as excitons. These effects combine to increase the band gap energy with reducing thickness.

The real-space symmetry of a crystal lattice determines the properties of its electronic band structure. The reciprocal image of the primitive unit cell is termed the 1^{st} Brillouin zone. The edges of the 1^{st} Brillouin zone are then high symmetry directions, i.e. lie at points at which the electron wavevector is commensurate with the real-space lattice. As the wavevector of an electron relates to its momentum via $\mathbf{p} = \hbar\mathbf{k}$, and all wavevectors outside the 1^{st} Brillouin zone are degenerate with states inside it, the electron momentum-energy dispersion of a material can be defined fully inside the 1^{st} Brillouin zone.

The presence of bands in solid materials can be understood as a consequence of orbital hybridisation. When two atoms, each with one electron, are brought together their electronic energy levels will be modified. The original electron orbital is split into two levels associated with the bonding and antibonding configurations. When a third atom is introduced a third level will appear. In fact, with N atoms in the system, N levels will be produced from the single initial energy level (Atkins et al. (2014)). These energy levels are distributed over a finite energy window and in the case of a typical solid material where N is very large (1 mole $= 6 \times 10^{23}$), the separation between the energy levels becomes sufficiently small to be described as a continuous function. This function, the density of states ($D(E)$), then gives the number of states $N(E)$ between E and $E + \delta E$ as $N(E) = D(E)\delta E$.

Density Functional Theory

In real materials, the calculations based on the nearly free electron model or by the linear combination of atomic orbitals fall short of providing an accurate quantitative description of the electronic band structure. Instead, what is required are highly accurate computational models which consider the electronic behaviour in the real crystal structure. However, the computational cost of performing the full quantum mechanical calculation is prohibitively expensive, with the coupled cluster single double (triple) (CCSD(T)) method, being one of the most accurate, scaling as N^7 (Harrison (2003)). This limits its use to small systems of extremely high scientific interest. To overcome this issue, a way to approximate the full quantum mechanical solution is utilised. The most common approach to this is density functional theory (DFT), which reduces the problem to 6 dimensions (Harrison (2003)).

DFT is based on a result proved by Hohenburg and Kohn that instead of solving for the wavefunctions of all the individual electrons, a generalised electronic density is used which then provides the correct solution to the Hamiltonian with an additive constant (Hohenberg and Kohn (1964)). This results in the expression

$$\delta \left[E\left[\rho\right] - \mu \left(\int \rho(\mathbf{r} d\mathbf{r} - N \right) \right] = 0, \tag{2.6}$$

where $E[\rho]$ is the energy functional of the trial electron density (ρ), μ is the chemical potential, $\mathbf{r}$ is the position and N is the number of electrons in the considered volume. The energy functional is then given by

$$E[\rho] = T[\rho] + V_{ext}[\rho] + V_{ee}[\rho], \tag{2.7}$$

where $T[\rho]$ is the kinetic energy functional, $V_{ext}[\rho]$ is the external potential functional, and $V_{ee}[\rho]$ is the electron-electron interaction functional (Harrison (2003)). The exact forms of these functionals are unknown, but several approximate solutions are commonly used allowing for the application of DFT to real systems (LDA, GGA, Meta-GGA, Hybrid functionals...). The different functionals vary in their ability to successfully predict ρ and lend themselves to different systems. The selection of the correct functionals is then determined by the agreement with experimental results from the same or similar systems.

Shown in Figure (2.1a) is the DFT generated electronic band structure of ϵ-GaSe. The changes in band structure due to the reducing of dimensionality are apparent upon comparison to the monolayer band structure shown in Figure (2.1b). Evident is the increased size of the band gap and the emergence of an inverted Mexican hat-like valence band maximum. The size of the band gap is underestimated at 1.21 eV compared to experimentally measured 2.02 eV (Ferrer-Roca et al. (1999)).

As ARPES does not conserve the k_z momentum component, but instead produces a sum over that vector, the experimental data displayed in Figure (2.1) shows the dispersion's along the $\bar{\Gamma}\bar{\text{K}}$ and $\bar{\Gamma}\bar{\text{M}}$ directions. The bar notation denotes that this data is a projection over the Brillouin zone. In Figures (2.1e) and (2.1f) the Brillouin zone and projected Brillouin zone

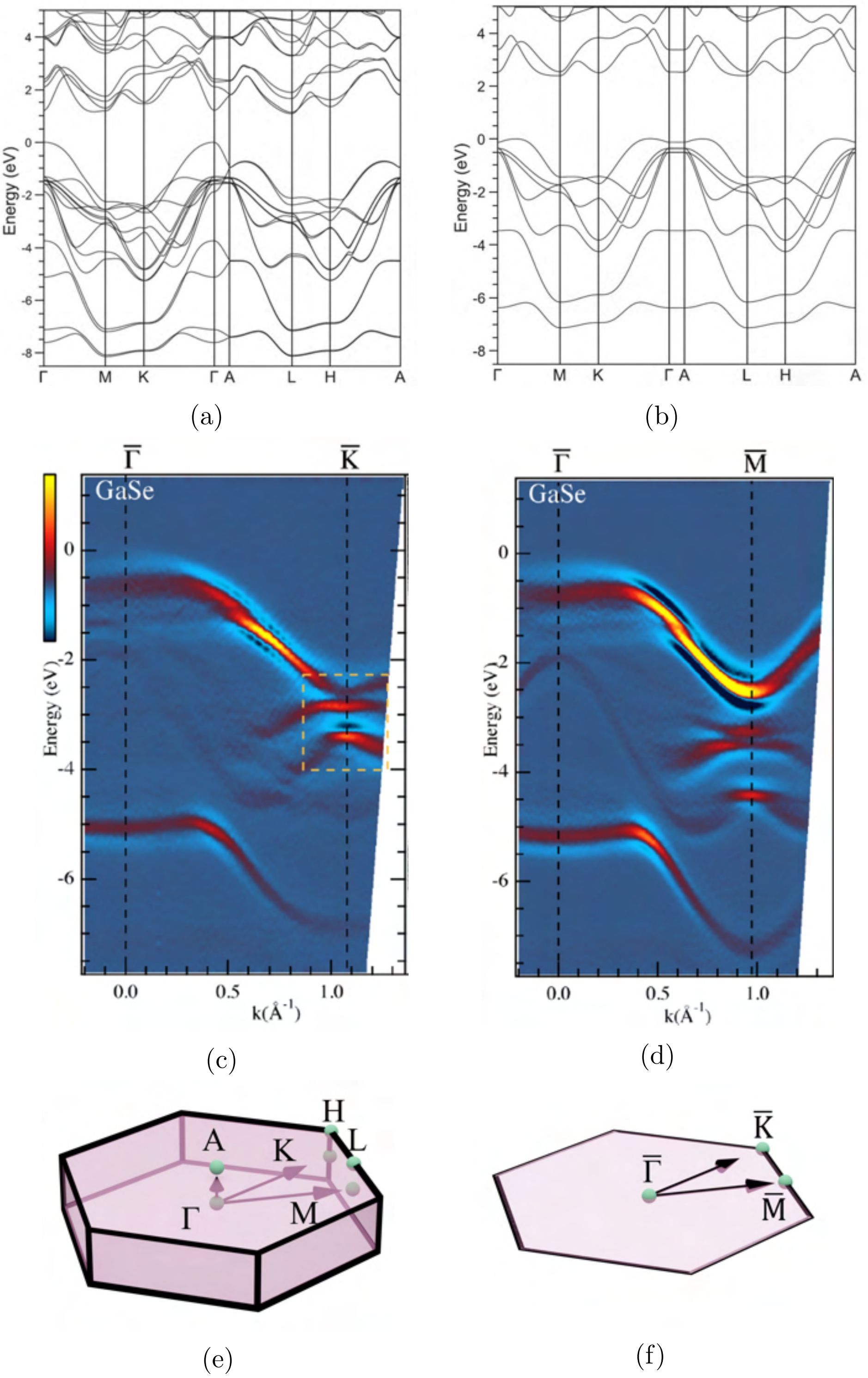

Figure 2.1: DFT generated electronic band dispersions of (a) bulk and (b) monolayer ϵ-GaSe, reproduced from Rybkovskiy et al. (2011). Valence band dispersions of bulk ϵ-GaSe determined via ARPES along the (c)$\bar{\Gamma}\bar{K}$ and (d) $\bar{\Gamma}\bar{M}$ directions, reproduced from Eremeev et al. (2020). The (e) full and (f) project Brillouin zone of ϵ-GaSe.

of ϵ-GaSe are shown, respectively. Demonstrated is the use of the bar notation when applied to ϵ-GaSe. As ARPES does not conserve the the k_z momentum component, the dispersion along k_z must be considered when making comparisons between an experimentally and theoretically determined dispersion.

2.1.2 Vibrational Structure

As is the case for electronic band structures, the symmetry of a crystal lattice has pronounced effects on the coherent vibrational modes of a material. The lattice restricts the allowed vibrational modes to specific frequencies for a given wavevector, described by the materials phonon dispersion. In the long wavelength limit, the dispersion relation for longitudinal acoustic modes on a 1D diatomic chain is given by

$$\omega_k^2 \simeq \frac{Ka^2k^2}{2(M+m)}, \tag{2.8}$$

where ω_k is the frequency, K is the interatomic spring constant, a is the lattice constant and M and m are the masses of the two atoms (Elliott (1998)). For optical longitudinal modes the dispersion relation in the long wavelength limit is given by

$$\omega_k^2 \simeq \frac{2K(M+m)}{Mm}. \tag{2.9}$$

These modes have a non-zero frequency at a wavevector of zero. By contrast, for the acoustic modes, the frequency tends to zero with the wavevector. By comparison with Equation (2.1) for the free electron dispersion relation, the vibrational modes have a lower energy for a given wavevector.

As such, generated phonons can transfer significant momentum for a small amount of energy.

The full quantum mechanical description of vibrations in a solid results in the quantisation of the vibrational modes. These quantised modes are known as phonons. When a crystal interacts with external fields, such as via photons, its vibrational properties (e.g. Raman Spectra) are modified/probed via an interaction with quantised phonons. As such, the energy difference in the incoming and outgoing energy of a photon during Raman spectroscopy is modified by a well defined energy, determined by the phonon. Photons can transfer only a little momentum to a crystal due to their dispersion relation, $E = pc$, where the momentum p of the photon is small due to the speed of light c being large. As phonons can transfer significant momentum and their energies are relatively small, the modification to the photon energy is small, even if the photon is scattered by 180°.

In vdW materials the interlayer vdW forces are much weaker than then intralayer covalent ones. As such, the spring constant, K, is lesser for the interlayer vibrations. Consequently, the interlayer phonon modes would be expected to have a flatter dispersion than their intralayer counterparts. The structure of vdW materials results in a high thermal anisotropy. For example, the thermal conductivity of graphite is 100× greater along the basal plane then normal to it (Balandin (2011)).

As with the determination of electronic band structure in real materials, the determination of the vibrational dispersion for a material requires computational methods. DFT is popular for this purpose (Mohr et al. (2007)).

2.2 Energy Band Alignment

When two semiconducting materials are placed into contact with one another, the electronic band structure of each is modified at the interface. The exact nature of this modification is dependent on the relative positions of the valence and conduction bands of the materials, the position of their Fermi levels, the dielectric permittivity in each of the materials and the charge carrier density.

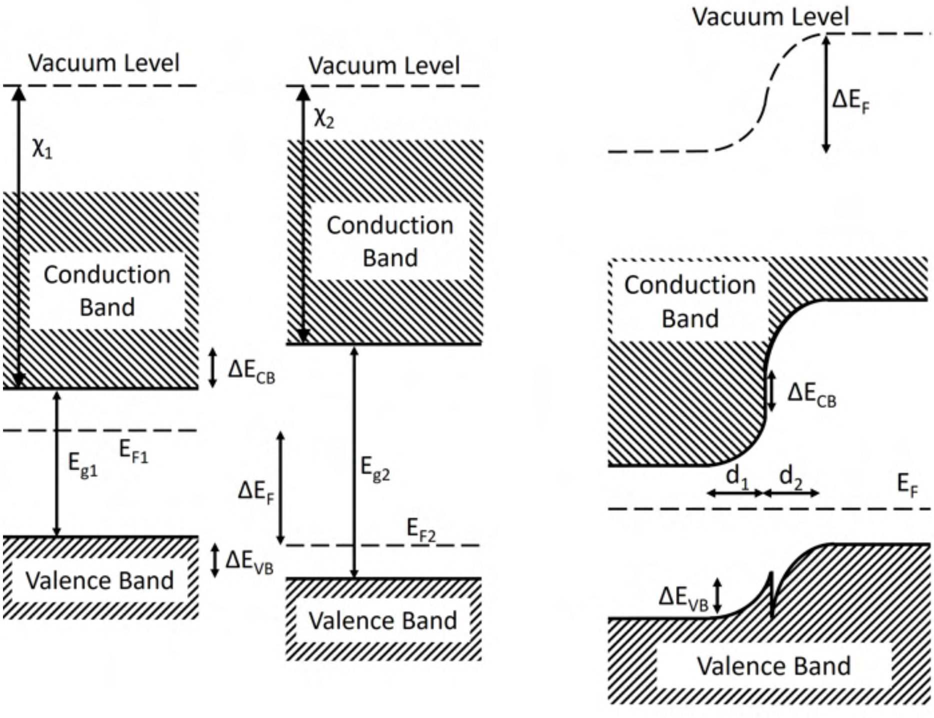

(a) (b)

Figure 2.2: Sketches of (a) the vacuum level aligned valence and conduction bands in two separate semiconducting materials and (b) the same materials brought into contact, illustrating the band bending at a heterostructure interface.

For two semiconducting materials with known band alignments, the Anderson rule can be used to determine their behaviour at the interface. The Anderson rule states that the vacuum level of the two materials must be aligned. The electron affinities and band gaps are then used to determine the band offsets at the interface. Figure (2.2a) shows the band edge positions of two materials aligned to the vacuum level. Utilising the electron affinities (χ_1,χ_2) and the band gap energies ($\mathrm{E_{g1}}$,$\mathrm{E_{g2}}$), the offsets in the conduction ($\Delta\mathrm{E_{CB}}$) and valence ($\Delta\mathrm{E_{VB}}$) bands can be determined. When the materials are brought together, a bending of the bands of both materials occurs. The difference in the Fermi levels of the two materials ($\Delta\mathrm{E_F}$) determines the extent of this bending and correspondingly the size of the built it potential of the heterostructure. The direction of the bending will act to align the Fermi levels of the two materials across the interface, with the spatial distribution of the bending determined by the charge carrier density in each material and their dielectric permittivities. This exact band distribution is determined via the Poisson equation

$$\bigtriangledown^2\phi = -\frac{\rho}{\epsilon}, \tag{2.10}$$

where ϕ is the electric potential, ρ is the charge density and ϵ is the permittivity of the material. The displacement of charge between the materials should be sufficient to produce a voltage, which aligns the two Fermi levels, whilst retaining overall charge neutrality. Far from the junction, the two materials should behave the same as before they were brought together. The conduction and valence band offsets present before bringing the materials together are present at the heterostructure interface as band discontinuities (Klingshirn (2012)).

A similar change can occur at the surface of a semiconductor when exposed to water. When held separately, the water species contain filled and unfilled electronic orbitals. The highest occupied molecular orbital (HOMO) and the lowest unoccupied molecular orbital (LUMO) have well defined energies relative to the vacuum level. The alignment of the vacuum level across

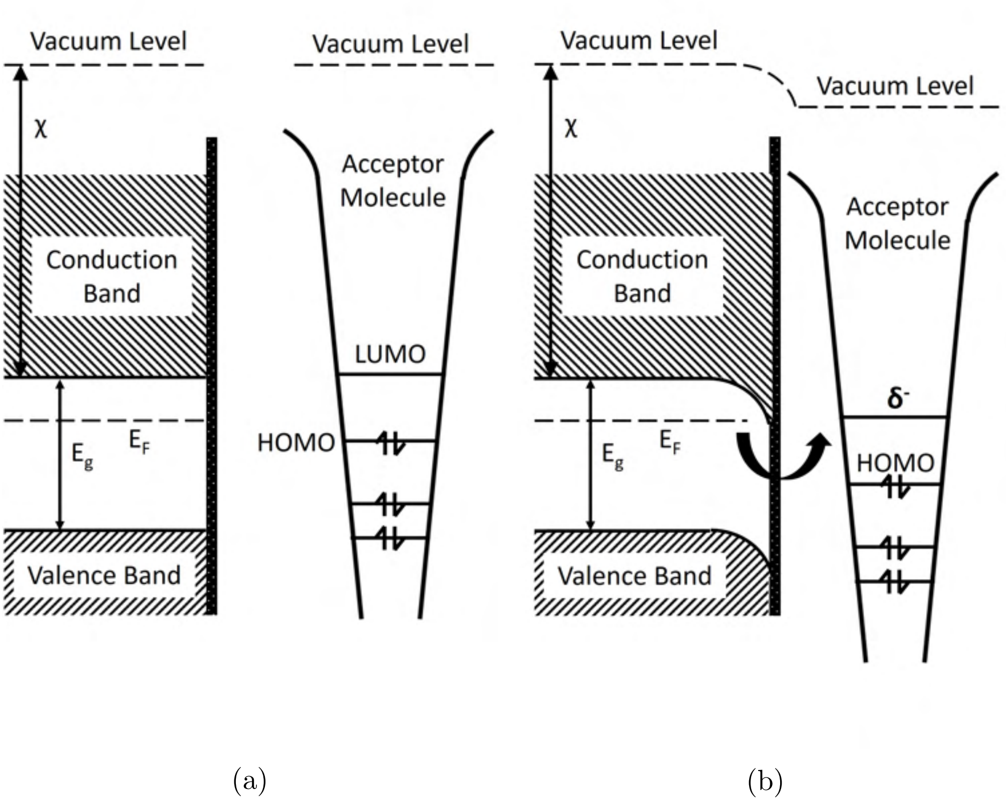

Figure 2.3: Sketches of the band alignment of an n-type semiconductor and a small acceptor molecule (a) when held apart and (b) when the acceptor molecule is adsorbed on the semiconductor.

the semiconductor and molecule then determines the offset between the semiconductor bands and the molecular orbitals (Figure (2.3a)). When a molecule of water is adsorbed onto the surface of a semiconductor, a small transfer of charge to or from the molecule can take place (Jiang et al. (2017)). The direction of this transfer is dependent on the conductivity type of the semiconductor and the position of its Fermi level relative to the either the H^+/H_2 or H_2O/O_2 redox potentials. In an n-type conductor, the Fermi level aligns to the LUMO of the slightly positive water species (Figure (2.3b)). The same occurs in p-type conductors, but with the Fermi level aligning to the HOMO of the negative species. The alignment induces a bending of the bands in the semiconductor and the establishment of a Helmholtz layer in the adsorbed water. The depletion layer established in the semiconductor is typically much larger than the thickness of the Helmholtz layer due to enhanced screening in the semiconductor (Jiang et al. (2017)).

2.3 Thermodynamics and Kinetics

The chemical changes in vdW materials induced by hydrogen or the photocatalytic splitting of water by a vdW material are dependant on both thermodynamic and kinetic factors. These factors are typically material specific but follow general laws, patterns and principles, as detailed below.

2.3.1 Thermodynamics

The chemical conversion or modification of a material by hydrogen can only proceed if thermodynamically favourable. Ascertaining whether a particular process meets this requirement can be accomplished via an understanding of thermodynamic laws and their application to a particular system. In particular, it is compatibility with the second law which details the requirement for the entropy of an isolated system to increase or remain constant. When a system is in contact with an environment at a constant temperature, this can be expressed mathematically as

$$0 \geq Q - \Delta S_s T = \Delta G, \tag{2.11}$$

where Q is the heat energy flowing from the environment to the system, ΔS_s is the entropy change of the system, T is the temperature and ΔG is the change in the Gibbs free energy. Based on the inequality statement of the Second Law, when ΔG is negative a process can proceed; when ΔG is equal to zero, the process is reversible; and when ΔG is positive the process cannot proceed spontaneously.

The size of ΔG determines the thermodynamic impetus of a process and its relation to Q, ΔS_s and T indicates the effect each of these variables have on its favourability. A negative value of Q, i.e. the process is exothermic and releases energy, increases the favourability. When T is equal to 0 K, only Q determines the favourability of the process and it is the same as ΔG. When the temperature is increased, the entropy of the process increases in importance relative to Q. As such, if ΔS_s is positive, then increasing the temperature will decrease ΔG and make the process more favourable. The reverse is true if ΔS_s is negative.

There are four possible combinations of ΔS_s and Q. In the first, ΔS_s is negative and Q is positive; in this instance the process is unfavourable at all temperatures. In the second, ΔS_s is positive and Q is negative and the process is favourable at all temperatures. In the third, ΔS_s and Q are positive. In this case, below a critical temperature the process is unfavourable and above the critical temperature the process is favourable. In the fourth combination, ΔS_s and Q are negative. In this instance, the process is favourable below the critical temperature and unfavourable above it. Adsorption type processes generally fall into the fourth category, whilst decomposition type processes tend to fall into the third category.

Both bulk and 2D vdW layers can exist in a stable configuration when held under the same conditions. This is owing the relatively small adhesive energies between layers due to vdW forces. If vdW layers were held together by covalent forces, the adhesion energies would be of the order of $\sim 100\times$ times greater (Richardson (1977); Brenner et al. (2002)). The 2D material is also expected to have a greater entropy than its bulk counterpart as flakes can be arranged in random distributions. As such, the value of the Gibbs free energy in the vdW system is far lower than for that of covalent systems. This lower thermodynamic penalty to exfoliation explains the stability of exfoliated vdW materials. The ability for both bulk and 2D vdW material to coexist is then explained by the presence of kinetic barriers between the two.

Present in real crystals are defects. The creation of these defects are inherently energetically unfavourable as they push a structure away from the energetically ideal configuration. Their presence is therefore made favourable by their entropic contribution, pushing the crystal away from a uniform configuration and as such increasing its entropy. The entropic contribution of a single vacancy decreases with increasing vacancy density, whereas the energy of their creation is more constant. As such, there is a thermodynamically favourable concentration of vacancies in a crystal associated with a minimum in the Gibb's free energy. This preferred concentration increases with temperature (Elliott (1998)).

2.3.2 Kinetics

Although the thermodynamic description of a process yields information on its feasibility and spontaneity, it often won't predict whether the process will take place. For example, despite graphite being the most stable form of carbon and the transition between diamond and graphite having a negative ΔG, diamond will not spontaneously transform into graphite at room temperature. The transition is prevented by kinetic barriers (Popov et al. (2019)).

Kinetic limitations are due to the need for a system to pass through a transition state or states in order to rearrange the material into the configuration found in the end product. These transition states will typically have a greater energy than either the initial or final state and as such sufficient energy is required to overcome the barrier presented by the transition state. This energy is typically provided in the form of thermal energy but can also be provided in other forms, e.g. light. There may be more than one possible transition state, with the most favourable path from initial to final state depending on conditions or the presence of a catalyst. This is true for Z-scheme solar water splitting which lowers the barrier to the water evolution reaction over the single step process by aligning the valence and conduction bands of two materials in such a way to maximise the thermodynamic potential of photogenerated holes and electrons. This is achieved by utilising electrons/holes photogenerated in the cathode/anode for hydrogen/oxygen evolution and allowing the recombination of holes in the cathode with electrons in the anode. This comes with the benefit of increasing the number of electrons in the cathode and holes in the anode with sufficient energy for the reaction. This effectively lowers the energetic barriers for hydrogen and oxygen evolution, catalysing the reaction (Ng et al. (2020)).

Catalysts act to lower the kinetic energy barriers to a reaction. As such, they increase the rate of the reaction by increasing the proportion of particles (electrons/holes/reactants) with sufficient energy to overcome the kinetic barrier. Given that the energetic distribution of particles follows an exponential Boltzman-like distribution, even small changes to the reaction kinetic barrier can significantly modify the reaction rate. At room temperature the decreasing of the activation barrier from 76 kJ mol^{-1} to 57 kJ mol^{-1} for the decomposition of hydrogen peroxide in the presence of an iodine catalyst results in a ~ 2000 fold increase in the reaction rate (Atkins et al. (2014)).

Defects on the surface of a material can be engineered to act as catalytic centres for a reaction. This is often the case for reactions where the surface adsorption or desorption of species acts as the rate limiting step such as catalytic water splitting (Laursen et al. (2012)). By introducing sites with different adsorption energies, the rates of these processes can be modified. The lifetime (τ) of a molecule on surface is given by

$$\tau = \tau_0 \exp(-E_a/RT), \tag{2.12}$$

where τ_0 is a constant, E_a is the adsorption energy per mole, R is the gas constant and T is temperature (Atkins et al. (2014)). By introducing sites which optimise the adsorption/desorption rates of reactants and/or products, the overall rate can be optimised.

Chapter 3

Materials and Methods

This chapter discusses the materials and methods used over the course of this PhD. The materials section describes the growth methods used to produce the vdW materials and the techniques used to prepare the materials in a state suitable for experimentation. The methods section covers the techniques utilised for hydrogen exposure and the means by which hydrogen-induced changes were determined and assessed.

Contents

3.1 Materials

The materials used to gather the results presented in this thesis are primarily the III-VI layered vdW semiconductors InSe and GaSe and the IV-VI layered semiconductor SnS_2. This section covers the growth methods used to produce these materials. This section then goes on to describe the methods used to prepare the samples for investigations of their interactions with hydrogen.

3.1.1 Material Growth

The vdW materials used were grown via two primary methods, the Bridgman method and physical vapour transport (PVT). The Bridgman growth was conducted by Prof. Zakhar Kovalyuk at the Institute for Problems of Materials Science, part of the National Academy of Sciences of Ukraine. The PVT growth was also conducted by the same institute with the quality of the produced material evaluated in Nottingham and reported in Kudrynskyi et al. (2020).

A schematic depiction of the Bridgman method is shown in Figure (3.1a). The apparatus consists of a sealed ampule with the ability to move freely between two temperature controlled ovens separated by a baffle. The ampule is loaded with feedstock material in the desired stoichiometric ratios. The ampule is then positioned in the hotter of the two ovens (upper) where the temperature is sufficient to melt the feedstock material. Once a melt is achieved, the ampule is slowly lowered through the baffle into the cooler (lower) oven. This oven is at sufficiently low temperature to crystallise the desired material. The crystallisation front, in a well controlled system, aligns with the baffle and can be controlled by varying the rate at which the

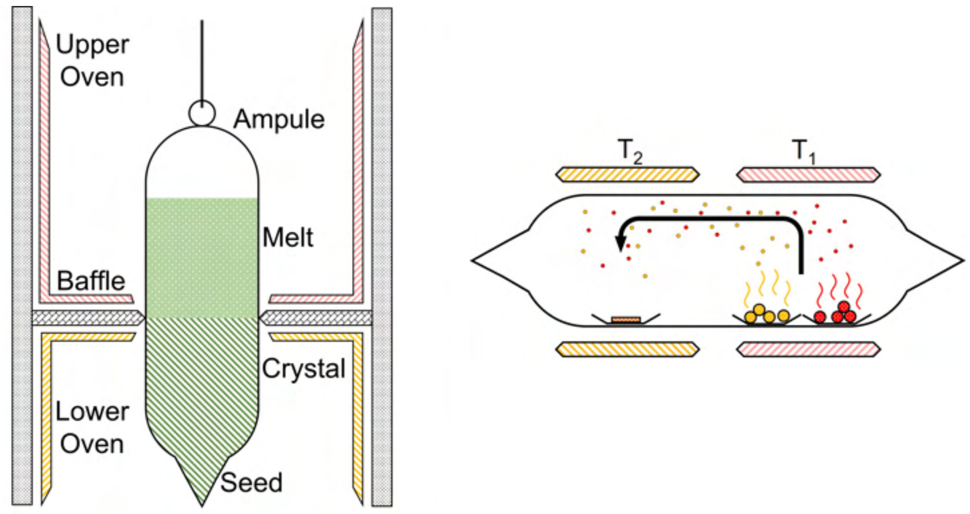

(a)

(b)

Figure 3.1: Schematic representations of vdW material growth using (a) the Bridgman method and (b) physical vapour transport.

ampule is lowered. A seed at the bottom of the ampule is used to initiate growth and set the crystallographic orientation. This method of growth can be used to produce large samples of a single crystal domain with well defined crystallographic orientations and stoichiometry.

The second growth method is PVT. This refers to growth methods where the feedstock material is first vaporised before being allowed to adsorb onto a substrate where the atoms can migrate and rearrange to form the desired material. Shown in Figure (3.1b) is a schematic representation of PVT growth in a sealed ampule. Other methods of PVT where a free-flowing carrier gas is present are also possible. In the sealed ampule configuration, the feedstock materials are loaded into one end of the ampule and heated until a vapour of atomic material is produced at temperature T_1. This material can then diffuse to the other end of the ampule where it adsorbs onto a prepared substrate held at temperature T_2 where $T_2 < T_1$. T_2 is at sufficient temperature to allow the migration of the atomic species such that they can rearrange into the preferred crystallographic positions. The SnS_2 used in Chapter 4 was grown with $T_1 = 650$ °C and $T_2 = 500$ °C

(Kudrynskyi et al. (2020)). This growth method results in a product on top of a substrate or, if grown in sufficient quantities, large flakes which can be free standing once removed from the ampule.

3.1.2 Sample Preparation

For the reliable study of vdW materials, it is desirable to transfer the as-grown bulk material to a suitable substrate. This enables the easy handling and identification of samples as well as producing a distribution of flakes from which different thicknesses can be sampled. The transferring of flakes to a suitable substrate is also desirable for certain techniques, such as XPS, the analysis of which benefits from a conductive substrate.

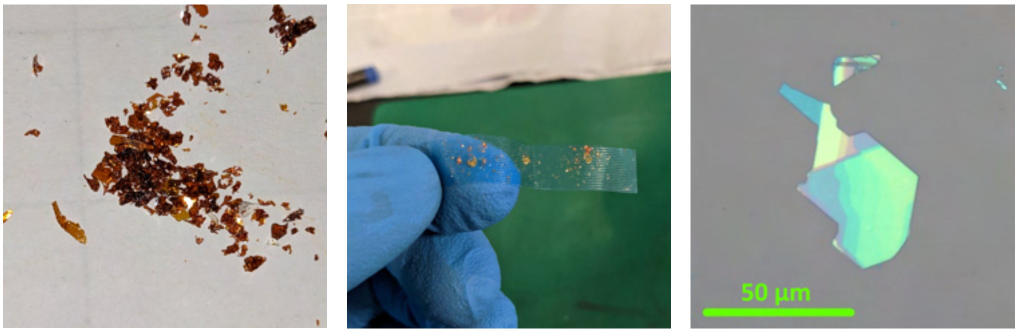

(a) (b) (c)

Figure 3.2: Stages of thin flake sample preparation via the exfoliation method. (a) Bulk SnS_2 material as grown via PVT. (b) SnS_2 material exfoliated on blue tape. (c) Thin Flake of SnS_2 stamped onto an SiO_2/Si substrate.

The flakes are first exfoliated from bulk material like that shown in Figure (3.2a) using tape, as shown in Figure (3.2b). Once on the tape, the flakes are then directly stamped onto a substrate by pressing the tape down onto the substrate before removing it. This leaves a distribution of flakes on the surface of different thicknesses and lateral sizes. Shown in Figure (3.2c) is an optical microscope image of a typical stamped flake of SnS_2. Variation in colour across the surface of the flake is associated with thickness-induced optical interference. In instances where precise positioning of a flake on the substrate is required, the flake can be transferred from the tape to polydimethylsiloxane (pdms), which is a transparent polymer. As pdms is transparent, it allows for the precise positioning of a flake with the aid of micro-manipulators under an optical microscope.

One substrate used for the studies was commercially acquired Si/SiO$_2$ wafers, with a nominal SiO$_2$ thickness of 300 nm. Alternatively, when a conductive or reference substrate is required, an Si/SiO$_2$/Ti/Au substrate is used. For this, an Si/SiO$_2$ wafer was commercially obtained and the ~10 nm Ti and ~40 nm Au layers were deposited via thermal evaporation.

An additional method of stamping was conducted by Anna Casey, a student of Dr. Fumin Huang at Queen's University Belfast to produce large area GaSe flakes on a gold substrate. This method relies on producing an extremely flat gold substrate (RMS roughness <1 nm) to increase the adhesion between the substrate and the vdW flakes. This resulted in a sample with flakes of 2 layers thick and with lateral sizes of 100s μm.

3.2 Experimental Methods

This section discusses the experimental methods used for exposing vdW materials to hydrogen in both the gas phase and in the form of H-ions, using a Sieverts apparatus and Kaufman ion source, respectively. This section then goes on to describe the methods used to characterise the samples before and after hydrogenation. These methods include: photoluminescence spectroscopy, Raman spectroscopy, X-ray photoelectron spectroscopy, ultraviolet photoelectron spectroscopy, angle resolved photoemission spectroscopy, atomic force microscopy, scanning electron microscopy, energy dispersive X-ray spectroscopy and transmission electron microscopy.

3.2.1 Sieverts

In order to expose vdW materials to hydrogen at pressures of between 1 bar and 60 bar and to quantify the resulting hydrogen uptake, a device known as a Sieverts was used. A Sieverts utilises pressure measurements to determine the quantity of a gas in a known volume. By determining its deviation from an expected value, it can quantify gas uptake. This requires the ability to convert the measured pressures into molar quantities. At low pressures, the ideal gas equation is suitable for this purpose. The ideal gas equation is as follows:

$$PV = nRT, \tag{3.1}$$

where P is pressure, V is volume, n is the molar quantity of the gas, R is the ideal gas constant, and T is the temperature. This equation is appropriate at low pressures where inter-molecular forces can be ignored. At higher pressures, inter-molecular forces become significant. As such, when examining pressures of up to 60 bar, a non-idealised expression must be used. A virial expansion of the ideal gas equation provides such an expression,

$$PV = nRT\left[1 + B\left(\frac{n}{V}\right) + C\left(\frac{n}{V}\right)^2 + ...\right], \tag{3.2}$$

where B and C are the first and second virial coefficient of the gas, respectively. For hydrogen B and C have values of 14.38 $\text{cm}^{-3}\text{mol}^{-1}$ and 370 $\text{cm}^{-6}\text{mol}^{-2}$, respectively (Goodwin et al. (1964)).

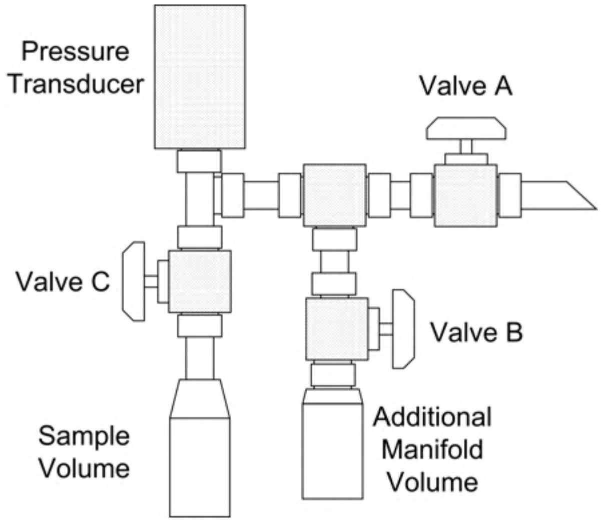

Figure 3.3: Schematic view of the Sieverts apparatus used for H_2 pressure based studies.

Figure (3.3) shows a schematic representation of a Sieverts, detailing the relative positions of its volumes and their separating valves. The sample is loaded into the sample volume and the whole system is then pumped down to a vacuum ($<10^{-3}$ mbar) through valve A. The system is then flushed with helium several times through valve A to remove trace gases. It is vital to the operation of the Sieverts that its volumes are precisely known. The manifold consists of the volume between valves A and C and its volume is known via calibration with ball bearings of a known size. The sample volume must be calibrated for each new sample. This is achieved using helium. First, the system is pumped down to a vacuum and valve C is closed. Helium is then allowed into the manifold though valve A, which is then closed. Valve C is then opened and the transducer records the pressure drop as the volume increases. This pressure drop is then used alongside the non-ideal gas equation to determine the sample volume. This is repeated over multiple pressures for the purpose of accuracy.

Once the sample space has been calibrated, quantitative uptake measurements can be made. All the volumes are first evacuated through valve A. Once evacuated, valve C is then closed and hydrogen is allowed into the manifold. Valve A is then closed and the pressure in the manifold noted. Using the non-ideal gas equation, the quantity of material in the manifold is then calculated. Valve C is opened to allow hydrogen into the sample space. After opening the valve the pressure is once again used to calculate the quantity of hydrogen in the new volume. Any discrepancy in the quantity of gas before and after the opening of valve C can then be attributed to hydrogen adsorption/absorption in the sample.

3.2.2 Kaufman Ion Source

In order to explore more reactive and potentially more penetrating forms of hydrogen, exposures using hydrogen-ions were also conducted. These exposures were accomplished using a Kaufman ion source, a system originally developed as a high efficiency rocket engine but with qualities which make it well suited to producing controlled exposures of H-ions (Kaufman (1961)). These qualities are: a controllable mono-energetic beam of ions, controllable and measurable ion flux, and a high ratio of H^+ ions to H_2^+ ions of 0.0291 (Bauer and Beach (1947)).

Shown in Figure (3.4) is a schematic representation of the Kaufman ion source illustrating the key components of its operation. Hydrogen gas is fed into the chamber on the right where it is ionised via collisions with electrons emitted by a thermionic element. A magnetic field generated in the chamber confines electrons to magnetic flux lines extending their path lengths and increasing the efficiency of the source. Ionised hydrogen species then diffuse in the chamber towards a set of accelerating grids, set at a predefined voltage to produce the mono-energetic ion beam. This beam is oriented towards the sample. The sample is grounded so that ions upon reaching the surface can acquire an electron and become neutral.

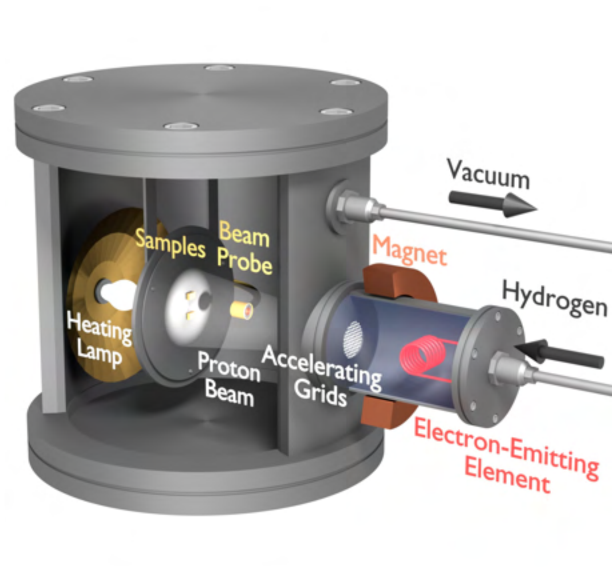

Figure 3.4: Schematic view of the Kaufman ion source used for exposures to H-ions and for some low pressure H_2 exposures.

The depth to which ions are implanted in the sample depends on sample composition and the beam energy. The behaviour of the hydrogen once in the sample will then depend on the nature of the interaction with the sample. The beam flux is determined via a probe in the path of the beam, which measures the current incident on a known area. Heating is achieved via an infra-red heat lamp positioned behind the sample mounting plate. When in operation the primary chamber is under continuous pumping to remove any H_2 gas.

This chamber was also used for some H_2 exposures with the Kaufman ion source switched off and H_2 allowed to enter the main chamber through the accelerating grids. This was done to leverage the pressure gauges available in this system which operate at a lower range than those used for the Sieverts.

3.2.3 Optical Spectroscopy

Photoluminescence (PL) spectroscopy and Raman spectroscopy were used for the non-invasive and non-destructive probing of optical and vibrational properties. The PL and Raman measurements were conducted using a Horiba LabRAM HR spectrometer equipped with a confocal microscope, motorised XYZ stage, two excitation sources at $\lambda = 532$ nm and $\lambda = 632.8$ nm, and diffraction gratings of 150 g/mm and 1200 g/mm. The operation for both PL and Raman spectroscopy is described here.

Photoluminescence Spectroscopy

PL spectroscopy works on a principle of exciting electrons in a material from the valence band to the conduction band using light. This generates an electron-hole pair which may then thermalise, diffuse, migrate or any combination of all three. After some time, characterised by the lifetime of the carriers, an electron hole pair can recombine and in doing so emit a photon. It is this photon which PL spectroscopy aims to detect. A simple picture of the PL process is shown in Figure (3.5a).

There can be variations on the process depicted in Figure (3.5a). For example, in 2D materials strongly bound electron-hole pairs known as excitons can be formed as shown in Figure (3.5b). The binding energy of the exciton lowers the energy of the system and consequently reduces the energy of the emitted photon. Another modification is via defect levels introduced to the band gap by defects in the material. This is shown in Figure (3.5c). The recombination of carriers from these levels can be radiative or non-radiative, and act to reduce the energy of the emitted photon and/or decrease the overall PL intensity.

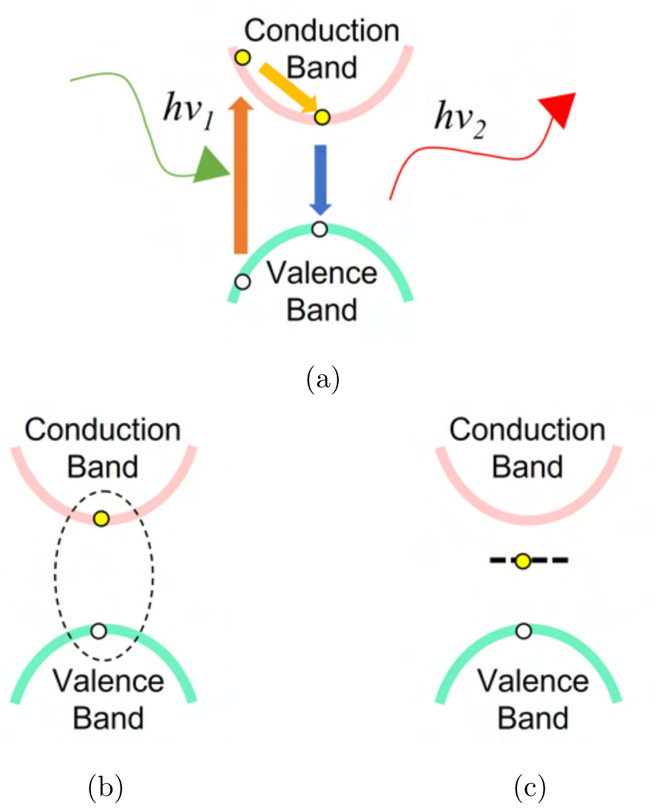

(a)

(b)

(c)

Figure 3.5: Sketches illustrating the origin of photoluminescence in a semiconductor, showing: (a) the excitation, relaxation and recombination processes, (b) an exciton and (c) position of an in-band gap defect state.

A schematic representation of a PL set-up is shown in Figure (3.6), illustrating its key components. First, is the excitation source, typically a laser. In this instance either a green frequency doubled Nd:YVO$_4$ ($\lambda = 532$ nm) or a red He-Ne ($\lambda = 632.8$ nm) laser can be selected. This laser beam then passes through a filter to adjust its intensity before being focused onto the sample via a microscope objective lens. This lens focuses the beam down to an area of $\sim$1 μm^2, increasing its intensity and allowing for highly selective sampling of the sample surface. The same objective lens is used to collect the photons emitted from the sample and passes them through to the edge filter. The emitted photons can pass through the edge filter, which is selected to block passage of the laser to the spectrometer, as their energy is less than that of the laser. They then pass through a confocal hole which allows for the probing to different depths within the sample.

Finally, the emitted photons arrive at the diffraction grating, splitting the light into its spectral components where they are then recorded via a linear detector array. This detector can either be a charge coupled device or an InGaAs array, depending on the spectral regions of interest.

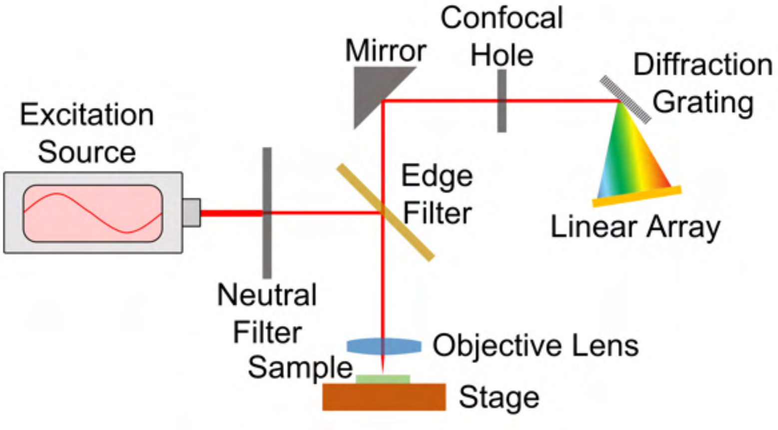

Figure 3.6: Schematic representation of a spectrometer suitable for PL or Raman spectroscopy.

The PL response can be mapped across the surface of the sample by utilising an X-Y motorised stage. In this mode, spectra are recorded sequentially in a grid pattern across the sample. The intensity of specific spectral regions or the position of specific peaks can then be displayed as a heatmap or as individual spectra.

A helium cold finger cryostat can also be incorporated into the system. For this, the sample is loaded into the cryostat and fixed to a copper slug. When sealed, the cryostat is then pumped down to a vacuum ($<10^{-6}$ mbar). A stream of helium vapour from a liquid helium dewar is then passed through copper pipes in contact with the underside of the slug, cooling it and consequently the sample. Through the presence of a heater and by controlling the flow of helium, the temperature in the cryostat can then be varied from temperatures as low as 4 K up to room temperature. A window in the lid of the cryostat allows for optical measurements of the sample.

Raman Spectroscopy

Raman spectroscopy relies on the creation or annihilation of a phonon to modify the energy of the incident photon. This creation or annihilation conserves both energy and momentum as per the following equations:

$$\hbar\omega_e = \hbar\omega_i \pm \hbar\omega_q \tag{3.3}$$

and

$$\hbar\mathbf{k_e} = \hbar\mathbf{k_i} \pm \hbar\mathbf{q}, \tag{3.4}$$

where $\hbar\omega_e$ is the energy of the emitted photon, $\hbar\omega_i$ is the energy of the incident photon, $\hbar\omega_q$ is the energy of the phonon, $\mathbf{k_e}$ is the wave vector of the emitted photon, $\mathbf{k_i}$ is the wave vector of the incident photon and $\mathbf{q}$ is the wave vector of the phonon. The ± here refers to the two different configurations of phonon annihilation and creation, which correspond to the anti-Stokes and Stokes processes, respectively. The Raman results presented as part of this thesis were conducted in the Stokes configuration.

Despite the differences between Raman and PL processes, the experimental setup is very similar, to the extent that the same system can be used for both. The most significant change is the requirement to change the diffraction grating used for the dispersion of the re-emitted light. For the PL studies a grating of 150 g/mm was used whereas for Raman studies a grating of 1200 g/mm was used. This results is a greater dispersion of the light and consequently allows for the viewing of the much narrower Raman features. However, using a more dispersive grating comes with the drawback of reducing the signal intensity incident on the detector.

3.2.4 Electron Spectroscopy

Electron spectroscopy techniques probe the properties of a material utilising the photoelectric effect. They include X-ray photoelectron spectroscopy (XPS), ultraviolet photoelectron spectroscopy (UPS) and angle resolved photoemission spectroscopy (ARPES). These techniques all probe the electronic properties near the surface of a material, with differences in their equipment/operation making each one more or less suited to studying specific features.

XPS

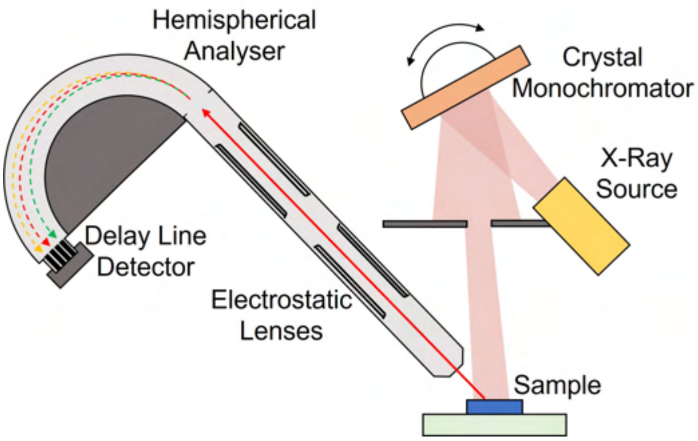

Figure 3.7: Generalised XPS schematic showing the common components utilised in most XPS systems.

The most common of the three techniques is XPS. The equipment used in XPS also the simplest of the three and most of the features present in an XPS system are also present for UPS and ARPES. Figure (3.7) shows a schematic description of an XPS system. The X-rays are first generated by an X-ray anode which emits X-rays upon electron bombardment from an electron emitting source. The material used for the X-ray anode determines the energy of the emitted X-rays, with energies between $h\nu = 132.3$ eV and $h\nu = 5417.0$ eV available. The most commonly used material is aluminium with the strong Al kα line at $h\nu = 1486.6$ eV (Watts and Wolstenholme (2019)). The X-rays are then monochromated by a quartz crystal utilising Bragg reflections from the crystallographic planes to disperse the X-rays. An aperture is then used to select for the correct Bragg reflected beam. The monochromated beam of X-rays is then directed onto the sample under investigation. The sample is mounted on a motorised stage to allow for precise positioning and for the investigation of specific regions of interest. When illuminated with X-rays the sample will begin to emit electrons with energies defined by selection rule allowed transitions. The resulting kinetic energy of the electrons is then described by the equation,

$$E_k = h\nu - E_B - W \tag{3.5}$$

where E_k is the kinetic energy of the electron, $h\nu$ is the photon energy, E_B is the binding energy of the electron in the material and W is the work function of the material. The emitted electrons then pass through a series of electrostatic lenses. These serve two purposes, to focus the electron beam and thus maximise its intensity, and to retard the electrons to an energy appropriate for the hemispherical analyser. When the analyser is operated in fixed energy mode, it is the variation in the retardation potential which controls the electron energies being sampled. The hemispherical analyser comes after the electrostatic lenses and consists of two concentric hemispheres held at different potentials, with the inner sphere held at a positive potential relative to the outer sphere. The electric field between the two spheres bends the path of the electrons around the analyser. The bending of the electrons is dependent of their kinetic energy and at the exit of the analyser the electrons are dispersed with lower kinetic energy electrons closer to the inner sphere and higher kinetic energy electrons closer to the outer sphere. The energy of the electrons which pass through the centre of the analyser is known as the pass energy and is given by the equation:

$$E = e\Delta V \frac{R_1 R_2}{R_2^2 - R_1^2}, \tag{3.6}$$

where E is the pass energy, e is the charge on the electron, ΔV is the voltage difference between the two hemispheres, R_1 is the radius of the inner sphere and R_2 is the radius of the outer sphere (Watts and Wolstenholme (2019)). This pass energy determines the extent to which the electrons are dispersed with a lower pass energy corresponding to a higher dispersion. With the electrons dispersed at the exit of the analyser, a multichannel delay line detector is used to sample the spatial variation in electron flux and convert it to an electrical signal to be read out by an analogue to digital converter. XPS systems are often operated in a swept mode whereby the retardation voltage is varied over the energetic region of interest to overcome data artefacts associated with the transmission function of the analyser and with variation across the delay line detector.

Typically, XPS requires strict vacuum conditions ($<10^{-8}$ mbar) for the electrons to have a sufficient mean free path for passage from the sample through the electrostatic lenses and analyser to reach the detector. However, it is often desirable to understand the chemical state of a surface whilst being exposed to a gas or vapour. For this to be achieved, a method for exposing the sample at higher pressures while maintaining the long mean free path through the electrostatic lenses and analyser is required. This is achieved in near ambient pressure XPS (NAP-XPS) with the use of a NAP cell and several differential pumping stages. Shown in Figure (3.8) is a NAP cell. The sample in the centre of the image is approached by a cone with a small hole at its tip. On the sample side of the cone the pressure can be

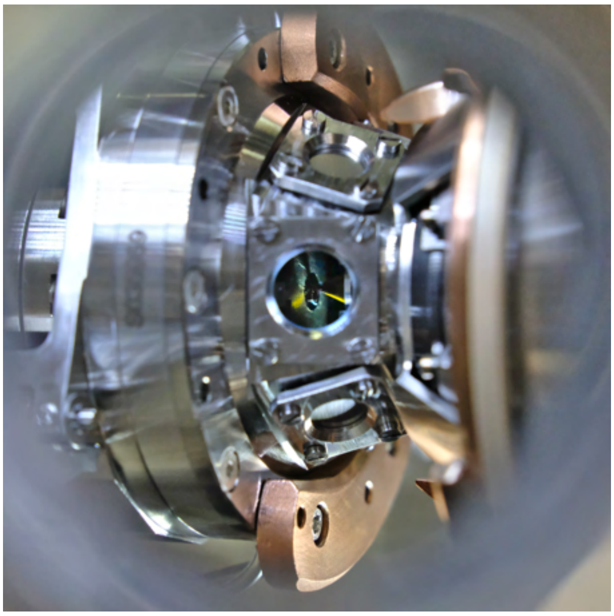

Figure 3.8: Image of the NAP cell in the SPECS Devi Sim NAP XPS at the University of Nottingham containing a GaSe sample on an Au/Ti/SiO_2/Si substrate for NAP-XPS. This image was taken through the optical port used for sample illumination with the Sciencetech A1 Light Line solar simulator.

of several mbar whilst on the other side of the cone the pressure is several orders of magnitude lower. By minimising the distance between the sample and cone, the distance travelled by the electrons in the cell is minimised thus allowing for XPS in environments where the mean free path would traditionally be considered too short. The window through which the sample is imaged in Figure (3.8) allows for the illumination of the sample via a solar simulator. A 1.5 global solar air mass solar simulator replicates the conditions used for standardised solar photovoltaic measurements.

Two separate XPS systems were used as part of this PhD. The first was a Kratos AXIS ULTRA equipped with a monochromated Al kα source. This system was operated with the use of a charge neutraliser filament, a hybrid aperture, a 300×700 μm spot size, and scans were performed with a 20 eV pass energy. This first system was employed for the study of SnS_2 and InSe is Chapter 4 and Chapter 5. The second system was a SPECS

Devi Sim near ambient pressure XPS equipped with a Phoibos 150 near ambient pressure hemispherical analyser, an Al kα source and a Sciencetech A1 Light Line solar simulator. This system was used to conduct NAP and vacuum measurements XPS on the GaSe sample in Chapter 6.

UPS

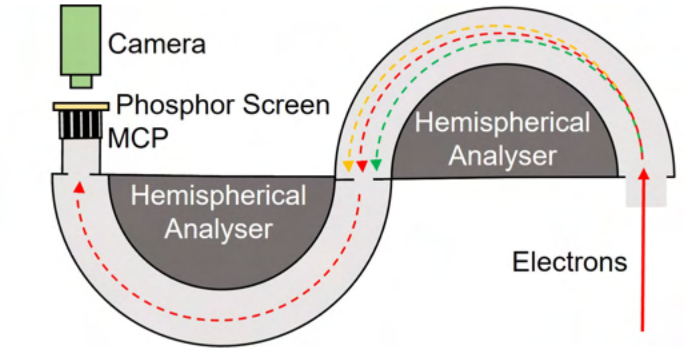

Figure 3.9: Sketch of a dual hemispherical analyser used for energy dispersion and spherical aberration correction in UPS and ARPES experiments.

Much like XPS, ultraviolet photoelectron spectroscopy (UPS) samples the electron flux from a sample due to the photoelectric effect. The difference between XPS and UPS lies in the energy of the exciting photons. In UPS the photon energy is much lower (∼100x) than in XPS. The advantage of using lower energy photons in UPS is the increased sensitivity to states closer to the vacuum level as a result of an increased interaction cross-section for transitions with energies closer to that of the incident photon. The nano electron spectroscopy for chemical analysis (Nano-ESCA) equipment used for the UPS studies in this thesis use photons of energy $h\nu =$ 21.219 eV, corresponding to the He Iα emission line from a helium discharge lamp. After sample irradiation, electrons emitted from the sample are then extracted by a large electric field (67,000 Vcm^{-1}), which ensures the efficient sampling of electrons and allows for the capture of electrons with zero kinetic energy. This element of the system in known as the extractor and acts as the first lens element for the system. After this first element, a series of electrostatic lenses are used to form either a real space or reciprocal space image (detailed in the next section) and for retarding the kinetic energy of the electrons. This image is then transferred through two hemispherical analysers, as shown in Figure (3.9). A slit located in-between the two analysers selects for electrons of a given energy whilst the second hemisphere corrects for aberrations introduced by the first. The image is then focused onto a screen to allow for real space or reciprocal space imaging. A real space or reciprocal space UPS spectrum can then be constructed by changing the energy of electrons which pass through the slit between the two analysers. For the results presented as part of this thesis, UPS was conducted utilising the same equipment as described for ARPES.

ARPES

Angle resolved photoemission spectroscopy adds to the functionality of UPS by preserving the in-plane momentum components of the electrons emitted from the sample. It does this by measuring the emission angle and kinetic energy of the photoelectrons. The in-plane k-vector ($\mathbf{k}_{\|}$) of the electrons is related to the emission angle (θ) relative to the surface by

$$|\mathbf{k}_{\|}| = \frac{1}{\hbar}|\mathbf{P}_{\|}| = \frac{1}{\hbar}\sqrt{2m_e E_k}\sin\theta, \tag{3.7}$$

where $\mathbf{P}_{\|}$ is the free electron momentum, m_e is the electron mass, and E_k is the electron kinetic energy (Damascelli (2004)). As the in-plane momentum component is conserved, the electron momentum can be inferred from the emission angle and electron kinetic energy. The out of plane momentum component is not conserved however due to the breaking of crystal periodicity at the surface. Instead, ARPES probes a section of the Brillouin zone as set by the photon energy. The selected momentum (k_z), in a free electron model, is described by

$$k_z = \sqrt{\frac{2m(E_k \cos^2\theta + V_0)}{\hbar^2}}, \tag{3.8}$$

where m is the electron mass, E_k is the electron kinetic energy, θ is the emission angle and V_0 is the inner potential (Plucinski et al. (2003)). Additionally, the out of plane component contributes a broadening to spectrum. This broadening is of the order

$$\Delta k_\perp \sim \lambda_{fe}^{-1}, \tag{3.9}$$

where $\Delta k_\perp$ is the uncertainty along the out of plane direction and λ_{fe} is the mean free electron path (Mitsuhashi et al. (2016); Strocov (2003)). With reference to a universal electron curve describing the mean free path of electrons in solids and a photon energy of 21.219 ev, the uncertainty for the Nano-ESCA can be said to be of the order $\Delta k_\perp = 0.1$ Å^{-1} (Chusuei and Goodman (2013)),

The work of the Nano-ESCA optics is to determine the emission angle and kinetic energy of the photoelectron such that their momentum's can be determined. A sketch of the electron trajectories is shown in Figure (3.10). The first part of this process is the same as for UPS with the emission of electrons resulting from the illumination of the sample with photons of energy $h\nu = 21.219$ eV. The electrons are then extracted from the surface by the extractor which forms the first lens element of the system. A contrast aperture can then be used to restrict the angular distribution of the electrons. The first transfer lens then focuses the electrons into the

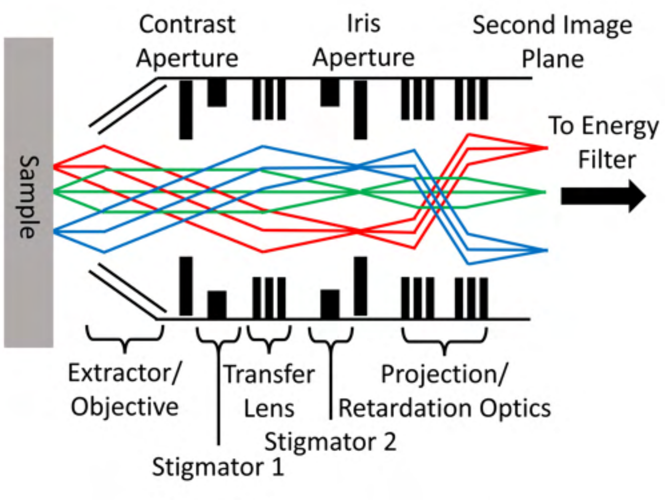

(a)

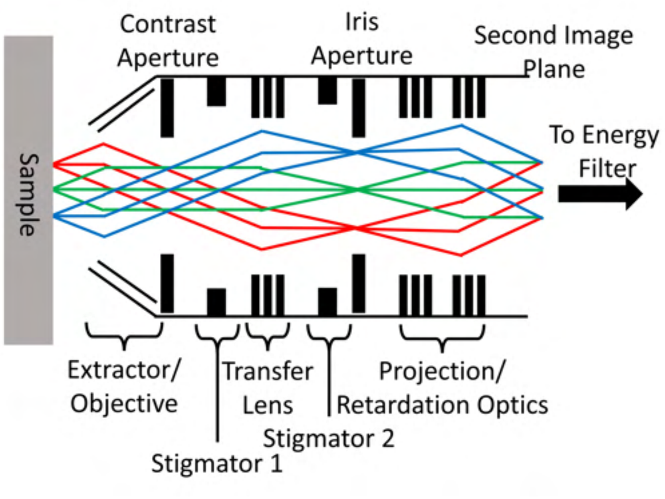

(b)

Figure 3.10: Ray traced diagram indicating the path of electrons through the Nano-ESCA optics in both (a) real space and (b) reciprocal space. After passing through these optics, the electrons enter the energy filter shown in Figure (3.9).

first image plane and the two stigmators can be used to correct the electron trajectories through the optical system. In the first image plane sits a iris which is used to select for electrons emitted from a given portion of the sample in real space. The projection/retardation optics have two functions, the first is to project either a real space or reciprocal space image into the second image plane, and the second is to reduce the electron kinetic energies such that the correct energies pass through the slit in the energy filter. A series of transfer lenses are then used to pass the electrons to and between the two hemispherical analysers. The first hemisphere serves the purpose of dispersing the electrons by energy, as with XPS. An aperture positioned at the exit of the first hemisphere then selects for electrons in a specific energy range, and determines the energy resolution of the measurement. The first hemispherical analyser introduces spherical aberrations into the system. The purpose of the second analyser is then to correct for these aberrations. With the same dimensions and with the pass energy set to the same value as the first analyser, the second analyser allows for the electrons to complete their Kepler orbits and reverses the aberrations introduced by their passage through the first hemisphere. The reciprocal space or real space image is then projected onto a multi channel plate (MCP), which amplifies the electron flux before being accelerated onto a phosphor screen for the conversion into photons. These are then detected by a camera.

Both ARPES and UPS were conducted at the University of Nottingham utilising a Scienta Omicron Nano-ESCA II equipped with a Hg discharge lamp for sample positioning and optical corrections. ARPES and UPS measurements were conducted using photons generated by a Focus HIS 14 HD helium discharge lamp equipped with a focusing mirror to achieve a 170 FWHM spot size and a photon flux of 2×10^{12} photons/second/mm^2.

3.2.5 Additional Techniques

This section considers the techniques utilised in this PhD which were primarily conducted by another individual and from which relatively straightforward results and analysis were gained. As such, a brief description of their operation is provided alongside references to detailed resources describing their operation.

Atomic Force Microscopy

Properties of and changes in the surface morphology of a material can provide powerful insights into the behaviour of a material and its interactions with hydrogen. Atomic force microscopy (AFM) is one of the most straightforward methods for characterising this morphology due to its ability to image areas of 100s μm in size whilst also retaining the ability to resolve features on the scale of the crystallographic lattice. This is achieved by monitoring the deflections and changing oscillations in a cantilever with an atomically sharp tip at one end induce by sample-tip interactions. AFM also provides additional utilities in the form of: compositional sensitivity (phase data), electrical conductivity characteristics and work function measurements (Kelvin probe force microscopy). A detailed description of the operating principles of AFM can be found in Johnson et al. (2009).

The AFM used for the study of SnS_2 in Chapter 4 and GaSe in Chapter 6 was conducted using an Asylum Research Cypher-S. This system is equipped with an optical microscope for the location of flakes and was operated in either non-contact tapping or contact mode. The NuNano Scout 70 Si AFM tip with a radius of < 10 nm was used in non-contact mode and a NuNano Spark 70 Pt tip with a radius of < 30 nm was used in contact mode.

Scanning Electron Microscopy and Energy Dispersive X-ray Spectroscopy

SEM is a common technique used to image the surface of a samples with spatial resolution better than that achievable using traditional optical microscopes. This is due to the comparatively shorter wavelengths of electrons

(0.1 Å at 10 keV) than that of visible light (450 nm for blue light), dramatically improving the diffraction limited resolution. SEM requires the focusing of an electron beam at a given energy onto the sample. The electrons can then impart sufficient energy to electrons within the sample to eject them from their atomic orbitals in an inelastic process. These electrons are known as secondary electrons. Alternatively, the electrons can be elastically back-scattered towards the incoming electron beam. A detailed description of the principles of SEM can be found in Akhtar et al. (2018).

EDX utilises much of the same equipment as SEM, to the extent that they are often integrated into the same device. As with SEM, a beam of electrons is accelerated and focused onto the sample. Electrons incident on the sample dissipate their energy into it. As such, electrons are ejected from their atomic orbitals and leave behind empty electronic states. With the atoms in an excited state, electrons from a higher energy shell can relax into the empty level and emit a corresponding X-ray. The emitted X-rays have well-defined energies associated with energy transitions within an atom allowing for their identification. A detailed description of the principles of EDX can be found in Abd Mutalib et al. (2017).

SEM and EDX was conducted using an JEOL 7000F FEG-SEM equipped with a field emission electron gun and the facility to image both secondary and backscattered electrons and equipped with an Oxford Instruments INCA Wave 700 WDS System for high resolution elemental mapping.

Transmission Electron Microscopy

TEM considers the electrons transmitted through a sample of interest. As such, it requires a different experimental arrangement with the electron beam directed towards one side of the sample and an electron detector positioned on the other side to detect the transmitted electrons.. Due to the requirement for transmission of electrons, the sample must be suspended to allow the free passage of electrons. The TEM images in Chapter 4 were conducted using high angle annular dark field scanning TEM (HAADF STEM), whereby the scanning beam is detected when deflected away from the original trajectory preferentially by atoms with a high atomic number. A detailed description of the principles of TEM can be found in Egerton et al. (2005).

Samples were first ion milled in a Zeiss Crossbeam 550 (HR-CAT-SEM) after being capped with Pt. The TEM analysis was then conducted using a JEOL 2100F FEG-TEM equipped with an Oxford Instruments INCA EDX system.

Chapter 4

Hydrogen - Tin Sulphides Interaction

Discussed in this chapter are the interactions between hydrogen and tin monosulphide and tin disulphide. The ability to produce a heterostructure based on these interactions is demonstrated. This chapter follows the reporting of results in (Felton et al. (2022)), with implications ranging from the chemical conversion of SnS_2 into SnS to the formation of SnS_2/SnS heterostructures with atomically flat interfaces and tunable electronic, vibrational and optical properties. The interaction of SnS_2 with H-ions leads instead to the conversion of SnS_2 to β-Sn. Density functional theory (DFT) is used to provide a theoretical basis for the experimental results and a fundamental understanding of the interaction of hydrogen in Sn-S compounds. These findings offer a route for engineering physical properties at the nanoscale for semiconductor technologies based on earth-abundant elements, such as Sn and S, and facilitate their use across a wide range of emerging technologies. Experimental work was contributed by Elena Blundo (University of Rome) and myself, with theoretical input from Dr. Sanliang Ling (University of Nottingham). The TEM and SEM studies were conducted in collaboration with the Nanoscale and Microscale Research Centre (University of Nottigham).

Contents

4.1 Chemical Interaction with H_2

Amongst 2D materials, vdW crystals based on Sn and S offer an interesting platform for hydrogen studies. They can exist in a variety of stoichiometries, lattice structures, and with Sn-atoms in the Sn^{4+}, Sn^{2+} and Sn^0 oxidation states. Shown in Figure (4.1) is a selection of materials from the Sn-S family, illustrating their diverse structural properties. Contained within the tin-sulphur materials family, are a number of 2D materials including the elemental-Sn material stanene, alongside mixed Sn-S compounds such as SnS ($Pnma$) and SnS_2 ($P-3m1$); the latter two of which are of particular interest as they represent the most stable phases for their respective stoichiometries (Burton and Walsh (2012)). This opens up the possibility that by altering the stoichiometry of these materials and the oxidation state of the Sn atoms that one vdW material might be converted into another.

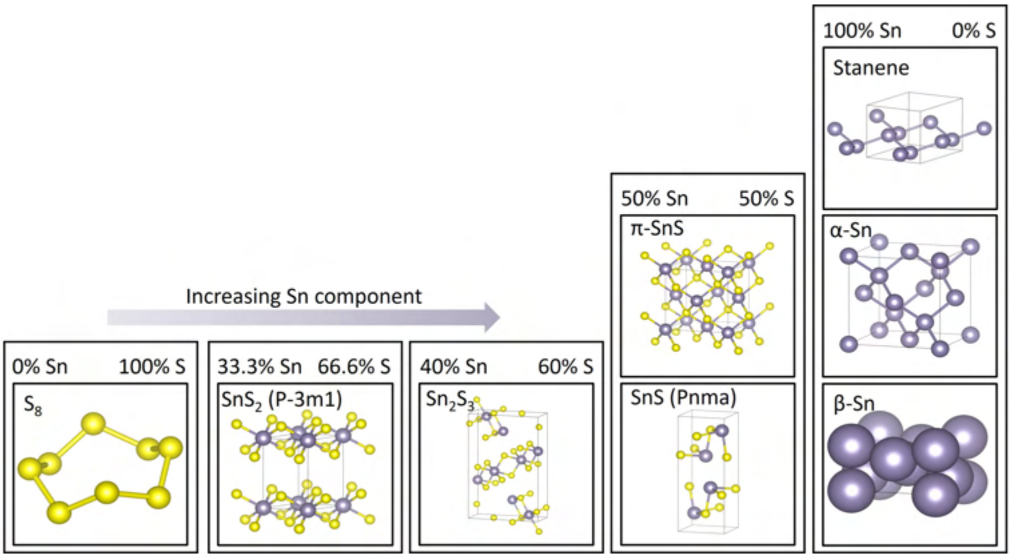

Figure 4.1: The structures of a sample of Sn and S containing materials. Materials further to the right have an increased Sn component and materials closer to the bottom are more stable.

One candidate for accessing the stoichiometric and oxidation degrees of freedom of the Sn-S system is hydrogen. Hydrogen is an excellent candidate for facilitating this conversion as it form strong bonds with sulphur atoms, and forms the relatively stable H_2S molecule. Given these preconceptions, the following expression describing a possible reaction of SnS_2 with H_2 can be proposed:

$$\mathrm{SnS_2} + \mathrm{H_2} \longrightarrow \mathrm{SnS} + \mathrm{H_2S}, \tag{4.1}$$

where H_2S is in the gas phase, allowing for its removal and leaving behind the newly formed SnS. This is just one potential reaction between H_2 and SnS_2, others can also be suggested, including: the complete reduction of SnS_2 to elemental Sn and H_2S, the partial reduction of SnS_2 to Sn_2S_3, the formation of hydride complexes, and some combination of some/all of these.

To better understand the interactions between hydrogen and the materials SnS_2 and SnS, samples of SnS_2 were prepared on a combination of Au and SiO_2 substrates. These samples were then exposed to a continually refreshed supply of H_2 at pressures from 5×10^{-4} to 6×10^{-3} mbar and temperatures between 150 and 300 °C for anywhere from 3.5 to 8 hours. These samples were then analysed utilising the techniques of X-ray photoelectron spectroscopy (XPS), scanning electron microscopy (SEM), energy dispersive X-ray spectroscopy (EDX), atomic force microscopy (AFM), transmission electron microscopy (TEM), Raman spectroscopy and photoluminescence (PL) spectroscopy, with additional theoretical input in the form of density functional theory (DFT) calculations. A further set of samples were exposed to H^+ via a Kaufman ion source at 150 °C with a beam energy of between 8 and 12 eV for total doses of between 8×10^{15} and 6×10^{16} ions cm^{-2} in order to assess the effect of highly reducing H-ion species on SnS_2 samples.

4.2 SnS_2 thin films exposed to H_2 and H-ions

The exposure of SnS_2 flakes to either H_2 or H-ions induces a visible change in their colour and contrast. Figures (4.2a) and (4.2b) illustrate a typical transformation in SnS_2 flake colour. It can be seen that the shape of the flake remains unchanged by the exposure, but the flake undergoes a colour shift. In this instance, the originally green colour (center of flake Figure (4.2a)) region is transformed into a light-orange tone (center of Figure (4.2b)), whilst an originally light red region takes on a yellow-orange colour. The exact nature of the shift is dependent on the original, interference-induced, colour of the flake. Similar effects were observed on several samples exposed at temperatures of up to 250 °C. However, at temperatures of 250 °C a strong etching of SnS_2 is observed alongside the appearance of dark-spots on the flake surface. When the exposure temperature is increased to 300 °C, the flakes are entirely etched away.

Flakes of SnS_2 exposed to H-ions from a Kaufman ion source behave in a different way to those exposed to H_2. Figures (4.2c) and (4.2d) show SnS_2 flakes before and after exposure to H-ions, respectively. A typical response is shown with discolouration of the exposed flakes alongside the formation of black micron-sized plateau features associated with a disordered and rough surface. Additionally, flakes which appear visually thin in microscope images undergo a significant etching and occurs over a wide range of temperatures, hydrogen doses and for flakes on both Au/Si and SiO_2/Si substrates.

SEM provides a higher spatial resolution than optical images and when used in conjunction with EDX can correlate surface features with compositional variations. Figures (4.3a), (4.3b) and (4.3c) show SEM images of control, H_2 exposed and H^+ exposed SnS_2 with the S/Sn atomic ratios,

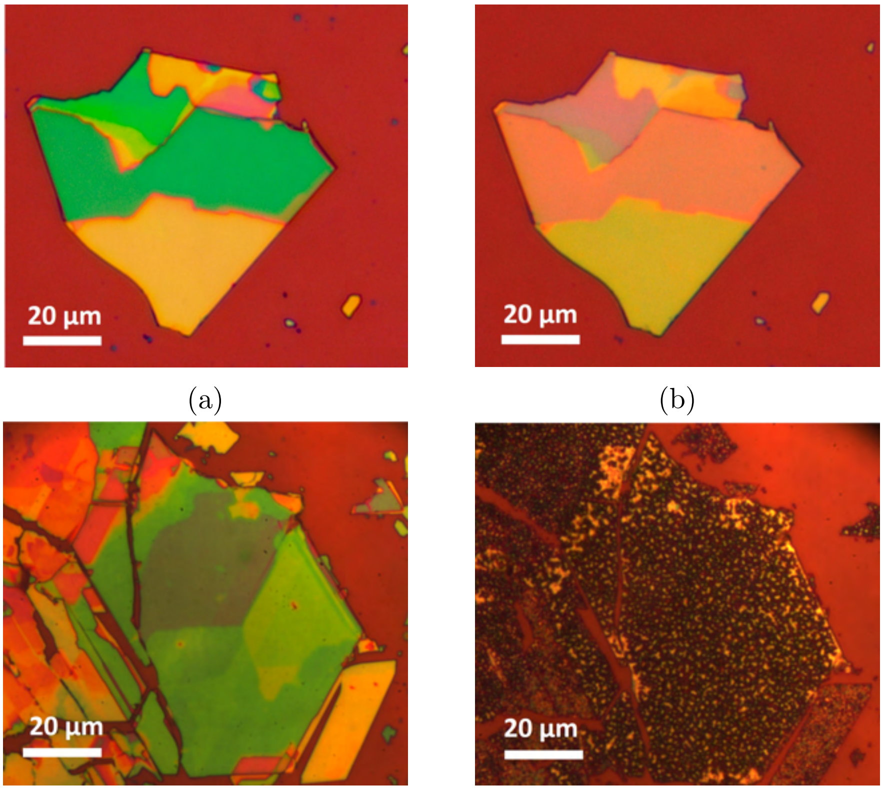

(a) (b)

(c) (d)

Figure 4.2: Optical images of SnS_2 flakes which have been mechanically exfoliated onto Au/Si substrates: (a) before exposure to H_2, (b) after exposure to H_2 (7×10^{-4} mbar, 150°C, 7.5 hours), (c) before exposure to H-ions and (d) after exposure to H-ions (12 eV, 6×10^{16} ions cm^{-2}, 150 °C, 3.5 hours).

as determined via EDX, labelled for specific sites. The trend in the SEM images is much like that in the optical images with no obvious changes between the surface morphologies of either the control or H_2 exposed samples, whilst there is a significant roughening of the H^+ exposed samples with the plateau features once again visible. The EDX ratios reveals more about the changes. In the control sample (treated at the same temperature under vacuum in the absence of hydrogen) the S/Sn ratio sits at between 1.83 and 1.92, close to the expected value of 2 for SnS_2. The deviation from the expected value is attributed to the overlap of EDX peaks with those from the substrate. In the H_2 exposed sample the ratio varies between 1.55 and 1.75. Importantly, this value is always greater than the 1 expected in SnS.

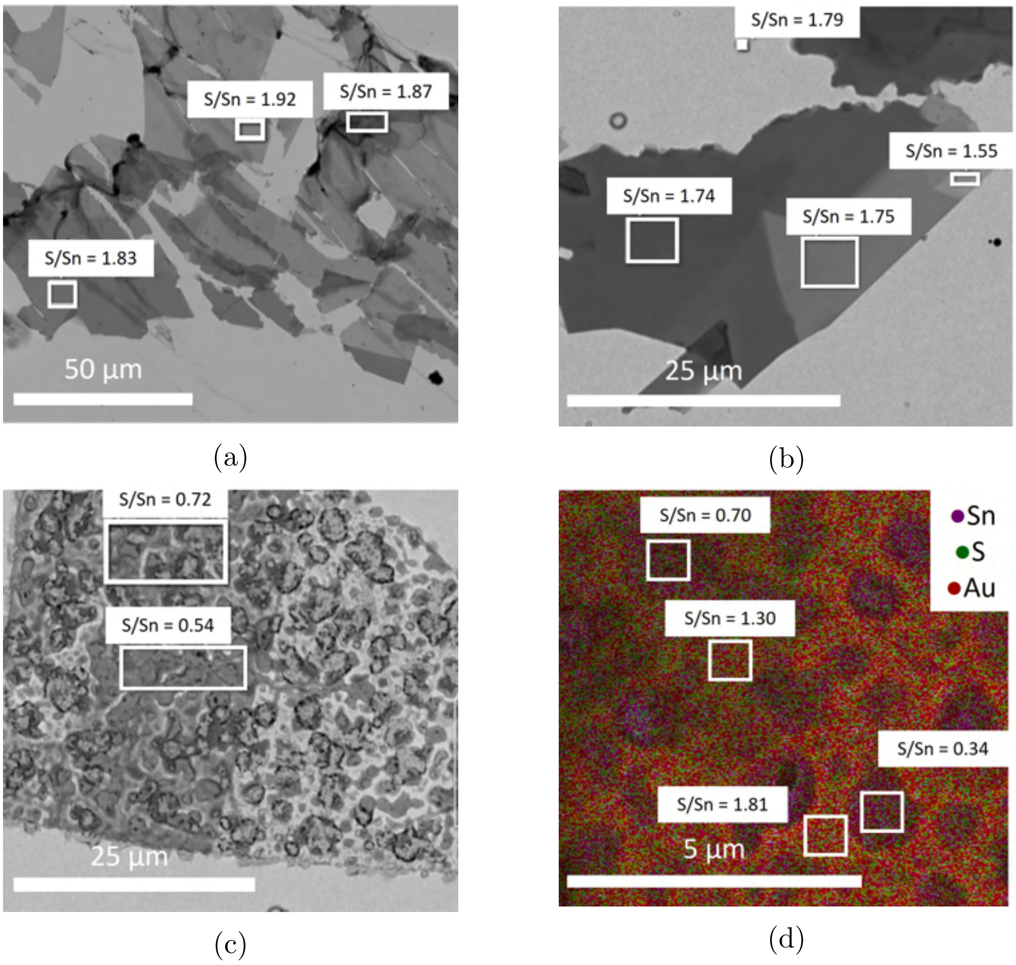

(a) (b)

(c) (d)

Figure 4.3: SEM images of, (a) a control SnS_2 sample, (b) SnS_2 sample exposed to H_2 (7×10^{-4} mbar, 150°C, 7.5 hours) and (c) an SnS_2 sample exposed to a H-ion beam (12 eV, 6×10^{16} ions cm^{-2}, 150 °C, 3.5 hours), with insets corresponding to the S/Sn atomic ratio determined by EDX. (d) EDX map of SnS_2 exposed to a H-ion beam (8 eV, 8×10^{15} ions cm^{-2}, 150 °C, 1.5 hours).

EDX samples a vertical volume extending into the substrate meaning any underlying SnS_2 would skew the ratio towards 2. This also explains the decreasing value of the ratio with decreasing flake thickness (AFM of flake in Figure (4.3b) shown in Figure (4.8)). For the H^+ exposed sample the ratio is seen to drop below 1 to between 0.54 and 0.72. Unlike the other two samples, the H-ion exposed flake also exhibits significant spatial variation which is not associated with changes in thickness. EDX mapping of a H-ion exposed sample, shown in Figure (4.3d), shows how the variation in composition maps onto the morphology. The plateau features exhibit a very low S/Sn ratio of <1 whilst the inter-plateau regions produce much higher ratios of >1 and in one instance close to that of the control sample. The low sulphur content of the plateaus is inconsistent with SnS and is instead indicative of elemental Sn as the ratio is sufficiently bellow 1 to be unexplained fully by substrate overlap in the EDX spectrum which slightly underestimates the S/Sn ratio.

4.3 Chemical Conversion of SnS_2 by H_2 and H-ions

It is clear from the optical images (Figure (4.2)) and the SEM/EDX data (Figure (4.3)) that the exposure of SnS_2 to either H_2 or H-ions induces a chemical change in the material which decreases its sulphur content. To further probe this change XPS was employed to give a better understanding of the chemical state of the constituent atoms. The ability for the Sn atom to exist in the Sn^{4+}, the Sn^{2+} and the Sn^0 oxidation states present in SnS_2, SnS and elemental-Sn, respectively, was exploited here.

Present in the XPS spectra of the samples are peaks associated with the core levels of Sn and S from the samples and Au from the substrates. Au can be used to calibrate the positions of the other peaks owing to its relatively high intensity and well defined peak positions. As already discussed, the Sn peaks are sensitive to changes in the chemical environment owing to its multiple oxidation states. Sulphur, however would be less sensitive to changes in the local environment, possesses a lower XPS cross-section and owing to its small spin-orbit splitting is harder to interpret. As such, the XPS studies of the samples focus on the changes to the Sn peaks.

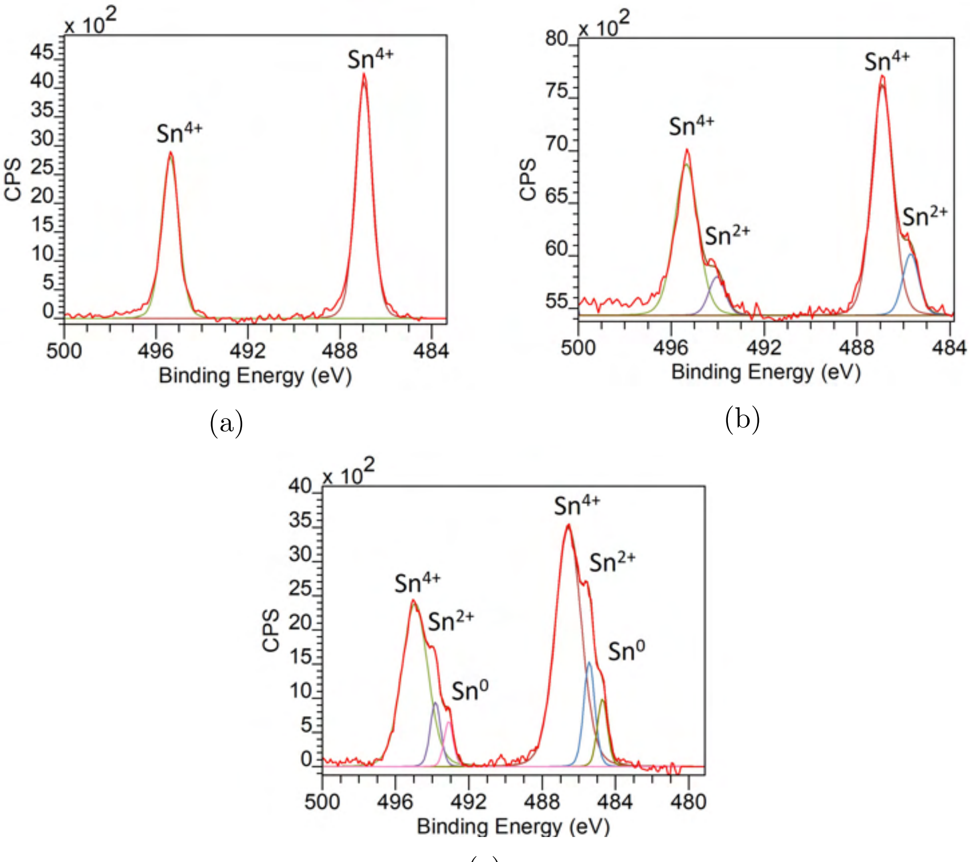

(a)

(b)

(c)

Figure 4.4: Peak fitting to the Sn 3d spectra of the (a) control sample, (b) H_2 exposed sample, and H^+ exposed sample. Labelled are the Sn oxidation states corresponding to each component. A Tougaard background and 50/50 Lorentzian Gaussian blend was used for the fitting.

Figure (4.4) shows the XPS spectra of the Sn 3d regions of the control SnS_2, H_2-exposed SnS_2, and H-ion exposed SnS_2 samples. In the control sample, the Sn 3d doublet is clearly visible: two well-resolved single lines can be seen at binding energies of 486.9 eV and 495.3 eV. The principle peak position at 486.9 eV is in agreement with the value of 486.7 eV for Sn^{4+} reported for SnS_2 in the literature, as is the 8.4 eV splitting (Reddy et al. (2015)). In the H_2 exposed sample, the Sn^{4+} doublet remains visible with its position un-changed. However, additional features appear on the low energy side of both components of the doublet. Specifically, these features appear at 1.0 eV and 1.2 eV below the Sn^{4+} low-energy and high-energy components, respectively (see Sn^{2+} components in Figure (4.4b)). The new features observed in the hydrogenated samples correlate with previous data for the Sn^{2+} peak in SnS where the Sn 3d component has a binding energy of between 0.9 eV and 1.3 eV less than the Sn^{4+} peak in SnS_2 (Reddy et al. (2015); Whittles et al. (2016); Moulder et al. (1992)).

For SnS_2 exposed to H-ions, the XPS spectra reveal more significant changes: the Sn^{4+} High-energy peak shifts to 486.6 eV, 0.3 eV lower than in the control sample, whilst the peak splitting remains at the expected 8.4 eV (Reddy et al. (2015)). Two additional components can also be seen at 485.5 eV and at 484.8 eV, 1.1 eV and 1.8 eV lower than the Sn^{4+} peak, respectively (see Sn^{4+} components in Figure (4.4c)). These peaks are assigned to the Sn oxidation states of: Sn^{2+} in SnS and the neutral Sn^0 states of elemental-Sn, in line with previously reported data for the Sn^0 peak in β-Sn (485.0 eV) and a Sn^{4+} - Sn^0 separation of 2.0 eV (Reddy et al. (2015); Moulder et al. (1992)).

Of the multiple flake ensembles examined via XPS, all showed a similar behaviour to those described above. None of the H_2 exposed samples revealed the presence of elemental Sn and in neither the H_2 nor the H-ion exposed samples could any traces of tin oxides be resolved. Given the mean free path suggested by the universal electron curve for the Sn 3d electrons of approximately 1 nm, and in conjunction with the later TEM measurements, the fact that SnS_2 can be seen in the H_2 exposed samples indicates a non-uniform distribution of SnS between flakes (Chusuei and Goodman (2013)).

4.4 Formation of an SnS/SnS$_2$ Heterostructure

The reduction of SnS$_2$ by H$_2$ and H-ions is clear from the XPS data. However, what is not clear is the phases which SnS$_2$ has been reduced to. After all, the Sn^{4+} and Sn^{2+} oxidation states present in SnS$_2$ and SnS, respectively, are also present in the mixed oxidation sates of Sn$_2$S$_3$. Structure sensitive techniques are necessary to better understand the make-up of the newly produced materials. To this end, Raman spectroscopy and cross-sectional TEM were employed.

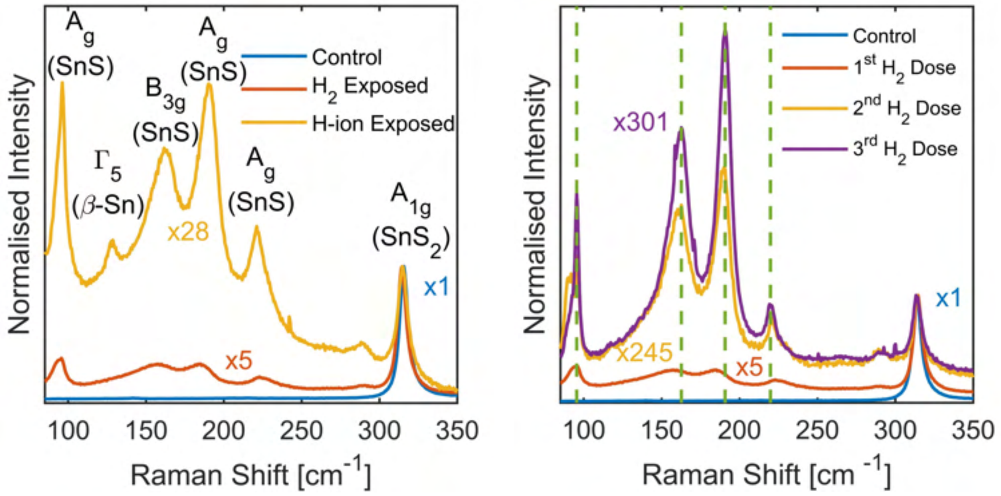

(a) (b)

Figure 4.5: (a) Raman spectra of SnS$_2$ samples (control and hydrogenated samples) at 300 K and $\lambda = 632.8$ nm. (b) Raman spectra of SnS$_2$ repeatedly exposed to H$_2$. The green dashed lines indicate the positions of SnS peaks after the third dose.

Raman spectra, shown in Figure (4.5a), reveal structural phases present within the control, H$_2$ exposed and H-ion exposed samples. In the control sample only one feature is observed, the Raman peak at 314.5 cm^{-1} which is assigned to the A$_{1g}$ mode of SnS$_2$. This compares favourably to previous reports of this mode between 314.3 cm^{-1} and 318 cm^{-1} (Mead and Irwin (1976); Ding et al. (2020); Sriv et al. (2018)). The A$_{1g}$ mode is also seen in the H_2 exposed sample, although with a lower intensity, together with four additional peaks centred at 95.1 cm^{-1}, 158.2 cm^{-1}, 185.1 cm^{-1}, and 224.1 cm^{-1}. These are assigned to the A_g, B_{3g}, A_g, and A_g modes of SnS, respectively. They are in agreement with the modes expected for SnS layers for which the Raman peak positions are thickness dependant (Xia et al. (2016); Li et al. (2017a)). The linewidth of the SnS_2 A_{1g} peak is unchanged by the exposure and the linewidths of the SnS components are in-line with those reported in the literature (Xia et al. (2016); Li et al. (2017a)).

For the H-ion exposed sample, all the Raman peaks seen in the H_2 exposed sample are present. However, they are significantly weaker and shifted. In particular, the Raman peaks from SnS are centred at slightly different positions (96.2 cm^{-1}, 161.6 cm^{-1}, 189.1 cm^{-1}, and 221.1 cm^{-1}), in-line with measurements of bulk SnS (Xia et al. (2016); Li et al. (2017a)). Also, an additional Raman feature is observed at 127.5 cm^{-1}, which is assigned to the Γ_5 mode of β-Sn (y Blancá et al. (1993)). Additionally, the possibility of forming either α-Sn or stanene was considered, but none of the associated Raman peaks could be resolved.

Figure (4.5b) shows the evolution of the Raman signal for a single SnS_2 film upon repeated exposures to H_2. Here, the Raman spectra are normalized to the A_{1g} peak of SnS_2, revealing that with increasing exposure time, the Raman signal due to SnS becomes stronger relative to that of SnS_2. The positions of the SnS peaks also shift with each exposure in-line with an increase of the SnS layer thickness (Xia et al. (2016); Li et al. (2017a)). Similar Raman experiments on the pristine and control samples confirm that none of the SnS related peaks are present before H_2 exposure.

The Raman spectra shown in Figure (4.5) reveal that the H_2 exposed samples consist of SnS$_2$ and SnS. What they do not reveal is anything about the distribution of these materials either in the plane or normal to it. To assess the distribution normal to the plane and provide some information about the in-plane distribution over sub-100 nm distances, cross-sectional TEM was used.

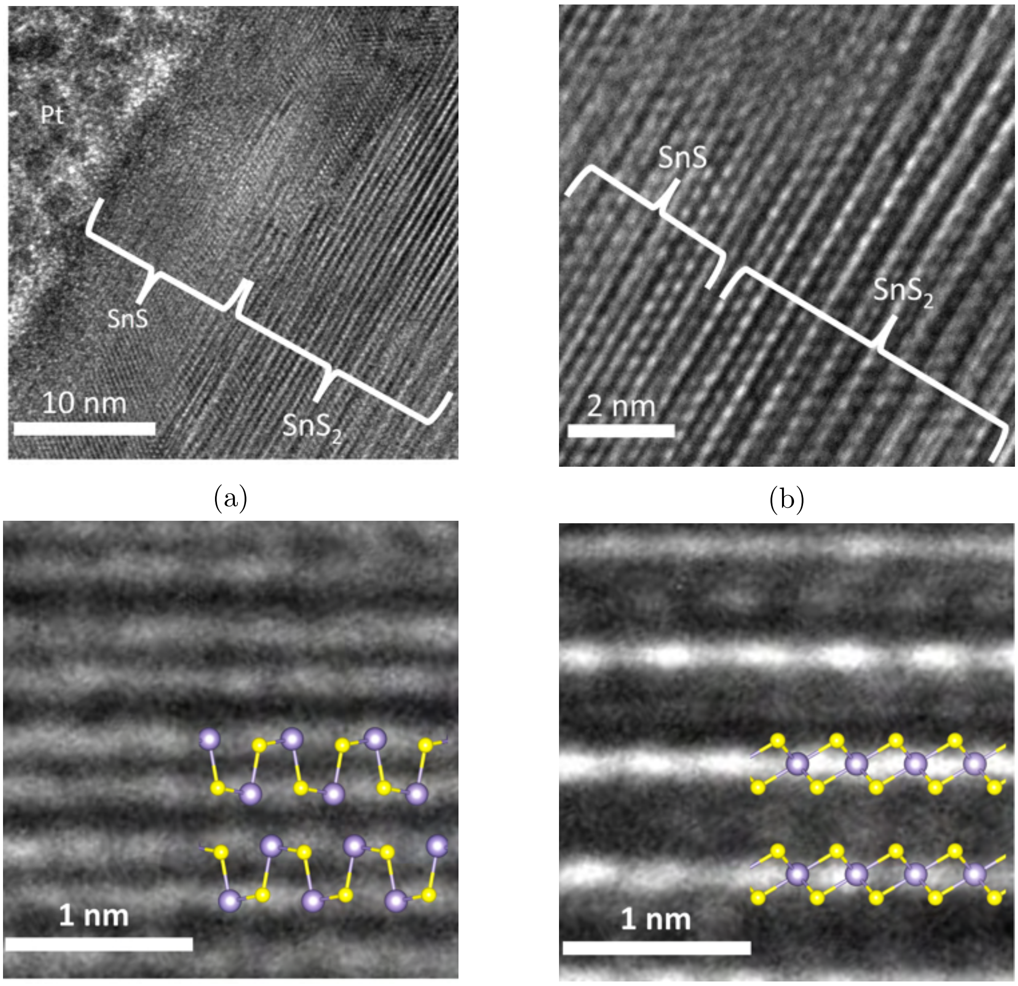

(a) (b) (c) (d)

Figure 4.6: (a) Cross-sectional high angle angular dark-field Scanning TEM image of a H$_2$ exposed sample (5×10^{-4} mbar, 150 °C, 7 hours). (b) Cross-sectional TEM images of a H$_2$ exposed sample showing the SnS-SnS$_2$ interface. (c) Overlay of the expected SnS lattice with TEM data. (d) Overlay of the expected SnS$_2$ lattice with TEM data.

Samples of H$_2$ exposed SnS$_2$ prepared on gold were reinforced using e-beam and ion-assisted deposition of platinum. Using an ion-mill, a cross-section of suitable thickness for TEM was extracted. Shown in Figure (4.6) are a selection of images from the cross-sectional TEM of this sample. Figure (4.6a) reveals the formation of an SnS$_2$/SnS heterostructure with a well defined interface between the SnS and SnS$_2$ layers and a SnS layer with a thickness of approximately 10 nm. Figure (4.6b) shows a more detailed view of the interface region: the individual vdW layers can be clearly identified and it is notable that they are continuous. Increasing the magnification further, the characteristic paired-up rows of Sn atoms are visible in the SnS region of Figure (4.6c) in line with the offset Sn atoms in individual vdW layers of SnS unit cell. In contrast, unpaired rows of Sn atoms are visible in the SnS$_2$ region of Figure (4.6d). In this case, the Sn atoms of an SnS$_2$ vdW layer all lie in the same plane. The cross-sectional TEM image in Figure (4.6d) shows the SnS$_2$ region in sufficient detail to resolve the inter-layer vdW gap. An overlay shows the expected crystallographic lattice (Madelung et al. (1998)). Similarly, the SnS interlayer vdW spacing can be seen in Figure (4.6c) overlaid with the corresponding lattice (Chattopadhyay et al. (1986)). For SnS$_2$, the lattice parameter along the c-axis is estimated at 5.9±0.5 Å. This is determined over six unit cells on the TEM image and is close to that (5.90 Å) reported in the literature (Madelung et al. (1998)). Similarly, for SnS a lattice parameter of 11.5±0.5 Å is estimated, close to that (11.2 Å) reported in previous studies of SnS (Chattopadhyay et al. (1986)). The c lattice parameter is larger than for SnS$_2$ as the unit cell of SnS consists of two vdW layers.

4.5 Optical Characteristics of SnS/SnS$_2$ Heterostructure

Information about the SnS/SnS$_2$ heterostructure over longer ranges ($\sim$ 10s μm) can be garnered via Raman mapping techniques. As shown previously in Figure (4.5), the SnS/SnS$_2$ heterosrtucture exhibits active Raman modes associated with both SnS (A$_\mathrm{g}$, B$_\mathrm{3g}$, A$_\mathrm{g}$, and A$_\mathrm{g}$) and SnS$_2$ (A$_\mathrm{1g}$). The ratio can then be taken of the area of the SnS associated peaks to the SnS$_2$ associated peaks and mapped across the surface of a flake. Over regions of constant SnS$_2$ thickness this ratio then gives a measure of the SnS layer uniformity.

Figure (4.7a) is an optical image of the region used for the Raman mapping measurements. The region is seen to cross a discontinuity in the flake associated with differing SnS$_2$ thickness present before the exposure to H$_2$. When looking at point spectra, the Raman response is markedly different when utilising the differing excitation wavelengths of λ = 532 nm and λ = 632.8 nm. This is shown in Figure (4.7b), where at location γ the SnS signal is present under excitation for λ = 632.8 nm but not for λ = 532 nm. The reverse is true for spectra gathered at location δ, with strong SnS Raman features observed with λ = 532 nm and a suppression for λ = 632.8 nm.

Raman mapping of the ratio r of the Raman signal intensity (I) due to SnS and SnS$_2$, i.e. $r = I(\mathrm{SnS})/I(\mathrm{SnS_2})$, allows the relation between the optical colour contrast and the Raman signal to be observed. Figures (4.7c) and (4.7d) show the Raman ratio maps of the area highlighted in Figure (4.7a) with λ = 532 nm and λ = 632.8 nm, respectively.

It can be seen that the value of r is dependent on both the flake colour and

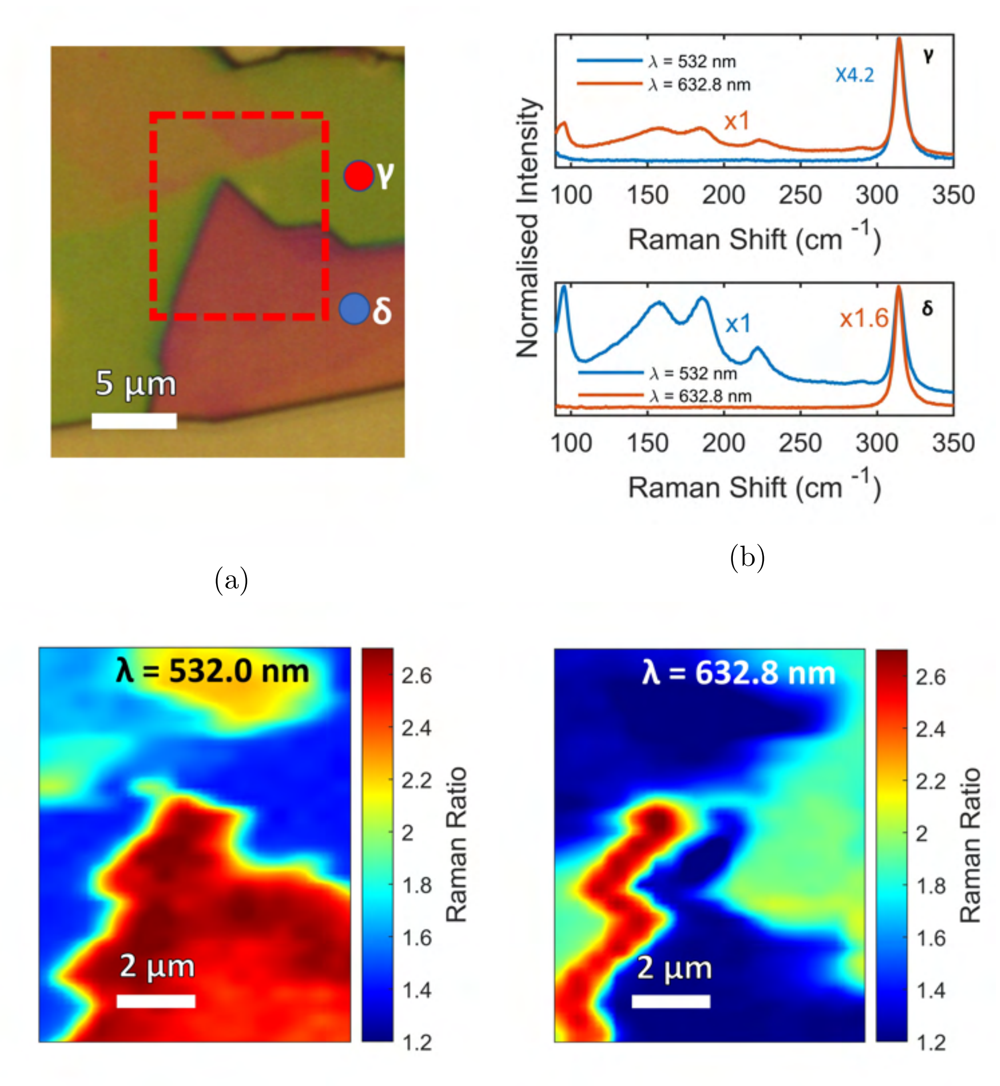

(a) (b)

(c) (d)

Figure 4.7: (a) Optical image of the areas investigated in the Raman maps as marked in red. Specific referenced locations of the flake are marked as γ and δ. (b) Raman spectra conducted on spots γ and δ in part (a). (c-d) Raman maps of the ratio of SnS to SnS$_2$ Raman signal for (c) $\lambda = 532.0$ nm and (d) $\lambda = 632.8$ nm.

the excitation wavelength λ. The colour and contrast in the optical image are determined by the interference of light reflected and transmitted at the different interfaces of the air/flake/substrate system. Thus, the colour changes as the thickness of the layers varies in the layer plane. For example, it is red (position δ, Figure (4.7a)) and green (position γ, Figure (4.7a)), corresponding to layer thicknesses of 125 nm and 175 nm, respectively, as measured by AFM, shown in Figure (4.8b). As shown in the Raman map of Figure (4.7c) for $\lambda = 532.0$ nm, the thicker regions of the flake (position γ) have a stronger contribution from SnS$_2$ than thinner regions (position δ). The reverse is observed for $\lambda = 632.8$ nm (Figure (4.7d)). This dependence and its correlation with the colour of the flake in the optical image (Figure (4.7a)) can be accounted for by a light interference effect in which constructive (destructive) interference of light leads to a corresponding enhanced (reduced) light absorption by the SnS$_2$ layer and hence larger (smaller) Raman signal.

The Raman interference effect comes about due to the nature of Raman measurements where $\lambda_{\text{excitation}} \sim \lambda_{\text{measured}}$. Given that the Raman mapping is conducted in the vertical orientation then the condition for the destructive and constructive interference of a thin film is then given by:

$$d = \frac{i}{2}\frac{\lambda}{2n}, \tag{4.2}$$

where d is the layer thickness, i is a factor determining the interference, λ is the laser wavelength and n is the refractive index. When i is even the interference is constructive and when it is odd the interference is destructive as there is no phase change at the interface between SnS$_2$ and Au due to their refractive indices (2.8 for SnS$_2$ and 0.2 for Au, (Ermolaev et al. (2021); Derkachova et al. (2016))). Similarly there is no phase change between the SnS$_2$ and SnS interface as the refractive index of SnS is ~4 (Diachenko et al. (2019)). As such, the regions where the conditions for constructive and destructive interference are met can be mapped onto an AFM height profile and represented as fractions of λ. This has been done for for $\lambda = 532$ nm and $\lambda = 632.8$ nm in Figures (4.8c) and (4.8d), respectively. Here the contribution from SnS has been ignored and the SnS layer thickness (10 nm) has been subtracted from the measured AFM height profiles.It is What can be seen from the interference maps at both excitation wavelengths is how well the interference conditions map onto both the optical colour contrast and the Raman ratio r maps of the flake. In both instances, it can be seen that only when the destructive condition is met in the SnS$_2$ layer can the SnS Raman signal be seen.

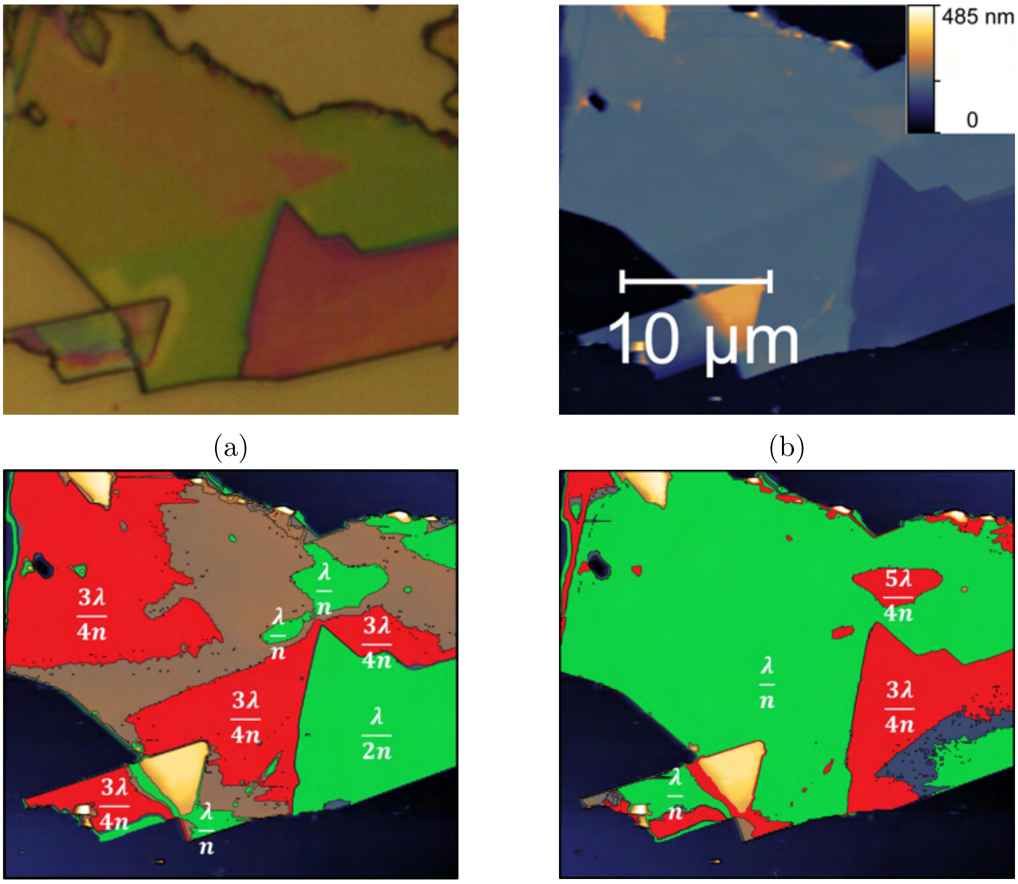

(a) (b)

(c) (d)

Figure 4.8: (a) Optical image of an SnS$_2$ fake exposed to H$_2$ (7×10^{-4} mbar, 150 °C, 7.5 hours). b) AFM height map of the flake in (a). (c) AFM map as in (b) indicating regions in which the constructive (green) and destructive (red) optical interference conditions are met for $\lambda = 632.8$ nm. (d) AFM map in (b) indicating regions in which the constructive (green) and destructive (red) conditions are met for $\lambda = 532.0$ nm. Here, n=2.8 is the refractive index of SnS$_2$.

Given that Raman disparities between regions of different thickness can be explained via an interference effect, then the variation within regions of constant thickness is used to estimate the uniformity of the SnS layer over the scale of microns. On the red and green regions of the flake in the optical image, the variation in the Raman ratio (r) is found to be less than 8% and 14%, respectively.

AFM also provides a means by which the surface quality of the heterostrcutre can be assessed. Surface studies of the heterostructures by AFM show that the surface SnS layer retains a similar rms roughness to the control sample at low doses (5×10^{-4} mbar, 3.5 hours, 150 °C). With increasing hydrogen dose and/or exposure (greater than 7 hours), the roughness tends to increase. Thus, under controlled hydrogen exposure conditions, it is possible to realize SnS$_2$/SnS heterostructures with high-quality surfaces.

An assessment of heterostructure quality beyond the structural proprieties described by TEM and Raman can be made via PL spectroscopy. This experimental probe is relevant to the potential opto-electronic applications of such a heterostructure. Both bulk SnS$_2$ and SnS crystals have an indirect band gap and their in-plane lattice constants, interlayer distances and interlayer binding energies tend to be weakly dependent on the layer thickness. SnS$_2$ has an indirect band gap energy of 2.25 eV and a direct band-gap energy of 2.38 eV (Burton et al. (2016); Yang et al. (2021)), whilst SnS has an indirect band gap energy of 1.07 eV and a direct band gap energy of approximately 1.4 eV (Vidal et al. (2012)). With these considerations, and with reference to the absorption spectrum of SnS$_2$ (Yang et al. (2021)), we now consider the optical properties of the flakes by examining their band edge recombination (Figure (4.9b)) under different excitation wavelengths. Figures (4.9c) and (4.9d) show the PL maps for the flake in Figure (4.7a). The corresponding PL spectra are displayed in Figure (4.9a) and are characterized by two bands centred at around 1.7 eV and 1.4 eV, whose relative weight changes with the excitation wavelength. The PL band centred at 1.7 eV is red-shifted relative to the absorption edge of SnS$_2$, suggesting a

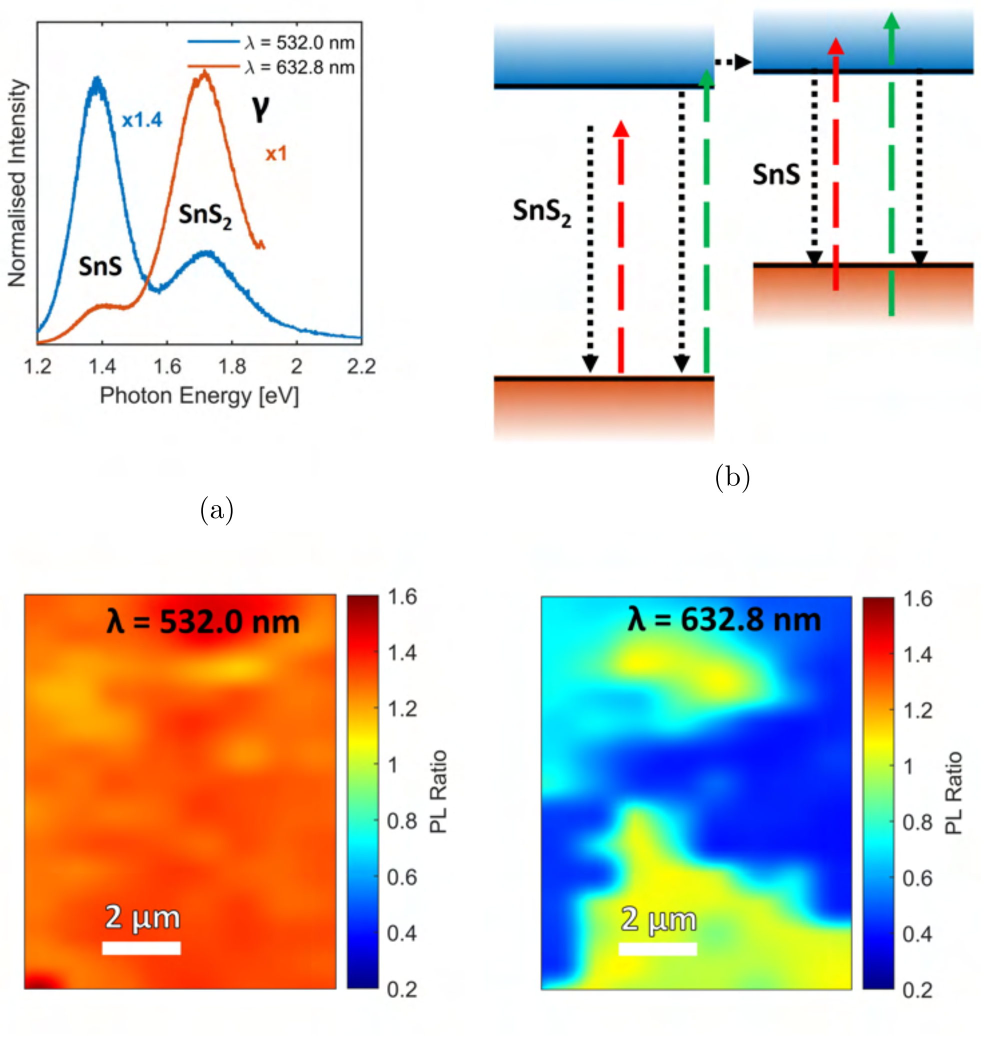

(a)

(b)

(c)

(d)

Figure 4.9: (a) PL spectra conducted on spot γ in Figure (4.7a). (b) Type II band alignments of SnS_2 and SnS and optical transitions under laser excitation at 532.0 nm (green 2.33 eV) and 632.8 nm (red 1.96 eV). Dotted and continuous lines sketch relaxation and radiative recombination, respectively. The band alignment as determined experimentally in the literature (Sugiyama et al. (2014)). (c-d) PL maps of the ratio of SnS to SnS_2 PL signal with $\lambda = 532$ nm (c) and $\lambda = 632.8$ nm (d).

dominant recombination of carriers from localized states, consistent with SnS_2 with a slightly reduced S content (Kudrynskyi et al. (2020)). The PL band centred at 1.4 eV was previously reported in SnS and SnS-inclusions in SnS_2 (Kudrynskyi et al. (2020); Sutter et al. (2017)). There was also an absence of the expected sizable optical anisotropy of the PL emission of

SnS, as measured from polarisation resolved PL (Chen et al. (2018a); Lin et al. (2018)), suggesting that the PL emission at 1.4 eV in the structures arises from the recombination of carriers from localized states (Kudrynskyi et al. (2020)). Thus, this PL band may not share the same optical characteristics of the band edge recombination.

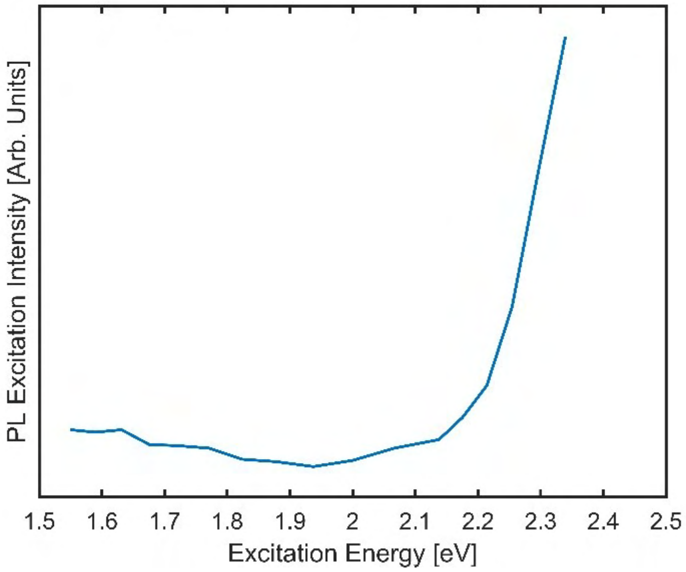

Figure 4.10: Photoluminescence excitation (PLE) spectrum for a SnS/SnS$_2$ heterostructure. The experiment is conducted at room temperature with a detection energy of $h\nu = 1.4$ eV, corresponding to the low-energy PL peak of the PL spectrum shown in Figure (4.9a).

The ratio of the integrated PL intensities, $r = I(1.4 \text{ eV})/I(1.7 \text{ eV})$, is approximately 1.2 and is uniform in the layer plane for $\lambda = 532$ nm (Figure (4.9c)). Thus, the emission from SnS tends to dominate the PL emission and is uniform, suggesting that the hydrogenation leads to a homogeneous conversion of the SnS$_2$ surface onto SnS. Furthermore, this indicates a preferential relaxation of photogenerated carriers from SnS$_2$ onto SnS. Increasing λ from 532.0 nm to 632.8 nm results in a stronger recombination signal from the defect dominated 1.7 eV band relative to the 1.4 eV band (Figure (4.9a)). The PL spectra under different excitation wavelengths can be understood in terms of different relaxation pathways for carriers and by referring to the schematic of Figure (4.9b). Since the SnS/SnS_2 heterostructure has a type II band alignment with a band offset of 0.10 eV in the conduction band (Sugiyama et al. (2014)), under resonant excitation ($\lambda = 632.8$ nm) of the SnS_2 layer, electrons photogenerated in SnS_2 cannot relax onto SnS, leading to a larger signal from SnS_2 relative to SnS and corresponding decrease of r (Figure (4.9d)). This result is supported by PL excitation (PLE) measurements over an extended energy range (Figure (4.10)) showing that the PL emission centred at 1.4 eV (attributed to SnS) tends to increase for excitation energies approaching the absorption band edge of SnS_2. Finally, the PL spectra show no evidence of an interlayer excitonic recombination. However, this is not unexpected due to the relatively thick SnS and SnS_2 layers. It should be noted that in the literature there is a large range of conduction band alignments from 0.1 eV to 0.5 eV (Sugiyama et al. (2014); Whittles et al. (2016)). These results are consistent with the low end of that range and speak to large differences in the band positioning of SnS as a result of crystal quality, composition and defects (Wang et al. (2017)).

4.6 Computational Results

Density functional theory calculations were performed to examine the reaction energetics for the conversion of SnS_2 to SnS via H_2. The results are summarised in Table (4.1). It was found the direct conversion of SnS_2 to SnS without H_2 (Reaction 1) is endothermic, i.e. the reaction is not energetically favourable. However, in the presence of H_2, the conversion (Reaction 2) becomes exothermic and energetically favourable, with the formation of H_2S as a by-product. Further conversion of SnS to β-Sn, either with (Reaction 6) or without H_2 (Reaction 5), is endothermic. Sim-

Table 4.1: DFT predicted reaction energies (ΔE, in kJ mol^{-1}) of selected reactions. Positive ΔE indicates the reaction is endothermic, and negative ΔE indicates the reaction is exothermic. The symbol in the brackets denotes the phase of the reactants/products, "s" for solid and "g" for gas.

Index	Reaction	ΔE [kJ mol^{-1}]
1	$SnS_2(s) \rightarrow SnS(s) + S(s)$	+8.6
2	$SnS_2(s) + H_2(g) \rightarrow SnS(s) + H_2S(g)$	-34.1
3	$SnS_2(s) \rightarrow Sn(s) + 2S(s)$	+114.5
4	$SnS_2(s) + 2H_2(g) \rightarrow Sn(s) + 2H_2S(g)$	+28.9
5	$SnS(s) \rightarrow Sn(s) + S(s)$	+105.8
6	$SnS(s) + H_2(g) \rightarrow Sn(s) + H_2S(g)$	+63.0

ilarly, the conversion of SnS_2 to β-Sn, either with (Reaction 4) or without H_2 (Reaction 3), is also endothermic. It's notable that the presence of H_2 makes the conversion of SnS_2 or SnS to β-Sn (Reactions 4 and 6) less endothermic, by 85.6 and 42.8 KJ mol^{-1}, respectively. Thus, the DFT calculated reaction energies explain well the experimental observation on why H_2 treatment promotes the conversion of SnS_2 to SnS, but further conversion to β-Sn requires higher temperatures or longer exposure times. Conversion to β-Sn by H-ions is facilitated by the increased reactivity of the charged species and the additional 12 eV kinetic energy of the ions above the energies available to H_2.

4.7 Carrier Effective Mass in SnS_2

Detailed studies of the electronic properties of SnS_2 were conducted in collaboration with Dr. Zhuo Yang (Institute for Solid State Physics at the University of Tokyo). He performed optical transmission measurements of SnS_2 samples at high magnetic fields (150 T). These results were reported in Yang et al. (2021). By extracting the electronic band gap energy from these spectra and recording its dependence on the strength of the magnetic field, we were able to deduce important information, including the reduced cyclotron exciton mass for comparison to calculated values. The magnetic field (B) dependence of the indirect band gap energy is given by

$$E(B) = E_g \pm \hbar\omega_0 + (N + \frac{1}{2})\hbar\omega_c^h + (N' + \frac{1}{2})\hbar\omega_c^e, \tag{4.3}$$

where $E(B)$ is the band gap energy, E_g is the band gap energy with no magnetic field, $\hbar\omega_0$ is the phonon energy, N and N' are the hole and electron Landau level quantum numbers, respectively, and $\hbar\omega_c^h$ and $\hbar\omega_c^e$ are the cyclotron energies of the holes and electrons respectively (Halpern and Lax (1965); Roth et al. (1959)). The magnetic field dependence of the cyclotron energies as given by

$$\omega_c^{e/h} = \frac{eB}{m^*_{e/h}}, \tag{4.4}$$

where $m^*_{e/h}$ is the cyclotron mass of electrons/holes. The masses can be combined into a reduced electron-hole cyclotron mass (μ^*) given by

$$\mu^* = \frac{m^*_h m^*_e}{m^*_h + m^*_e}. \tag{4.5}$$

As N and N' were found to be 0 and $\hbar\omega_0$ is assumed to be independent of B, this allows a rewriting of Equation (4.3) as

$$\Delta E = \frac{\hbar e B}{2\mu^*}, \tag{4.6}$$

where ΔE is the magnetically induced change in the band gap energy.

To accurately determine the measured band gap in the transmission spectra, a precise fit must be made. This is done via the following equation

$$\alpha = A\frac{(\hbar\omega - E_g - \hbar\omega_0)^2}{1 - e^{-\hbar\omega_0/k_BT}}, \tag{4.7}$$

where α is the adsorption coefficient, A is a constant pre-factor, $\hbar\omega$ is the photon energy, k_B is the Boltzmann constant and T is the temperature (Lipson et al. (2010)). The adsorption coefficient is then related to the transmission function (T) via an exponential ($T = e^{-\alpha t}$, where t is the sample thickness).

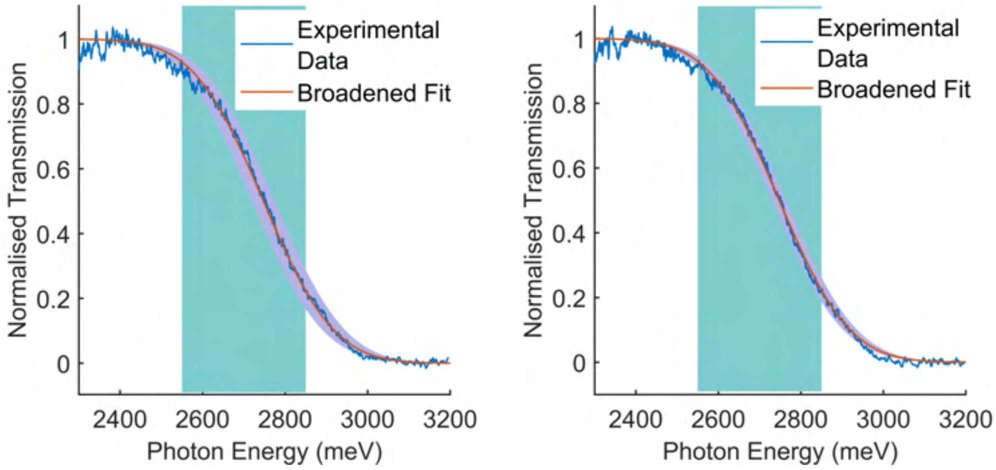

(a) (b)

Figure 4.11: Fitting to optical transmission spectra of $\mathrm{SnS_2}$ at 5 K with (a) $B = 0$ T and (b) $B = 150$ T. The teal region defines the portion of curve used to assess the error in E_g. The purple region defines the 2σ uncertainty in E_g.

This expression was utilised to perform a fit to the experimental data shown in Figure (4.11) with a Gaussian broadening applied. A large Gaussian broadening was required to achieve a good fit at the tails of the spectra. The values used are $\sigma = 138$ meV and 133 meV in Figures (4.11a) and (4.11b), respectively. This is much higher than k_BT, which is 0.43 meV at 5 K, indicating some other non-thermal component contributes to the broadening.

The values of E_g determined from the best fits are 2690 meV and 2688 meV at 0 T and 150 T at 5 K, respectively. The error was estimated from the distribution of experimental data about the line of best fit with the 2σ bound shown in purple in Figure (4.11). The 2σ error on both fits is then 23.9 meV and 17.0 meV at 0 T and 150 T, respectively, in-line with the experimental spectral linewidth. It is not possible in the case of SnS_2 to resolve any band gap shift at 150 T. As no shift in the band gap energy was observed, an inspection of Equation (4.6) reveals that a lower limit can be determined for the reduced electron-hole cyclotron mass. With $\Delta E \leq$ 17.0 meV, this was determined as $\mu^* \geq 0.511$ m$_e$.

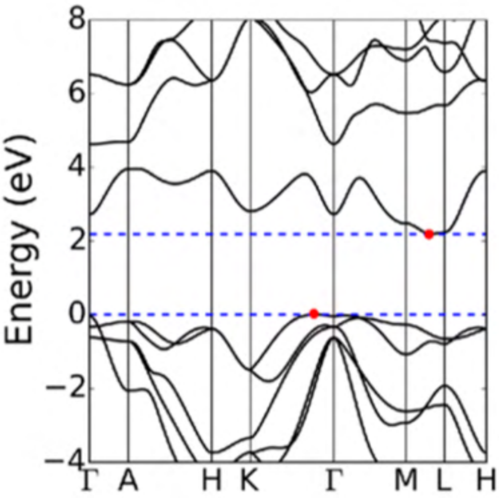

Figure 4.12: Band Structure of bulk SnS_2 computed via DFT and reported in Yang et al. (2021). The red dots and dashed blue lines denote the positions and energies of the valence band maximum and conduction band minimum.

This value of μ^* is greater than that predicted via DFT calculations which put the value of μ^* between 0.307 m$_e$ and 0.378 m$_e$ (Gonzalez and Oleynik (2016); Shafique et al. (2017); Yang et al. (2021)). The large value of μ^* is driven by the hole effective mass in SnS_2, which is predicted as being between 0.92 m$_e$ and 1.169 m$_e$, as compared to the electron effective mass which has a predicted range of between 0.46 m$_e$ and 0.559 m$_e$ (Shafique et al. (2017); Yang et al. (2021)). The large hole effective mass is determined by the relatively flat band dispersion in SnS_2 near the valence band maximum. This is shown if Figure (4.12) where the relatively flat dispersion extends along the X-K and X-Γ directions, where X is the position of the valence band maximum. Along X-K and X-Γ the hole effective masses are 2.583 m_e and 3.196 m_e (Yang et al. (2021)).

4.8 Summary

The results of the Raman, TEM, and XPS studies demonstrate the conversion of SnS_2 to SnS through exposure to H_2. Furthermore, cross-sectional TEM images reveal how this conversion produces a heterostructure with a sharp transition from SnS_2 to SnS, indicative of a box-like diffusion. Importantly, as with the exfoliation and stamping method frequently used in lab-scale manufacture of vdW heterstuctures, the *c*-axes of both SnS_2 and SnS are co-axial and reveal continuous unbroken layers.

The uniformity of the heterostructure and its interface, as revealed by TEM, is further confirmed by Raman mapping. These show Raman signals from the heterostructure that are uniform over extended (micron sized) regions. Also, the Raman measurements demonstrate the possibility for controlling the formation and properties of the heterostructure via exposure time or repeated exposures, resulting in an increasing Raman intensity ratio $I(\mathrm{SnS})/I(\mathrm{SnS_2})$ and shift of the Raman modes due to SnS. However, the XPS reveals that the SnS loading may vary significantly between flakes.

The further conversion of SnS to β-Sn was also considered using a H-ion beam and confirmed by XPS, EDX, and Raman data. The formation of extended plateau features observed in the optical and SEM images is explained by the increased density of Sn in β-Sn (35.3 atoms nm^{-3}) than in SnS (19.6 atoms nm^{-3}) and SnS_2 (14.7 atoms nm^{-3}), resulting in a contraction of the crystal as SnS is converted to β-Sn. This behaviour is in-line with previous reports of etching of SnS by hydrogen plasma (Xiao et al. (2018)). A similar etching behaviour is observed in samples exposed to H_2 at temperatures greater than 250 °C.

The chemical conversion of SnS_2 to SnS could be facilitated by the presence of S-vacancies, a common defect in SnS_2 (Gong et al. (2018)), with a stronger binding energy to H_2, i.e. the reaction may initiate from S-vacancies present on the SnS_2 surface, propagate within the layer, followed by continued reaction into other layers. It is notable that these defects can be induced, for example via an electron beam, and that these defects introduce deep states within the band-gap (Sutter et al. (2017); Kumagai et al. (2016)). For SnS_2 exposed to H-ions, the conversion to β-Sn is ascribed to the higher reactivity of H-ions. Note that H_2 has a dissociation energy of 432 kJ mol^{-1} (Herzberg and Monfils (1961)), and this may render reactions 4 and 6 in Table (4.1) exothermic if H_2 is replaced by protons as reactants.

That the conversion of SnS_2 to SnS via H_2 should produce such a highly ordered heterostructure is a surprising result. It has clear application in any field where a SnS/SnS_2 heterostructure might be applied, including heterojunction diodes (Kim et al. (2018)), NO_2 detectors (Sun et al. (2019)), and other opto-electronic devices (Li et al. (2018)).

Additionally, a study conducted to determine the reduced electron-hole cyclotron mass in SnS_2 yielded a lower bound of $\mu^* \geq 0.511\ m_e$. This is a relatively large value when compared to theory and to other materials such as GaSe, where the value is 0.13 m_e and 0.15 m_e parallel and perpendicular to the c-axis, respectively (Watanabe et al. (2003)). This is relevant to the design of functional devices containing SnS_2.

Chapter 5

Hydrogen - Indium Selenide Interaction

This chapter describes a number of experimental and theoretical studies of the interactions between the vdW crystal γ-InSe and both molecular and atomic hydrogen. The results of which were reported in Felton et al. (2020) authored by myself with experimental input from myself and Elena Blundo (University of Rome), a PhD student of Prof. Antonio Polimeni (University of Rome), and theoretical input from Dr. Sanliang Ling (University of Nottingham) and Joseph Glover (University of Nottingham).

Contents

5.1 Proposed Sites of Hydrogen Incorporation

The motivations for studying the interaction of γ-InSe with hydrogen are threefold. Firstly, the desire to understand the ability for hydrogen to be incorporated within the vdW layers of γ-InSe from both molecular and ionic sources. This has relevance to the applications of hydrogen storage, sensing and purification. Secondly, the ability for hydrogen to modify the structural and optical properties of the crystal. The applications of which lie in the desire to find ways to tune the properties of vdW materials. Third, to understand the comparisons to other vdW materials where different modalities of interaction have been observed but remain unexplained. For example, the reasons why some vdW materials such as MoS_2 form H_2 filled bubbles when exposed to a H-ion beam whilst others don't remains unknown (Tedeschi et al. (2019)). Intuition might suggest that the layer flexibility is important in this respect. Since γ-InSe has a relatively small Young's modulus (Zhao et al. (2019)), it provides a good check for this intuition.

For samples of γ-InSe exposed to hydrogen, we propose five different sites for hydrogen incorporation, four of which are shown in Figure (5.1). In the first (Figure (5.1a)), the presence of H_2 molecules is sufficiently unfavourable in the crystal that any introduced via an ion beam or any incorporated from the gas phase under high pressure and/or temperature are expelled from the crystal when returned to ambient conditions. In this scenario, unmodified γ-InSe remains. In the second, shown in Figure (5.1b), the presence of H_2 molecules within the crystal are sufficiently favourable that when introduced via ion-beam or from the gas phase, they remain in the crystal under ambient conditions. This forms a monolayer in the vdW

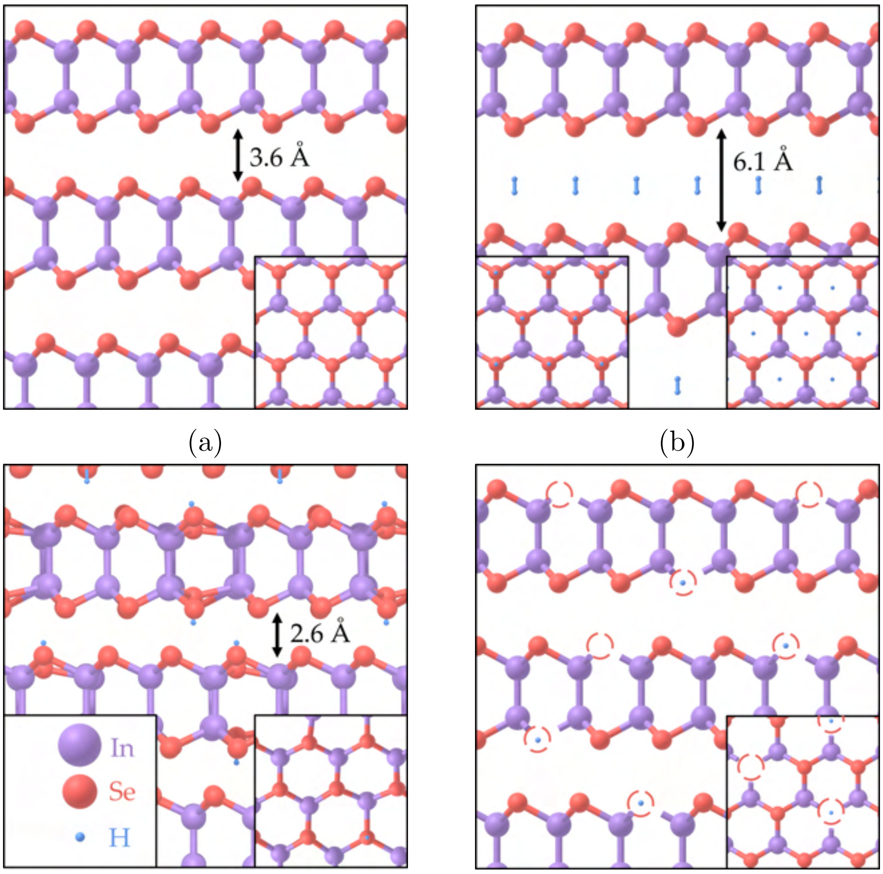

(a) (b) (c) (d)

Figure 5.1: Crystallographic structures for: (a) Pristine bulk γ-InSe viewed in plane and (inset) out of plane. (b) Bulk γ-InSe containing H_2, as computed using DFT, viewed in plane and (inset) out of plane. (c) Bulk γ-InSe with atomic hydrogen bonded to Se, as computed using DFT, viewed in plane (inset) out of plane. (d) Proposed structure of bulk γ-InSe with Se vacancies, some of which contain atomic hydrogen, as viewed in plane and (inset) out of plane.

gap which could ultimately lead to the formation of bent layers or domes, as seen in other layered crystals (Tedeschi et al. (2019)). In the third, shown in Figure (5.1c), the reactivity of a H-ion beam and/or gas phase H_2 is sufficiently great to react with the crystal. Shown in Figure (5.1c) is the case where H atoms bond to Se atoms within the crystal but other reaction schemes can also be envisaged. For example, a reaction wherein the crystal is reduced by hydrogen to form $InSe_x$ where x <1 and H_2Se is released. This is analogous to the reaction scheme considered in chapter 4. In the fourth scenario, shown in Figure (5.1d), Se vacancies present in

γ-InSe are occupied by atomic hydrogen. In the fifth case, Se vacancies present in γ-InSe are occupied by molecular H_2.

In the interest of understanding these different possibilities the interaction between hydrogen and γ-InSe has been studied both experimentally and theoretically. This was done through a combination of PL, Raman spectroscopy, XPS, gas-uptake measurements, DFT simulations (including phonon mode calculations), and grand canonical Monte Carlo (GCMC) simulations. The interaction with H-ions is discussed first, followed by a discussion on the interaction with H_2.

5.2 Interaction with Hydrogen-Ions

In order to characterise the interaction between H-ions and γ-InSe, samples of the vdW crystal were mechanically exfoliated and dry-stamped onto $Au/SiO_2/Si$ substrates. These samples of bulk γ-InSe were then exposed to atomic hydrogen using a Kaufman ion source, which produces a mono-energetic beam of H-ions. When these ions implant themselves in the grounded sample, they acquire an electron and become neutralised. A full description of the Kaufman ion source can be found in section 3.2.2. After neutralisation the behaviour of the hydrogen species is dependant on the nature of the hydrogen interaction with the material in question. All results were obtained from samples exposed to low beam energies of either 10 eV or 32 eV at temperatures of $T = 25$ °C and 80 °C and with total ion doses of $1{\times}10^{15}$ ions cm^{-2} and $6{\times}10^{16}$ ions cm^{-2}, respectively. These samples were compared with pristine γ-InSe or samples covered by a H-opaque mask during the hydrogenation.

5.2.1 Electron Spectroscopy Studies

Important to assessing the interaction of H-ions with γ-InSe is the possibility that the crystal may be chemically modified by the exposure. In particular, the propensity of InSe for forming Se vacancies must be considered. In the instance that Se vacancies are formed in the samples, it would be expected that they would be rapidly oxidised upon exposure to air (Balakrishnan et al. (2017)). If generated in sufficient concentrations this oxidation would be visible to techniques sensitive to the chemical state of the atoms in the sample. Such as XPS.

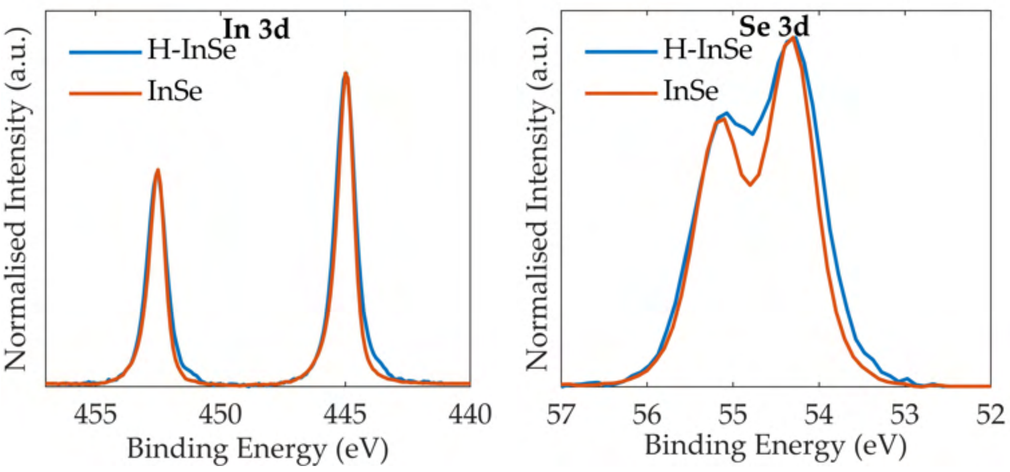

(a) (b)

Figure 5.2: Charge corrected and normalised XPS spectra for pristine and hydrogenated (32 eV) γ-InSe. Shown are the regions corresponding to: (a) The In 3d doublet and (b) the Se 3d doublet.

Demonstrated in Figures (5.2a) and (5.2b) are the In 3d and Se 3d peaks of the masked and H^+ (32 eV) exposed InSe samples. In the masked InSe sample, the In 3d peaks are located at 445 eV and 452.5 eV. The splitting of this doublet is 7.5 eV, in-line with the expected 7.54 eV (Wagner et al. (2003)). The most prominent components of the In 3d peaks remain unchanged by H^+ exposure in terms of position, relative peak height and magnitude of the doublet splitting. However, in the H^+ exposed sample there is a slight broadening of both peaks towards lower binding energy, accompanied by the emergence of a new small shoulder. In Figure (5.2b) a similar pattern of behaviour is observed in the Se 3d peak. In the unexposed sample the Se 3d peaks are found at 54.3 eV and 55.1 eV, with an associated splitting of 0.8 eV, in-line with expectations of 0.86 eV (Moulder et al. (1992)). As with the In 3d peaks, there is a broadening towards lower binding energy of theses peaks of approximately 0.1 eV.

The modification of both the In and Se 3d peaks is inconsistent with the changes expected from the oxidation of Se vacancies as this would induce a shift of the In 3d peaks to higher binding energy and would produce little change of the Se 3d peaks (Balakrishnan et al. (2017)). It is clear however, that the H-ion beam has induced a chemical change in the sample.

5.2.2 Raman Studies

The small interaction cross-section between X-rays and hydrogen limits the ability for XPS to probe the hydrogen incorporation in a given material. To further assess the mode of hydrogen modification, a structure sensitive technique is instead employed. To this end, a Raman spectroscopic characterisation of the unmodified and modified material has been conducted.

Raman spectroscopy, being sensitive to the phonon modes of a crystal, does not need to be hydrogen sensitive to be useful in this context. Instead, what is needed is an understanding of the phonon origin of each Raman peak and of how these peaks are modified by the presence of hydrogen in different locations. Figure (5.3a) shows the measured Raman spectra of a masked and H-ion exposed γ-InSe, and the phonon modes attributed to each of the peaks. These modes are: the $\mathrm{A}^1_{1\mathrm{g}}$ mode at 118 cm^{-1}, the $\mathrm{E}^1_{2\mathrm{g}}$

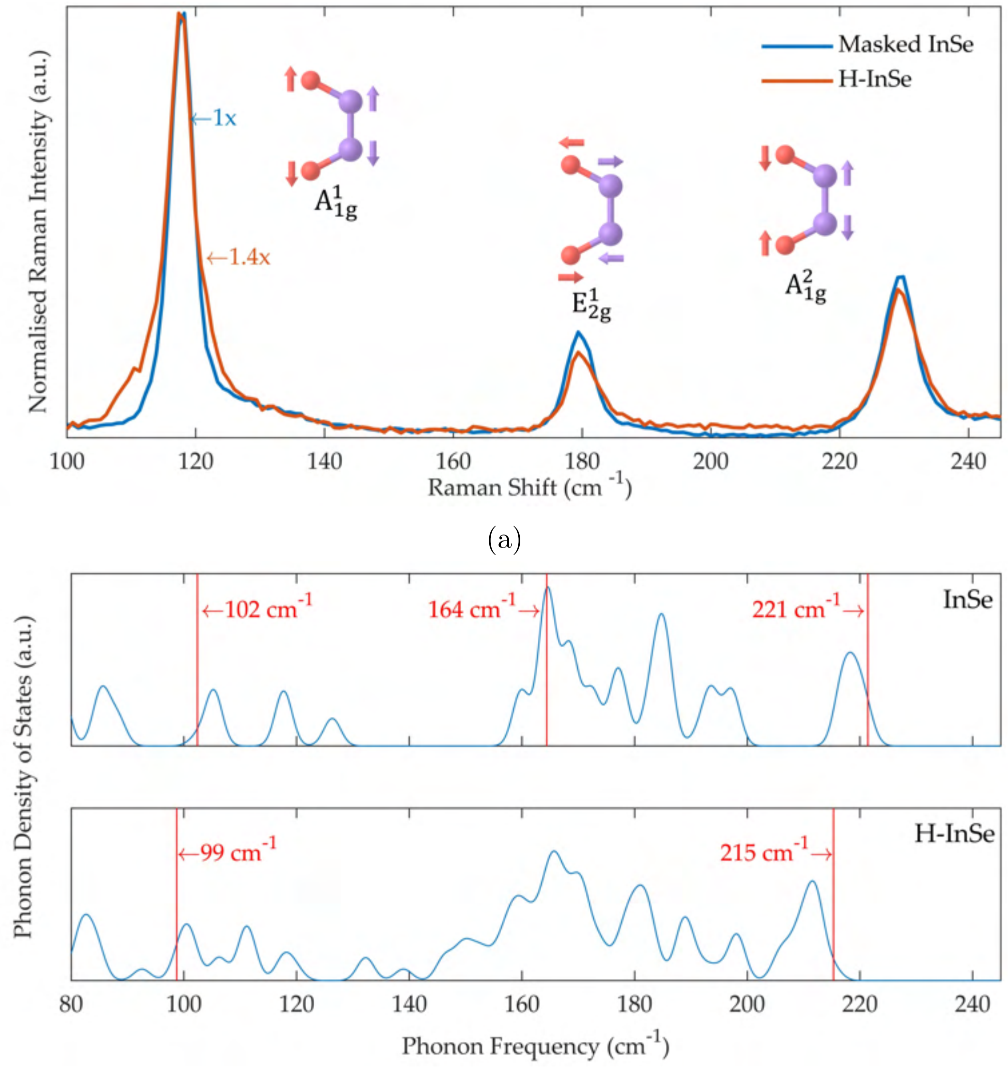

(a)

(b)

Figure 5.3: (a) Normalised Raman spectra of masked and hydrogenated (32 eV) γ-InSe, measured 12 days after hydrogenation (λ = 532 nm, P = 0.2 mW, T = 300 K). The spectra are normalised to the first Raman peak. Insets: vibrational modes responsible for the three peaks. (b) DFT-calculated phonon density of states for a pristine InSe monolayer and atomic hydrogen bonded to an InSe monolayer. These were calculated using a 4×4×1 supercell. The phonon density of states are Gaussian broadened with σ = 1.5 cm^{-1}. Vertical red lines in (b) mark the position of Raman active modes, these correspond to the peaks in (a).

mode at 180 cm^{-1}, and the A^2_{1g} mode at 230 cm^{-1} (Sánchez-Royo et al. (2014)). Upon exposure to the H-ion beam a reduction in the Raman intensity of 1.4× is seen. The positions of the three labelled Raman peaks remain unchanged by exposure of γ-InSe to the H-ion beam. However, there is a sizable modification of the low shift tail of the A^1_{1g} mode with a more prominent feature visible for the H-ion exposed sample. Fitting to the component allowed it to be located to 110.2 cm^{-1}. The size of the feature and the absence of similar features on the E^1_{2g} and A^2_{1g} modes indicates that this change is real and not associated with a change in the background signal. Also, it was noted that Raman spectra recorded in an extended range up to 4200 cm^{-1} did not yield any features consistent with the presence of H_2 (Stoicheff (1957); Leitch et al. (1998)).

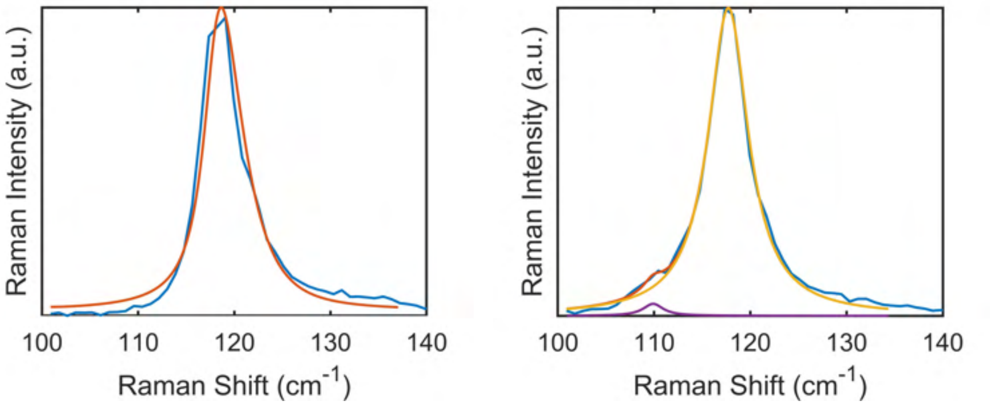

(a) (b)

Figure 5.4: Raman spectra of the A^1_{1g} peak of the InSe (a) control sample and (b) exposed to hydrogen. The peak are fit using an exponential broadened Lorentzian function.

An understanding of the structural changes of γ-InSe induced by hydrogen can be gained from computational methods. Specifically, the frequencies of the phonon modes can be computed using DFT for different sites of incorporation, such as those in Figure (5.1). Figure (5.3b) shows the simulated phonon density of states for unmodified and H-bonded monolayer InSe. Monolayer InSe was used as the active Raman modes could not be identified in the H-bonded bulk γ-InSe phonon density of states and a full Raman calculation was not performed to allow for a precise identification. Across the range shown (80 - 245 cm^{-1}) the total number of modes remains unchanged by hydrogen inclusion. However, following the incorporation of

H, the modes broaden, particularly around the E^1_{2g} mode in the 140 - 190 cm^{-1} range. The position of the labelled Raman active modes can also be seen to change. The A^1_{1g} mode shifts from 102 cm^{-1} to 99 cm^{-1} and the A^2_{1g} mode shifts from 221 cm^{-1} to 215 cm^{-1}. The shift of the A^1_{1g} mode is in qualitative agreement with the experimental outcome. This result can be intuitively understood as the modification of the Raman mode by the additional mass of hydrogen present in the crystal. Similarly, the computational prediction of the modification of the E^1_{2g} mode is consistent with the slight reduction of the intensity of the measured Raman peak relative to the A^1_{1g} mode. However, the simulation fails to replicate the experimental behaviour of the A^2_{1g} mode (Figure (5.3a)). This may be due to the limits of the simulation and the requirement to run the calculation at very high hydrogen densities. H_2 incorporation fails to explain the Raman changes shown in this sample, discussed later in this chapter and shown in Figure (5.13). The position of the A^1_{1g} mode shifts in the wrong direction for H_2 incorporated γ-InSe. Ultimately, the H-bonded configuration shown in Figure (5.1c) best explains the observed Raman and XPS behaviour. However, it should be noted that the DFT underestimates the extent of the change in the Raman.

5.2.3 Photoluminesence

The incorporation of hydrogen and/or the modification of the γ-InSe crystal resulting from the interaction with hydrogen can reasonably be expected to modify its optical properties. PL can be especially helpful in this regard due to its sensitivity to impurities and defects within a crystal. To this end room temperature and low temperature PL studies of the masked and H-ion exposed (32 eV and 10 eV) samples were conducted.

Figure (5.5a) shows the room temperature PL spectra of masked and H-ion exposed γ-InSe. The PL peak position at 1.25 eV is unaffected by the presence of hydrogen, as is the PL lineshape. The intensity of the PL emission does change with an 18× lower PL intensity recorded in the samples exposed to H-ions at 32 eV and a 10× lower PL intensity recorded in the sample exposed to H-ions at 10 eV, relative to the masked sample. The masked sample recorded no quenching of PL intensity when measured immediately before and after exposure.

A better understanding of the origin of the reduced PL intensity can be gathered through low-temperature PL. Low-temperature PL can reveal spectral features unseen at room temperature due to reduced phonon scattering of carriers and the preferential recombination of photogenerated carriers from defect states. Figures (5.5b) and (5.5c) show the PL spectra of unexposed γ-InSe and γ-InSe exposed to H-ions (10 eV) recorded at 10 K for a range of exciting laser powers (P) with $\lambda = 532$ nm. The multiple emission lines at low photon energies (<1.32 eV) are most prominent at low excitation powers and are associated with impurities and/or defects (Shubina et al. (2019); Abay et al. (1998)). No features at photon energies less than 1.32 eV can be successfully attributed to hydrogen, as the variation between the two samples is indistinguishable from the variation found within the individual samples. For photon energies above 1.32 eV, the exciton (X), biexciton (XX) and exciton-exciton scattering (X-X) PL lines can be identified (Shubina et al. (2019); Abay et al. (1998)). They dominate the PL spectra at higher excitation powers. The X-peak in pristine and hydrogenated (10 eV) InSe is at 1.340 ± 0.002 eV and 1.337 ± 0.002 eV, respectively. The position of the XX-peak in pristine and hydrogenated (10 eV) InSe is at 1.333 ± 0.002 eV and 1.334 ± 0.002 eV, respectively. The position of the X-X peak in pristine and hydrogenated (10 eV) InSe is at

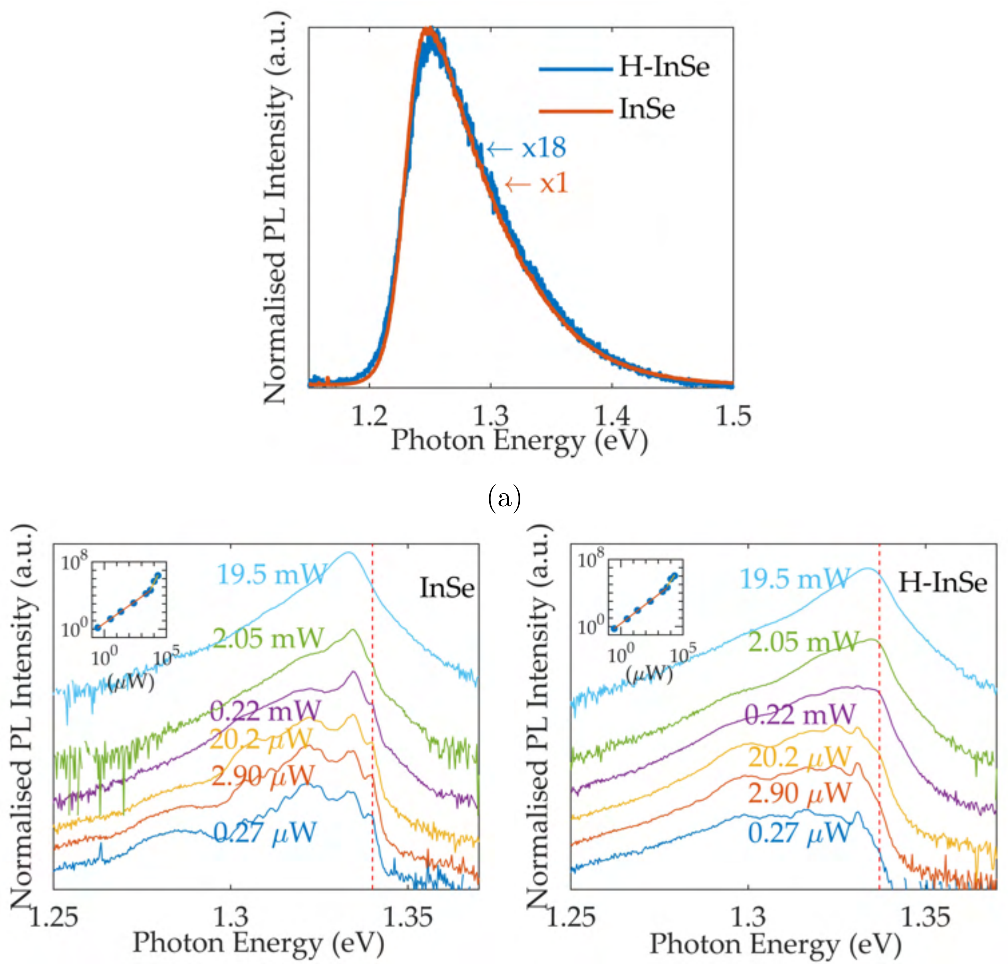

(a)

(b)

(c)

Figure 5.5: (a)Normalised PL spectra measured in masked and hydrogenated (32 eV) γ-InSe, 12 days after hydrogenation focused through a 100× objective with a spot size of $\sim$1 μm (λ = 532 nm, P = 0.2 mW, T = 300 K). (b,c) PL spectra measured at different exciting laser powers in pristine and hydrogenated (10 eV) γ-InSe (λ = 532 nm, T = 10 K). The spectra are plotted on a logarithmic scale with the dashed lines denoting the energy position of the exciton line (X). Insets: dependence of the total integrated PL signal on excitation power (P) on a logarithmic scale.

1.331±0.002 eV and 1.332±0.002 eV, respectively. The positions of the X and XX peaks in pristine γ-InSe are in good agreement with results from the literature (Shubina et al. (2019); Abay et al. (1998)). However, the X-X peak position is at a higher energy in both samples than the 1.32 eV peak reported previously (Shubina et al. (2019)).

The insets in Figures (5.5b) and (5.5a) show the dependence on power

(P) of the integrated intensity of the PL spectrum (I) in pristine and hydrogenated γ-InSe. This is described by a power law $I \sim P^{\alpha}$ (Nakayama et al. (2010)). In both samples two distinct regions can be seen. In the pristine sample, α increases from $\sim$1.0 to $\sim$2.8 with increasing power. A similar behaviour is observed in the hydrogenated sample with the value of α increasing from $\sim$1.0 to $\sim$2.3 going from low to high powers. The superlinear dependence at high power reflects the contribution to the PL from XX and X-X recombination. The onset of the superlinear dependence occurs at higher power in the hydrogenated sample than in the pristine sample by approximately one order of magnitude when all the tested control and hydrogenated samples were considered. This suggests an increasing concentration of defects and/or impurities in these samples, causing the recombination of carriers from these states to acquire importance relative to that of free excitons. This finding and the lower room temperature PL intensity in the hydrogenated samples suggests that hydrogen acts as a centre for non-radiative recombination of carriers in H-ion exposed samples.

If H_2 is present in H-ion exposed samples then a phase-transition might be observed upon varying the temperature. Figure (5.6) shows the temperature dependence of the PL signals in masked and H-ion exposed γ-InSe. A small difference is apparent between the two samples at 10 K due to the reduced excitonic features in hydrogenated γ-InSe. Otherwise, both samples PL signals progress in the same manner towards the expected room temperature lineshapes with the two samples lineshapes and peak positions indistinguishable by 80 K.

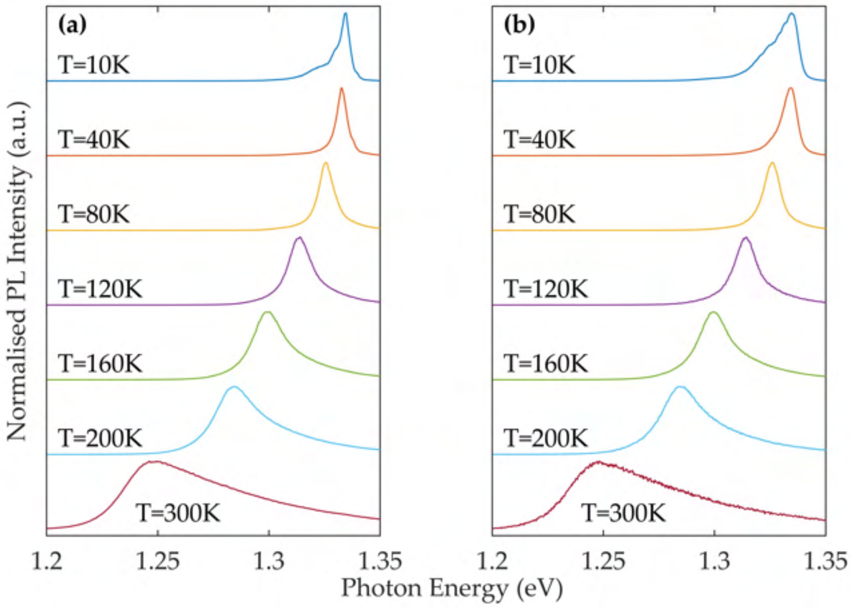

Figure 5.6: PL spectra between $T = 10$ K and 300 K of (a) masked γ-InSe and (b) H^+ exposed γ-InSe (10 eV) ($\lambda = 532$ nm, $P = 2.05$ mW, 100× objective).

5.3 Interaction with Molecular Hydrogen

The interaction of InSe with molecular hydrogen is important in understanding the applicability of InSe to hydrogen technologies and in assessing the ability for molecular hydrogen to modify γ-InSe, for example, via intercalation, as considered in Figure (5.1b).

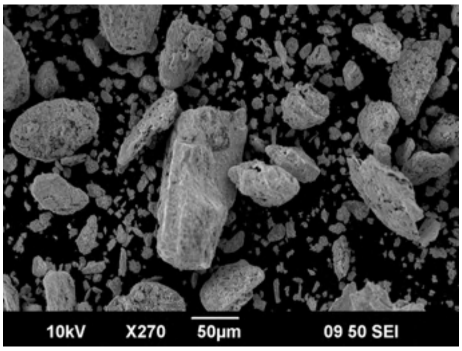

Figure 5.7: SEM image of powdered γ-InSe.

The samples considered in this study are bulk freshly exfoliated γ-InSe and powdered γ-InSe (shown in Figure (5.7)). An additional mechanically exfoliated InSe sample was stamped onto an SiO_2/Si substrate for use in optical studies. Hydrogen exposures were conducted using the Sieverts apparatus described in section 3.2.1. Of interest here are two distinct, but related phenomena: first, whether hydrogen can be intercalated within the vdW gaps present in InSe, relevant to potential applications in hydrogen storage, purification, and sensing; second, what modification can be introduced to the InSe crystal via an interaction with hydrogen. These aspects are examined below.

5.3.1 Pressure Studies

The Sieverts apparatus used to assess the uptake of H_2 consists of two connected chambers of known volume which can be separated or connected via a valve with a pressure transducer attached to the non-sample chamber (manifold). The sample is placed into one of these chambers and both are evacuated. With the chambers separated, the empty chamber is filled with a known pressure of H_2 gas and allowed to stabilise. The valve connecting the two chambers then is opened to allow the gas to interact with the sample. If the hydrogen does not interact with the sample, then the pressure in the combined chambers should match that expected from the non-ideal gas equation. Any deviation from the expected pressure indicates an uptake of H_2 by the sample. This uptake is then converted to a weight percentage (wt%), an important figure of merit for hydrogen storage in mobile applications. The approximate error in wt% for an InSe sample in this system is 0.1 wt% . A full description of the operating principles and calibration of the Sieverts system is given in section 3.2.1.

Bulk samples of InSe, grown via the Bridgman method, were the first to be investigated. The typical size of the samples is approximately $2\times5\times1$ mm^3.

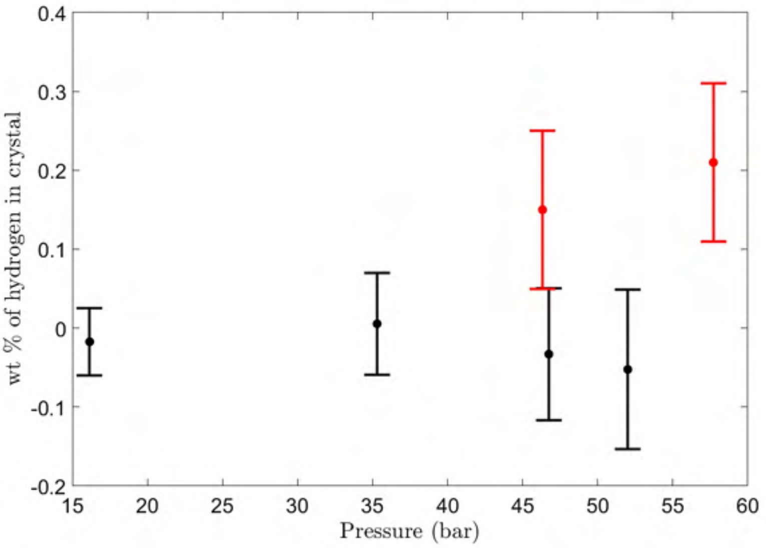

Figure 5.8: The room temperature uptake isotherms of (black) bulk γ-InSe and (red) powdered γ-InSe.

The second set of samples to be investigated were powdered InSe with a particle size of 5-200 μm. Figure (5.8) shows the isotherm generated for bulk InSe (black) and powdered InSe (red). Here, the wt% is plotted against the H_2 gas pressure. The isotherm generated for bulk γ-InSe does not reveal any hydrogen uptake. However, the powdered InSe sample does indicate some incorporation of H_2. Additionally, pressure against time plots recorded on the powdered γ-InSe sample were consistent with hydrogenation upon increasing pressure and dehydrogenating upon decreasing pressure. What is not clear from the gas-uptake measurements is the method and location of the hydrogen incorporation and whether the powdered uptake is a result of surface adsorption or a greater ability for intercalation.

5.3.2 Photoluminescence and Raman Studies

As with the samples of γ-InSe exposed to H-ions via a Kaufman ion source, any modification of the γ-InSe crystal structure induced by hydrogenation can be expected to produce a corresponding change in the PL and Raman spectra.

PL and Raman measurements were performed on InSe before and after exposure to H_2. In this instance, as the mass limitations of pressure studies don't apply, additional mechanically exfoliated samples were also studied. Figures (5.9a) and (5.9b) show the PL and Raman spectra, respectively, of a typical exfoliated γ-InSe flake. The exposure has very little effect on either the PL or Raman spectra. The PL spectra show a slight reduction in intensity by 1.9×, whereas the Raman spectra reveal an increase in intensity by 1.3×. Changes of this scale could arise from slight differences in the optical excitation and detection between the samples resulting from experimental variation.

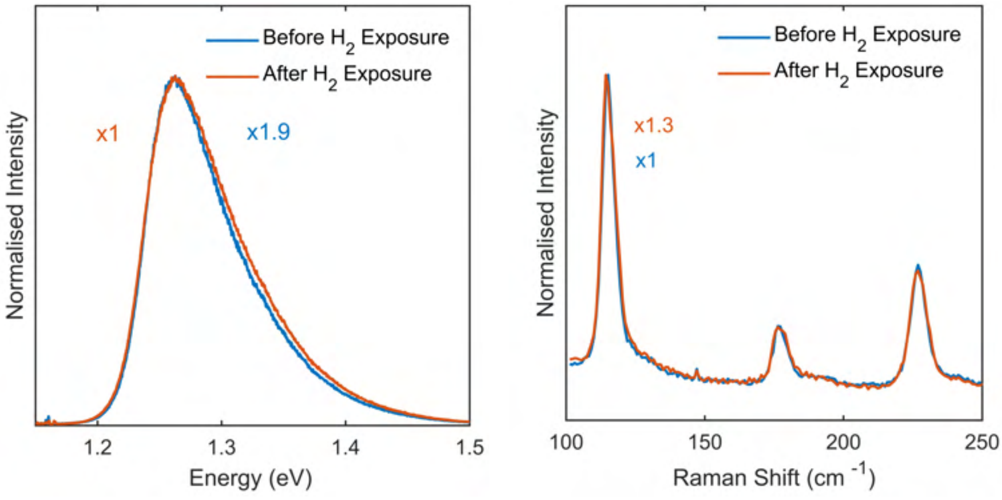

(a) (b)

Figure 5.9: (a) Room temperature PL of mechanically exfoliated γ-InSe on a SiO_2/Si substrate before and after exposure to H_2 ($\lambda = 532$ nm, 100× objective). (b) Room temperature Raman spectra of the same flake ($\lambda = 532$ nm, 100× objective).

It might be expected that the powdered samples show a more pronounced modification in optical properties given that they demonstrated a greater hydrogen uptake than single crystals. Shown in Figure (5.10) are the PL and Raman spectra from γ-InSe powder before and after exposure to hydrogen. The PL measurements reveal a large inhomogeneity across different locations of the sample. This is likely due to degradation in the samples resulting from the milling process. Overall, the typical PL intensity remains unchanged by the H_2 exposure and any shift in the PL peak position, or the emergence of new components, is masked by the variation between sample locations.

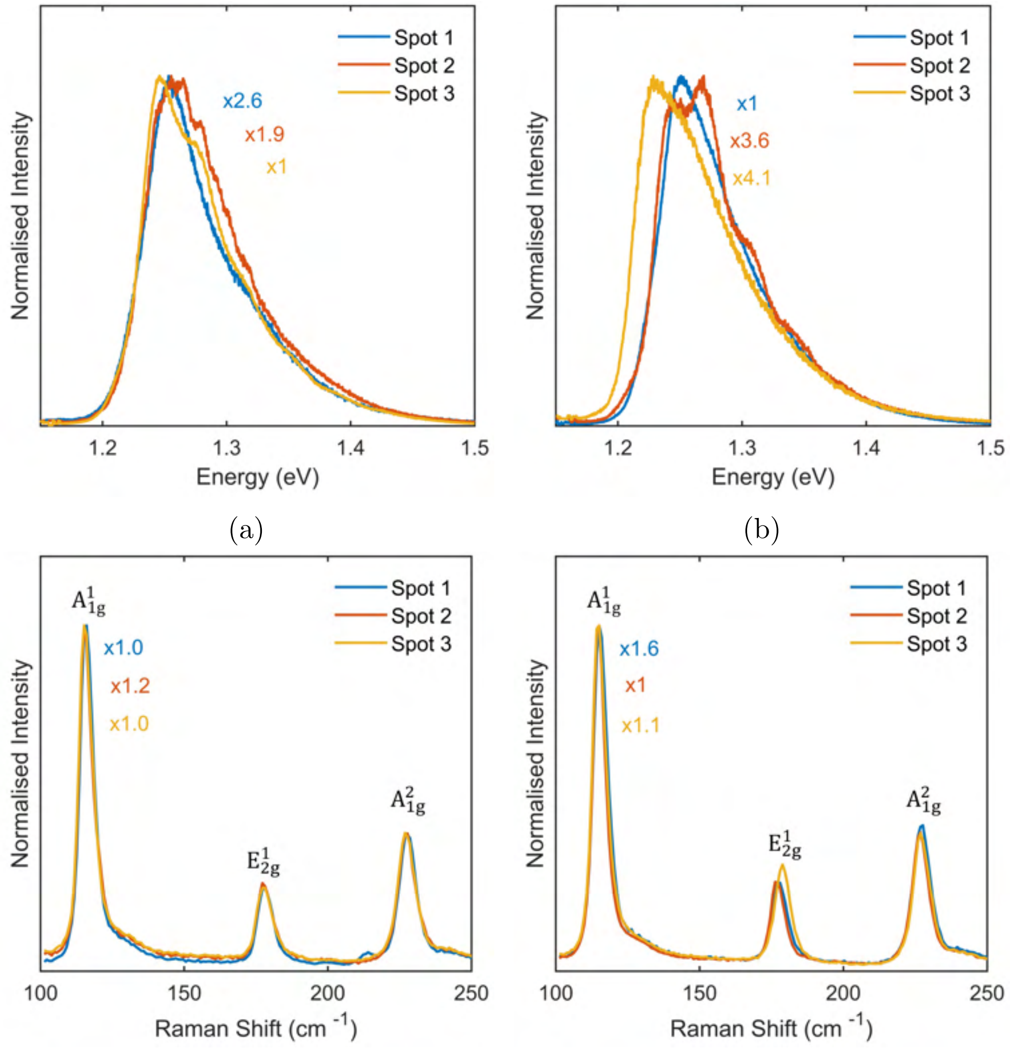

(a) (b)

(c) (d)

Figure 5.10: Normalised PL measurements of (a) pre-exposure γ-InSe powder and (b) post H_2 exposure γ-InSe powder. Normalised Raman measurements of (c) pre-exposure γ-InSe powder and (d) post H_2 exposure γ-InSe powder. All measurements conducted with $\lambda = 532$ nm, through a 100× objective. PL measurements used a 150 g/mm grating and Raman measurements utilised a 1200 g/mm grating.

The Raman spectra, shown in Figures (5.10c) and (5.10d), also reveal very little changes resulting from hydrogen exposure. The variation between location in the Raman measurements is less than that for the PL measurements, with the most significant variation seen in the E^1_{2g} peak. However, despite this greater uniformity, there is no change that can be attributed to the presence of H_2.

5.3.3 Computational Studies

Given that uptake of H_2 has been recorded in powdered γ-InSe (see Figure (5.8)), it is perplexing as to why there is no change attributable to H_2 present in either PL or Raman measurements. There are two potential explanations for this. First, that H_2 does not remain in the crystal at pressures below the pressure at which it was hydrogenated. There is some experimental evidence for this from the de-hydrogenation gas-uptake measurements. Second, that the PL and Raman properties of the γ-InSe crystals are very weakly modified by the incorporation of hydrogen. To test these possibilities a number of thermodynamic calculations were conducted.

Table 5.1: Energy cost of introducing H_2 into various sites of the InSe crystal in kJ mol^{-1} as determined by DFT. The number in brackets indicate a calculation where the InSe crystal is allowed to relax. All other numbers assume no relaxation of the crystal just atomic positions.

γ-InSe Bulk	**Interlayer**	**Intralayer**
	30.1 (29.3)	19.8
InSe Monolayer	**On Surface**	**Intralayer**
	-6.0	20.7

Thermodynamic calculations conducted using DFT can be used to determine the formation enthalpies of different states. As such, it can then be used to determine the energy associated with incorporating hydrogen in different locations within a structure as compared to the pristine structure and free hydrogen. Table (5.1) shows the results of such calculations for

H_2 introduced to γ-InSe and monolayer-InSe in various configurations. In bulk γ-InSe the incorporation of H_2 in both the interlayer and intralayer spaces is found to be favourable. Unintuitively, it is the incorporation in the intralayer space which is found to be the more favourable of the two configurations. An additional consideration can be made when the cell parameters of the γ-Inse crystal are allowed to relax. In the interlayer configuration, this slightly lowers the energy cost associated with hydrogen incorporation. This requires an increase in the size of the vdW gap from 3.6 Å to 6.1 Å. When interaction with an InSe monolayer is considered, the surface adsorption of H_2 is seen to be favourable. As with γ-InSe, the introduction into the intralayer space remains unfavourable.

It is clear from DFT calculations that the incorporation of hydrogen in the interlayer space of γ-InSe is energetically unfavourable. This may be due to the high electron densities in the interlayer space of γ-InSe (Li et al. (2019); Sun et al. (2018)). However, the cost of this incorporation can be lowered by allowing an increase in the size of the vdW gap.

A full description of the gap-size dependence of hydrogen uptake in γ-InSe was achieved via Grand Canonical Monte Carlo (GCMC) simulations. This process randomly samples the potential landscape of the crystal to determine the preferred sites of adsorption and/or absorption. The final spatial distribution is then given by molecules accepted or rejected from specific sites based on their available thermal energy and the energy required for incorporation.

Figure (5.11) shows the heatmaps generated for H_2 at 298 K and a pressure of 20 bar for an unmodified vdW gap (Figure (5.11a)) and a sequence of 1 Å vdW gap increases in Figure (5.11b - 5.11f). For the unmodified gap, the site of greatest H_2 incorporation is the surface exposed to H_2 gas. Upon

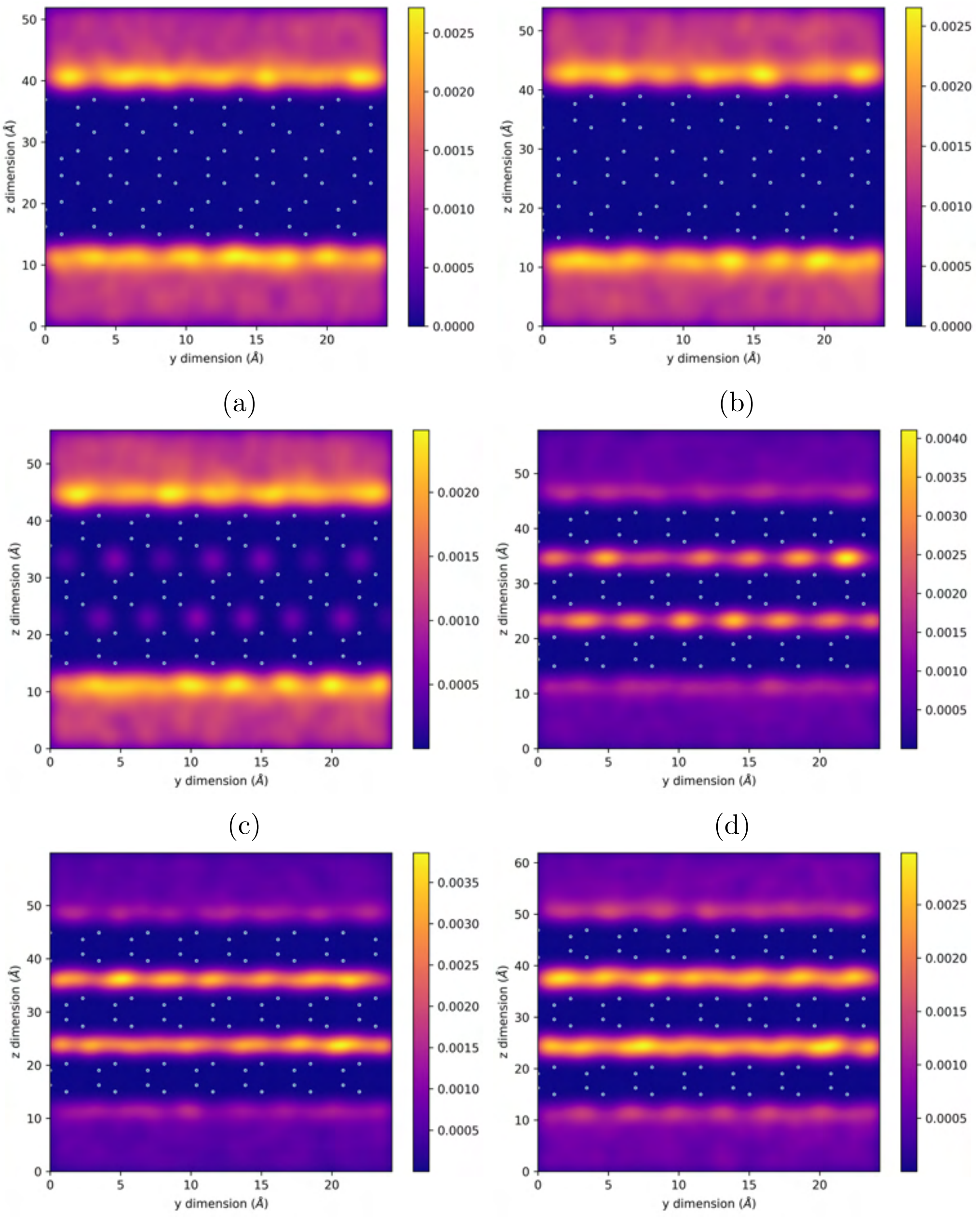

(a) (b)

(c) (d)

(e) (f)

Figure 5.11: Heatmaps showing the H_2 density within a γ-InSe crystal at 20 bar, as calculated using kernel density estimation from GCMC simulations for (a) unmodified γ-InSe, (b) γ-InSe with the vdW gap increased by 1 Å, (c) with the vdW gap increased by 2 Å, (d) with the vdW gap increased by 3 Å, (e) with the vdW gap increased by 4 Å and (f) with the vdW gap increased by 5 Å.

increasing the size of the gap, the concentration inside the gap increases. In particular, when the size of the gap is increased by 3 Å or greater there is a greater concentration of H_2 in the vdW gap than on the crystal surface. A significant increase in the concentration of H_2 within the vdW gap happens for increases of 2.5 Å or above. This compares to the kinetic diameter of the hydrogen molecule of 2.9 Å (Ismail et al. (2015)).

Hydrogen-uptake isotherms generated from GCMC simulations support the data shown in the heatmaps. Figure (5.12) shows the hydrogen loading in three layer InSe. The isotherms with a the increase of the vdW gap of <2.5 Å represent the hydrogen adsorption on the surface, whilst those of >2.5 Å indicate the hydrogen incorporated within the gaps. There is very little difference in the uptake within those systems with the gap increase ≥3 Å and within those with a gap increase ≤2 Å. The inability of H_2 to enter the interlayer space may be due to the nature of the P_z orbitals which project into the interlayer space and result in a high interlayer electron density (Li et al. (2019); Sun et al. (2018)).

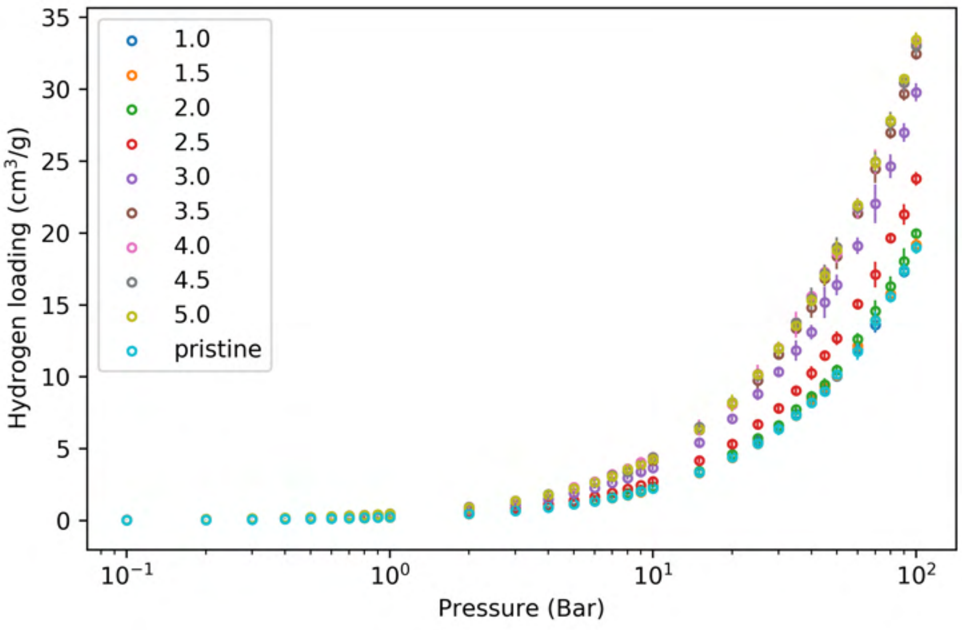

Figure 5.12: Hydrogen uptake isotherms generated from GCMC simulations at 298 K for γ-InSe crystals with different increases in the size of their vdW gaps.

As was done for H^+ exposed γ-InSe, the phonon density of sates can be calculated for H_2 incorporated γ-InSe. Figures (5.13a) and (5.13b) show the simulated phonon modes of pristine γ-InSe and hydrogen intercalated γ-InSe as shown in Figures (5.1a) and (5.1b), respectively. The peaks in the phonon density of states are noticeably narrowed between 150 cm^{-1} and 190 cm^{-1} in the hydrogenated structure. A new peak emerges between 230 cm^{-1} and 233 cm^{-1} associated with translational modes of hydrogen within the vdW gap. The position of the active Raman modes is also seen to shift with the A^1_{1g} peak shifting from 98 cm^{-1} to 100 cm^{-1}, the E^1_{2g} mode shifting from 163 cm^{-1} to 161 cm^{-1} and the A^2_{1g} shifting from 206 cm^{-1} to 214 cm^{-1}. It is notable that the A^1_{1g} and A^2_{1g} modes shift towards their monolayer values (shown in Figure (5.13c)). This is not true for the E^1_{2g} mode, likely due to the displacement of the atoms in this mode being parallel to the vdW gap rather than normal to it as in the case of the A^1_{1g} and A^2_{1g} modes.

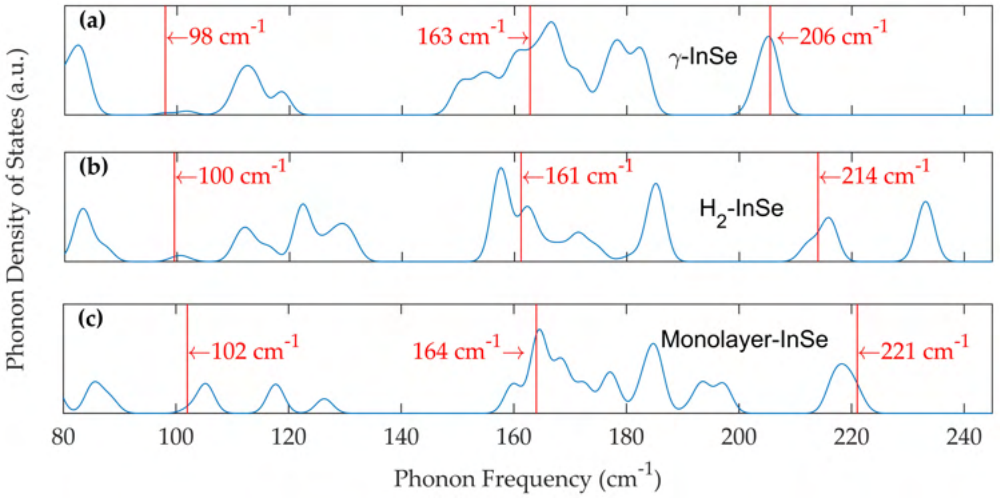

Figure 5.13: DFT-calculated phonon density of states in: (a) Bulk pristine γ-InSe, using a 3×3×2 supercell, (b) Bulk γ-InSe intercalated with H_2 using a 3×3×2 supercell and (c) monolayer-InSe. The phonon density of states are Gaussian broadened with $\sigma = 1.5$ cm^{-1}. Vertical red lines mark the position of the A^1_{1g}, E^1_{2g} and A^2_{1g} active Raman modes.

5.4 Summary

Samples of γ-InSe irradiated with H-ions from a Kaufman ion source exhibited suppressed room temperature PL intensity and decreased excitonic character at low temperature. This indicates that hydrogen acts as a centre for non-radiative recombination of photo-generated carriers. The incorporation of hydrogen was found to modify the A^1_{1g} Raman mode of γ-InSe. This modification is qualitatively consistent with the binding of atomic hydrogen to the selenium atoms in the crystal (shown in Figure (5.1c)) and is considered the most likely scheme of modification. Gas uptake measurements have indicated the ability for molecular hydrogen incorporation in powdered γ-InSe. Time-dependent uptake measurements and the lack of modification in PL and Raman properties of the crystal indicate that the hydrogen does not remain in γ-InSe under ambient conditions. This is supported by DFT measurements which indicate that the incorporation of hydrogen is unfavourable under ambient conditions. Upon increasing the size of the vdW gap by 2.5 Å the incorporation of H_2 becomes favourable and the phonon density of states becomes more monolayer-like in nature. This finding suggests an interesting possibility to create thin layers via intercalation with H_2 and to modify the interlayer phonon coupling of bulk-like γ-InSe. This possibility could be explored in future experiments at higher H_2 pressures and or temperatures.

The behaviour of hydrogen in γ-InSe is qualitatively different from that observed in other vdW crystals, such as the transition metal dichacogenides, where the presence of hydrogen in the vdW gap leads to the formation of hydrogen filled 'bubbles' (Tedeschi et al. (2019)). A possible reason for the difference in phenomenology is the strong interlayer vdW interaction of γ-Inse, owing to the projection of P_z orbitals into the vdW gap (Li et al.

(2019); Sun et al. (2018)). This is evidenced in the similarities between the kinetic diameter of the H_2 molecule and the vdW gap increase required for the successful incorporation of hydrogen.

Chapter 6

Gallium Selenide for Photocatalysis

This chapter considers the interaction between water and GaSe. This is relevant to the application of solar water splitting, a low carbon method of hydrogen production. Specifically, the modification of the valence band of GaSe by adsorbed water species and permanent water-induced oxidation is considered. This was assessed via the techniques of near ambient pressure X-ray photoelectron spectroscopy (NAP-XPS), atomic force microscopy (AFM), ultraviolet photoelectron spectroscopy (UPS), Raman spectroscopy, photoluminescence spectroscopy (PL) and angle resolved photoelectron spectroscopy (ARPES). The results reveal the morphology of partially oxidised GaSe as well as the water-induced band bending in GaSe and modifications to the valence band of GaSe by partial oxidation. The NAP-XPS work was conducted at the University of Nottingham in collaboration with Jack Hart, a PhD student of Dr James O'Shea; the AFM was conducted in collaboration with Dr Vladimir Korolkov (Park Systems) as well as with Dr Jonathan Bradford (University of Nottingham).

Contents

6.1 GaSe for Solar Water Splitting

The process of solar water splitting utilises the energy of incoming solar photons to generate a photovoltage for the separation of water into hydrogen and oxygen. In solar water splitting devices the photovoltaic and water splitting components are integrated into the same device. In principle, this has the ability to achieve solar to hydrogen efficiencies greater than that in systems where the photovoltage generation and water splitting are performed by two separate devices, for example by a photovoltaic panel connected to an electrolyser (Juodkazytė et al. (2016)). The difficulty in realising integrated solar water splitting devices is the need for materials with the properties required for both the photovoltaic and catalytic components of a device. Specifically, the photovoltaic requirements are for a material with efficient absorption of the solar spectrum, an ability for efficient charge carrier separation, long carrier lifetimes and a sufficiently large band gap. The catalytic requirements are for large specific surface areas, efficient species (H_2O, OH^-, H^+, O_2 and H_2) adsorption/desorption, and suitably aligned electronic band edges.

2D and vdW crystals are natural candidates when looking for materials with the properties required for photocatalysis. They inherently have large surface area to volume ratios, have been shown to exhibit excellent optoelectronic properties (Lee et al. (2008); Miró et al. (2014)), and with band gaps tuneable through quantum confinement, alloying and strain (Naumis et al. (2017); Kudrynskyi et al. (2020)). It is important when identifying candidate vdW materials for solar water splitting that they meet certain conditions. The first consideration is the suitability of their band edge positions. This requires that the material has a band gap greater than the redox potential of water (1.23 V) and that the conduction band minimum

(CBM) is located higher than the H^+/H_2 redox potential, while the valence band maximum (VBM) is located below the H_2O/O_2 redox potential (Jiang et al. (2017)). These conditions ensure that charge transfer at the material-electrolyte interfaces is favourable. Depending on the device structure the position of the band edges might only need to be satisfied at one interface. Typically, these devices would also require an additional external bias to operate (Jiang et al. (2017)).

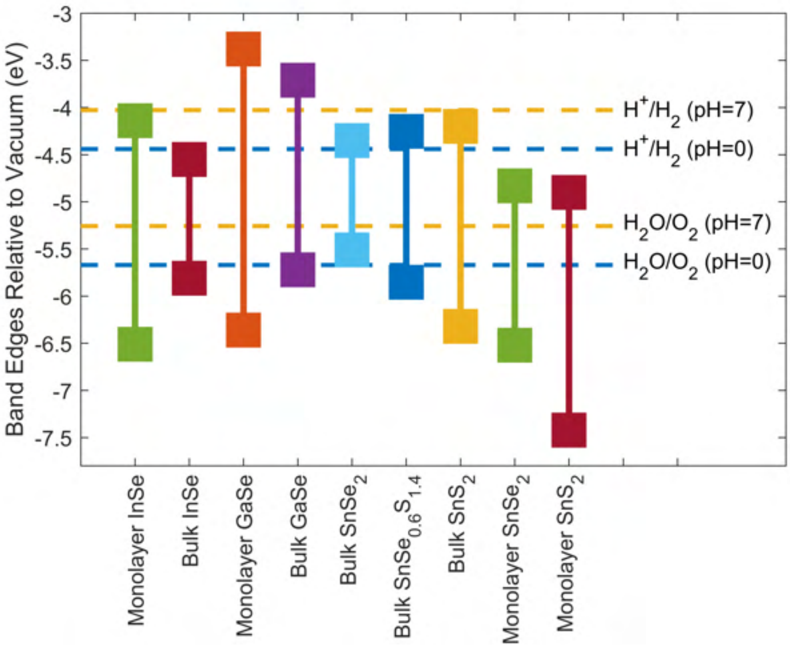

Figure 6.1: The position of the valence band and conduction band edges of various vdW materials relative to the vacuum level and compared to the H^+/H_2 and H_2O/O_2 redox potentials. Band edge positions extracted from the literature (Zhuang and Hennig (2013a); Lang et al. (1999); Brudnyi et al. (2015); Zhuang and Hennig (2013b); Fu et al. (2019); Kudrynskyi et al. (2020)).

Figure (6.1) shows the band edge positions for a selection of vdW materials relative to the water redox potentials at pH = 7 and pH = 0. The ability for the reduction in dimensionality of vdW crystals to modify the band edge positions and consequently the suitability of a materials for photocatalysis is demonstrated here. Whilst monolayer InSe, monolayer GaSe, bulk GaSe, bulk $SnSe_{0.6}S_{1.4}$ and bulk SnS_2 all have suitable band edge positions for water splitting at pH = 0, only bulk and monolayer GaSe are suitable when the pH = 7. Bulk GaSe has a band gap of 2.02 eV, whilst monolayer GaSe has a larger band gap of between 3 eV and 3.5 eV (Ferrer-Roca et al. (1999); Rybkovskiy et al. (2011)). Both of these values are above the 1.23 eV minimum required for water splitting and sit within the optimum 1.8 eV - 3.2 eV range required for efficient absorption of the solar spectrum and for generating a suitably large overpotential required for overcoming energetic barriers (Jiang et al. (2017)).

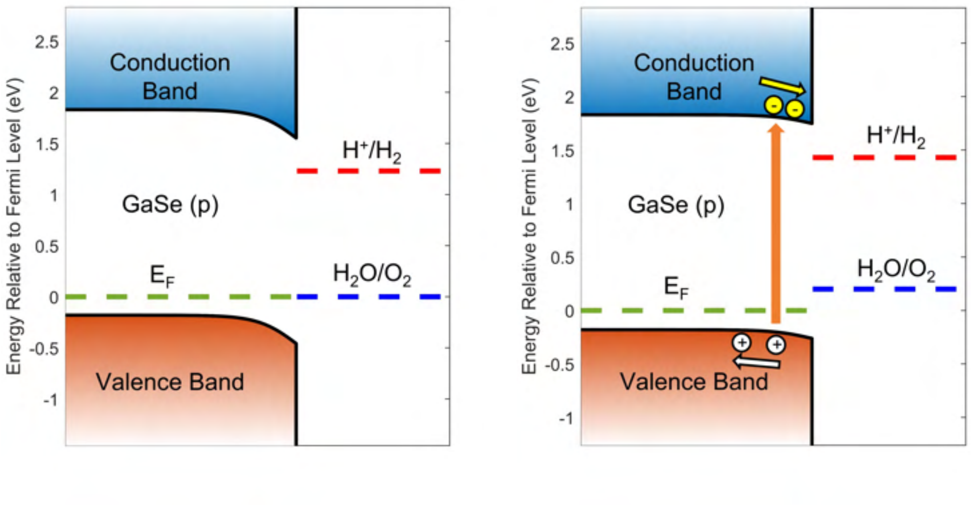

(a)

(b)

Figure 6.2: The water induced band bending of the GaSe valence and conduction bands near the surface in bulk GaSe under (a) dark conditions and (b) illumination.

When placed into water, a semiconductor will experience band bending at the surface. The nature of the band bending is dependant on the conductivity type of the semiconductor and the position of its Fermi level relative to the water redox potential. In n-type semiconductors the band bending will act to align the Fermi level at the surface with the H^+/H_2 redox potential, in p-type semiconductors the Fermi level will instead align with the H_2O/O_2 potential (Jiang et al. (2017)). As GaSe is a p-type conductor, the Fermi level aligns with the H_2O/O_2 potential. This is shown in Figure

(6.2a) for bulk GaSe. As the position of the Fermi level in bulk GaSe is below the H_2O/O_2 potential, a downward band bending of up to 0.3 eV would present at the surface if the alignment is assumed to take place entirely in GaSe (Balakrishnan et al. (2014)). The origin of the bending is charge transfer between the highest occupied molecular orbital (HOMO) of the water and GaSe. In the electrolyte this corresponds to a higher concentration of negatively charged water species on/near the surface and the establishment of a Helmholtz layer (Jiang et al. (2017)). A consequence of the band bending is an ability for the separation of mobile charge carriers. Shown in Figure (6.2b) is a sketch of the band bending induced by the separation of photogenerated carriers in water exposed GaSe when illuminated with photons with an energy greater than the band gap. Electrons move towards the surface of the material whilst holes move towards the bulk. This has the effect of reversing some of the water induced band bending and flattening the bands due to a slight build up of negative charge near the surface.

The ability for GaSe to to act as both a catalyst and photocatalyst has been demonstrated previously (Zappia et al. (2020); Meng et al. (2022)). In these reports, various modifications have been made to GaSe with the intention of improving its catalytic properties. For example, GaSe-based nanoribbons have a larger surface area than that of a planar structure (Zappia et al. (2020)). Similarly, optimisation for the adsorption/desorption of species has been achieved by creating local catalytic centres via oxidation (D'Olimpio et al. (2020)). However, the optimisation studies often fail to consider the effect of the modifications on other properties required for photocatalysis. For example, the increasing catalytic activity via oxidation would also be expected to introduce centres for charge carrier recombination and might also modify the band edge positions and optical absorption characteristics.

With these concepts in mind, it was decided to investigate some of the properties of GaSe relevant for water splitting. Given the propensity for oxide formation in GaSe exposed to water, it is important that the modification of the electrical band structure and the positions of the band edges are understood in oxidised GaSe. For this purpose the techniques of near ambient pressure X-ray photoelectron spectroscopy (NAP-XPS), atomic force microscopy (AFM), ultraviolet photoelectron spectroscopy (UPS), Raman spectroscopy, photoluminescence (PL) spectroscopy and angle resolved photoelectron spectroscopy (ARPES) were used.

6.2 XPS Studies of the Interaction Between Water and GaSe

XPS is routinely used to study the core level electrons within a material. However, in materials with a sufficiently large XPS cross-section, it can also be used to study the valence band. The resulting spectrum reflects the density of states within the valence band of the material. Also, available in this instance, is the ability to conduct near ambient pressure XPS (NAP-XPS), which allows for in-situ XPS of systems under pressures of several mbar. This facilitates an in-situ study of the valence band and core shell electrons in GaSe before, during and after exposure to water. The system also includes a 1.5 solar global air mass simulator, which provides additional data of how the system behaves under illumination.

A sample of bulk GaSe was freshly cleaved and secured to a standard XPS sample plate using carbon tape. Whilst acting quickly to minimise air exposure, the sample was loaded into the NAP-XPS system. Once loaded and under pressures of better than 10^{-9} mbar, spectra of the valence band, O 1s, Ga 2p and Se 3d regions were obtained in dark conditions and under illumination by the solar simulator. The sample was then exposed to water vapour at 1.5 mbar (T = 298 K, 2 hours), with the same peaks measured under dark and solar simulator illumination conditions in the NAP configuration. Finally, after water exposure, low pressure ($<10^{-9}$ mbar) XPS spectra of the same peaks were recorded under dark and light conditions.

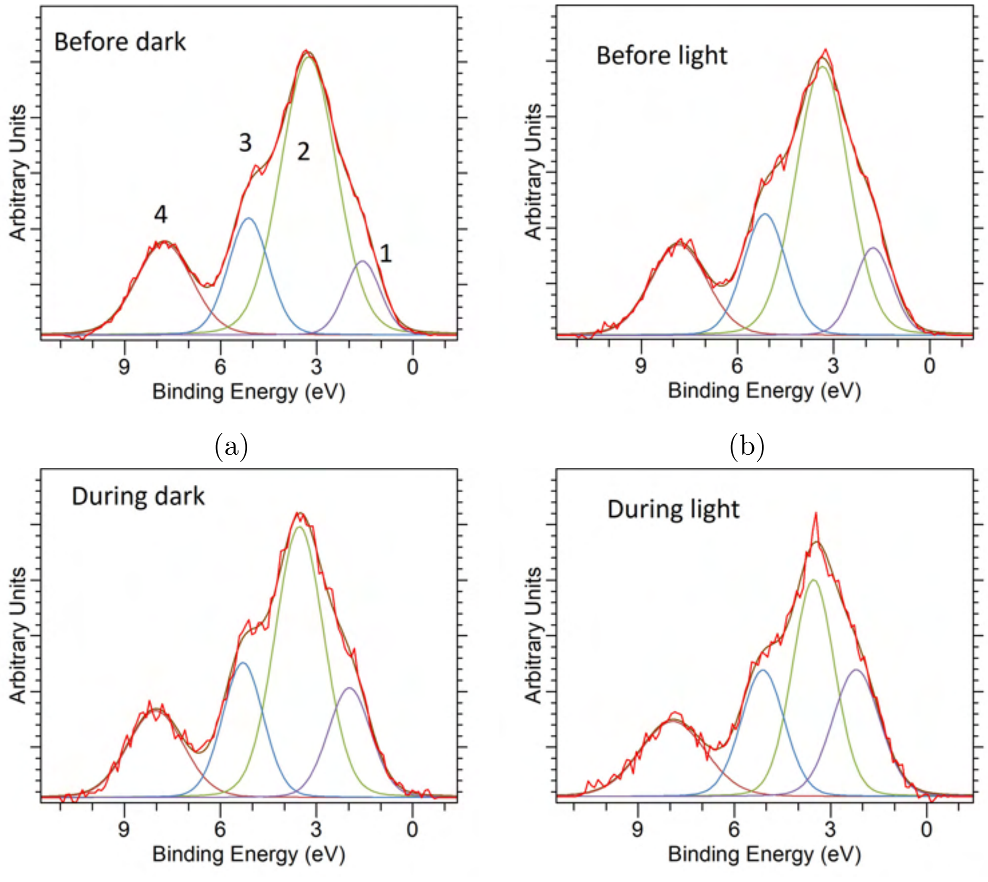

(a) (b)

(c) (d)

Figure 6.3: The XPS valence band spectra of GaSe are displayed with their component fits for samples (a) before water exposure in dark conditions, (b) before water exposure under illumination by a solar simulator, (c) during water exposure in dark conditions, and (d) during water exposure under illumination by a solar simulator. A Tougaard background and 10/90 Lorentzian Gaussian blend was used for the fitting.

Table 6.1: Valence band component positions corresponding to the fittings in Figure 6.3.

	Peak 1 (eV)	Peak 2 (eV)	Peak 3 (eV)	Peak 4 (eV)
Before Dark	1.58	3.26	5.13	7.77
Before Light	1.77	3.35	5.14	7.82
During Dark	1.97	3.53	5.30	8.02
During Light	2.20	3.46	5.11	7.92
D'Olimpio et al.	-	3.1	4.7	7.6

Figure (6.3) shows the fittings to the valence band of GaSe under vacuum and during water exposure in dark conditions and under illumination with a solar simulator. The peak positions are quoted in Table (6.1) and compared with those from air exposed GaSe obtained by D'Olimpio et al. (2020).

The fits in Figure (6.3) have been overlaid in Figure (6.4) to allow for direct comparison of the spectra. Before exposure to water, four components can be seen in the valence band spectra. Of which, peaks 2, 3, and 4 compare favourably to previously reported peaks at 3.1 eV, 4.7 eV and 7.6 eV (D'Olimpio et al. (2020)). Peaks 3 and 4 are ascribed to Ga 4p - Se 4s and Ga 4p - Se 4p states, respectively. Peak 3 is ascribed to the mixing of hybridised orbitals and peak 1 remains unattributed. The difference with the measured peak positions of peaks 2, 3, and 4 and those reported in the literature is the same at 0.16 eV. This difference is likely due to a difference of charging. The difference between the measured 5.13 eV and reported 4.7 eV is greater at 0.43 eV. This difference is currently unaccounted for but may be explained by slight differences in sample composition and/or structure. The intensity ratios of the four peaks shown in Figure (6.4a) is qualitatively the same as reported in the literature (D'Olimpio et al. (2020)). It is notable that before exposure to water, illumination by a solar simulator does not modify the valence band spectrum significantly.

In-situ NAP-XPS was conducted on the GaSe sample during water expo-

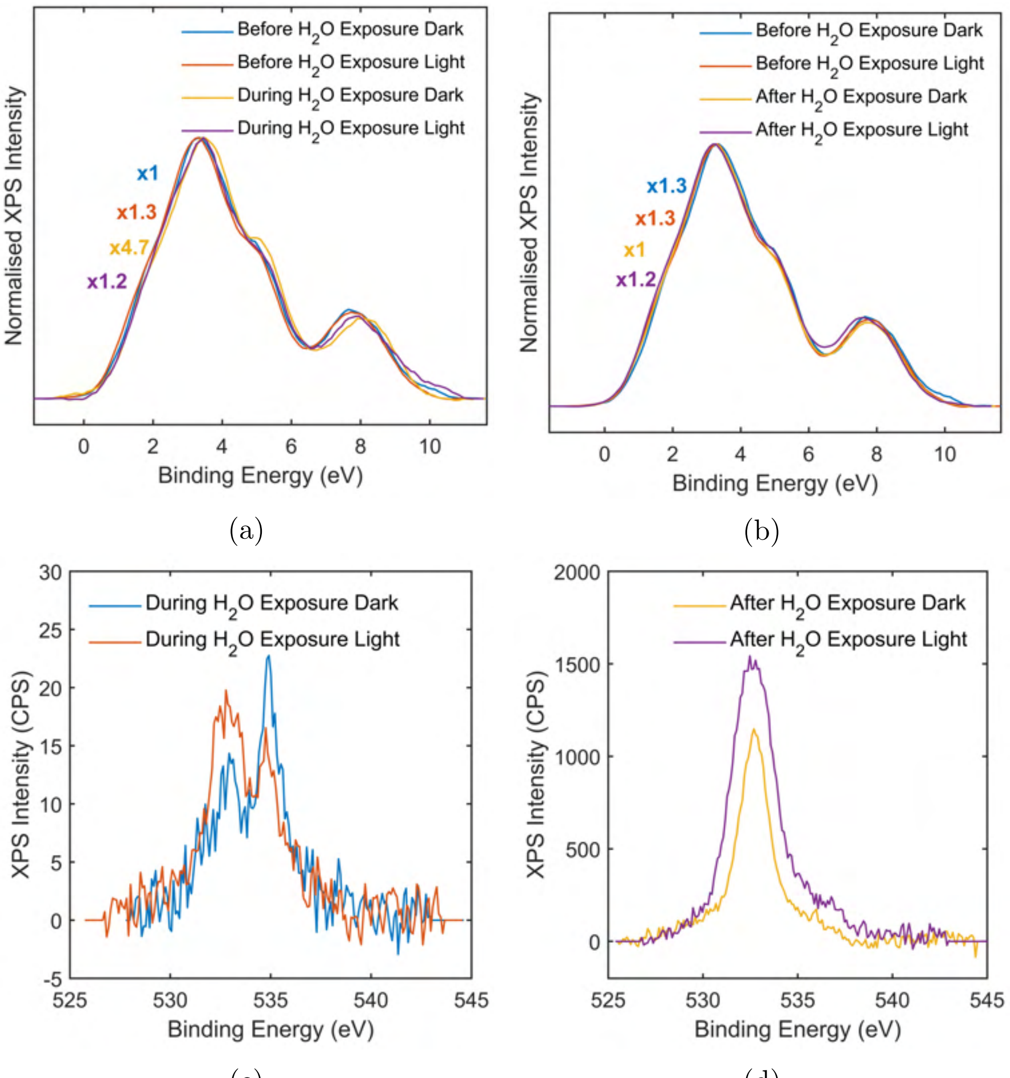

Figure 6.4: XPS spectra of a bulk GaSe sample before, during and after exposure to water vapour. The valence band spectrum (a) before and during water exposure and (b) before and after exposure. The O 1s spectrum (c) during water exposure and (d) after water exposure. Light illumination was achieved using a 1.5 global air mass solar simulator.

sure. The in-situ valence band spectra are shown in Figure (6.4a). The intensity of the valence band spectrum is reduced during the in-situ experiments due to the presence of water vapour and the geometrical restrictions of the NAP cell. With the in-situ spectra normalised to the largest peak, a change in the relative intensity of the components can been seen. The position of the most prominent peak (peak 2) is shifted by 0.27 eV to 3.53 eV, consistent with that expected for adsorbed water species of GaSe. When illuminated, the position of this peak moves to 3.46 eV. Without illumination, the peak 3 is seen to have an increased contribution as compared to the pre-exposure measurements. When the sample is illuminated, this increased contribution disappears and reverts to approximately the pre-exposure levels. Similarly, peak 4 is seen to change significantly during the water exposure under dark conditions with the peak reverting back towards the pre-exposure contribution when the sample is illuminated.

To assess any permanent changes to the valence band spectra of GaSe as a consequence of water exposure, the valence band spectra were measured before and after water exposure and are displayed in Figure (6.4b). Under dark conditions the valence band spectrum post water exposure is unchanged when compared to the before exposure measurement. However, when the sample is illuminated, a change is observed with peak 3 recording a slight increase in intensity and peak 4 seeing a larger increase in intensity.

To understand the underlying phenomena responsible for the behaviour of the valence band spectra, the core level spectra must also be studied. Shown in Figure (6.4c) and Figure (6.4d) are the O 1s spectra of the GaSe sample during and after water exposure, respectively. Before water exposure there were no O 1s associated peaks visible. The in-situ spectra, shown in Figure (6.4c), reveal the presence of two O 1s peaks at 533.2 eV and 535.3 eV, associated with oxide species and adsorbed water species, respectively (D'Olimpio et al. (2020)). When illuminated the intensity of the oxide peak increases whilst that of the adsorbed water species decreases. The post exposure XPS of the O 1s peak reveals a strong oxide associated feature and a smaller shoulder associated with residual adsorbed water species. The presence of oxides was also confirmed in spectra of the Ga 2p and Se 3d peaks, both of which displayed new components consistent with the partial oxidation of GaSe. This is shown for the Ga 2p peak in Figure (6.5),

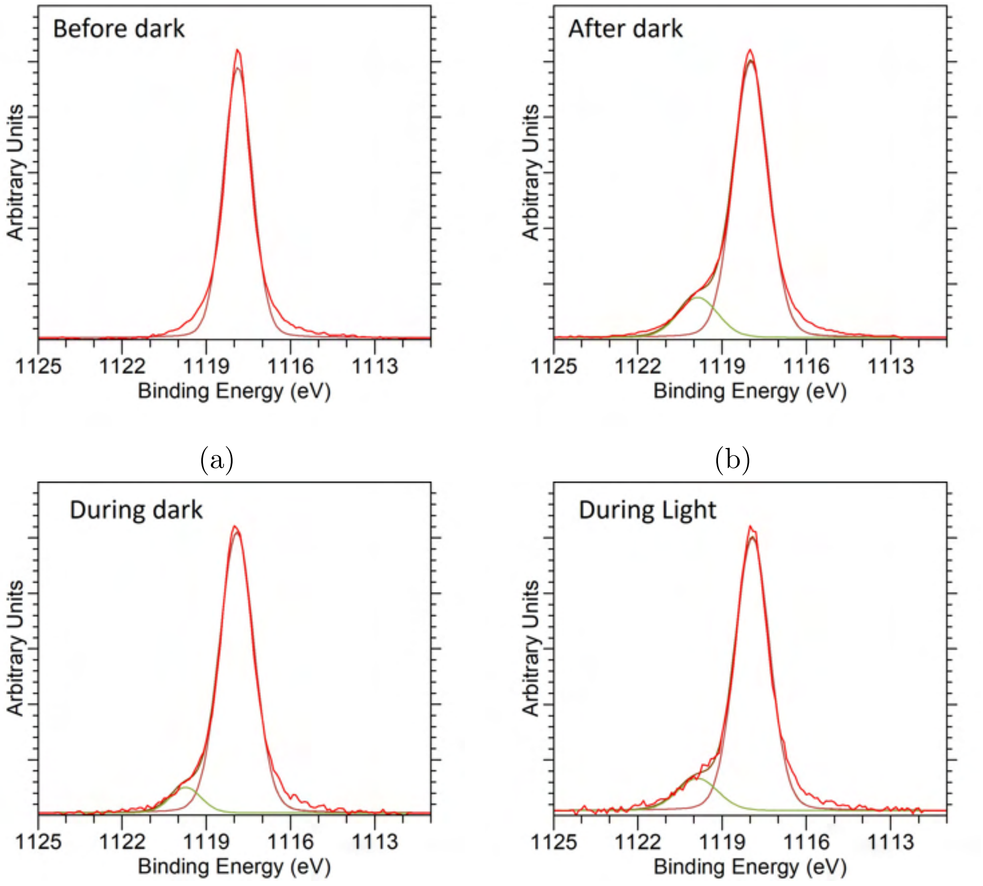

(a) (b)

(c) (d)

Figure 6.5: XPS spectra of the Ga 2P peak recorded in (a) dark conditions before water exposure, (b) dark conditions after water exposure, (c) dark conditions during water exposure, and (d) light conditions during water exposure. A Tougaard background and 50/50 Lorentzian Gaussian blend was used for the fitting.

where and oxide feature appears at a binding energy of 1119.9 eV, 1.9 eV above the previously recorded peak in unexposed GaSe. This compares to previously reported descriptions of oxidised GaSe which recorded the new feature 1.5 eV higher than in pristine GaSe (Susoma et al. (2017)). The position of the GaSe associated peak changes very little on water exposure, shifting to higher binding energy by only 0.03 eV and exhibiting no shift upon illumination. However, the oxide peak shifts to a higher binding energy by 0.13 when exposed to water under no illumination as compared to vacuum. When illuminated, the position of the oxide peak returns to its vacuum value. This indicates that the oxide is likely playing a significant role in any band bending at the surface.

The behaviour seen in the XPS spectra of GaSe in response to water exposure and illumination via a solar simulator can be understood with reference to Figure (6.2a). Upon water exposure there is a slight shift in the positions of the valence band features associated with the water induced band bending. In this instance the shift was measured at 0.27 eV in the valence band. The presence of water also modifies the relative intensities of the components in the valence band spectrum. When illuminated, many of these features shift back towards their pre-exposure positions and relative intensities (Figure (6.2b)). This is likely due to charge carrier separation taking place in the bent bands near the crystal surface, with the separated charges acting to reverse the water induced band bending. This has the secondary effect of a reduction in the concentration of water adsorbed species on the surface, as evidenced by the reduction in the water species intensity in the O 1s spectra when illuminated. A permanent modification of the material also occurs and manifests through the formation of an oxide. This oxide is likely responsible for the differences between the valence band spectra of GaSe post water exposure in the dark and under illumination.

6.3 Surface of GaSe

We conducted AFM of GaSe to gain a better understanding of its oxidation, specifically its surface morphology. The AFM measurements where performed on exfoliated large-area GaSe samples with extended areas ($\sim$ 50 - 100 μm) of thin flakes (<10 layers thick). The sample also contained thicker bulk-like flakes. The sample was on a gold substrate.

On a thick bulk-like flake investigated by AFM, bump-like protrusions in

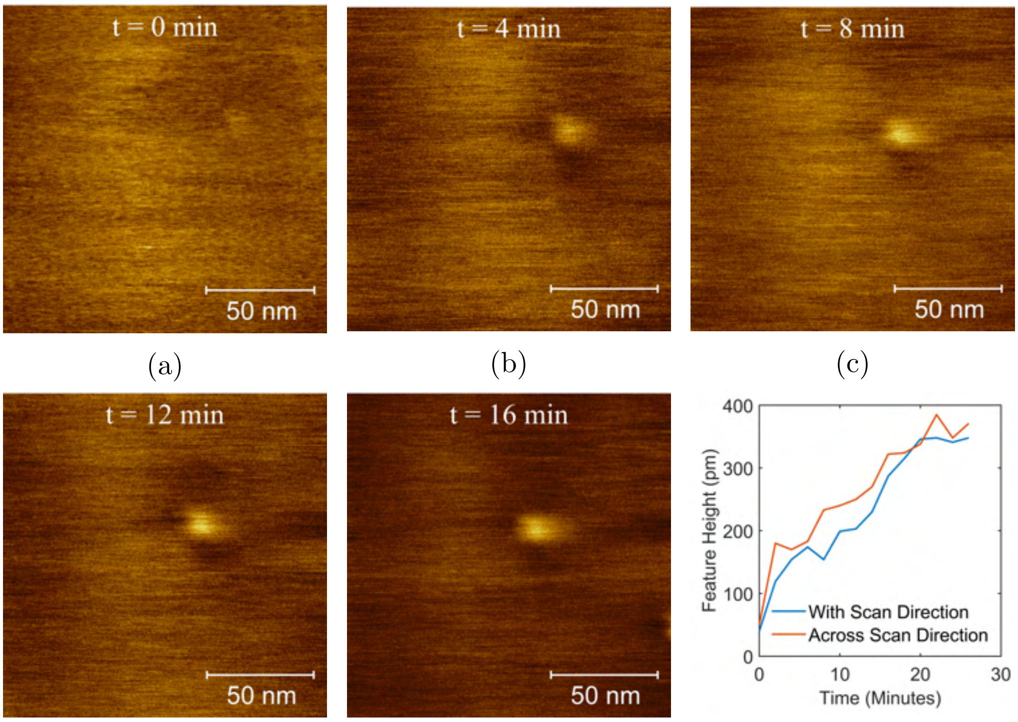

(a) (b) (c)

(d) (e) (f)

Figure 6.6: AFM height maps of the same location of a bulk GaSe flake at time (a) $t = 0$ min, (b) $t = 4$ min, (c) $t = 8$ min, (d) $t = 12$ min and (e) $t = 16$ min. (f) Plot of the feature height in (a-e) plotted as a function of time.

the surface morphology were observed. The density of these bumps was approximately 108 μm^{-2} whilst their vertical size size was up to 1.6 nm and their horizontal size was up to 36 nm. However, tip convolution (tip radius ~10 nm) can be expected to increases this value, meaning the true diameter is likely significantly smaller. Phase measurements on the bumps were out of phase with the inter-bump regions by approximately 8°, indicative of a different material composition. In the inter-bump regions the surface had a root mean square roughness of approximately 44 pm.

A similar set of observations was made on thin flakes. On a flake of thickness 1.7 nm, corresponding to 2 layers, the same bump features were observed. In this instance the density of the features was approximately 20 μm^{-2}, with a maximum vertical size of approximately 0.9 nm and approximate maximum width of 50 nm (with tip convolution). The difference in bump size and density is likely due to the difficulty in accurately identify the bump features as a result of the increased roughness of the thin flake at 0.17 nm.

When measuring the surface roughness of an inter-bump region of the bulk-like GaSe flake, it was fortuitous that the growth of a new bump feature was observed. A sequence of AFM height maps recorded at different times during this observation are shown in Figure (6.6a - 6.6e). A similar set of AFM images recorded for phase data shows the same characteristics seen on other bump features. Figure (6.6f) shows how the feature height grows with time. It appears as though the rate at which the bump grows slows with time. It is possible that the height may even be starting to plateau, indicating a maximum/natural size of the bumps. A similar sequence of images was gathered on the thin 2 layer thick flakes with the same behaviours observed. The feature growth is reflected in the phase data, confirming suggesting that they may have a similar composition.

It is not known the mechanism which induced the formation of the bumps at the time at which AFM imaging was taking place. Tip-induced defects are a possible explanation here. Given the similarity in morphology and phase characteristics between the previously measured bumps and the bump observed during growth, it is likely that their growth mechanisms are the same. Given the ability for GaSe to oxidise has already observed via XPS (Section 6.2) and later via Raman (Figure (6.7b)), it is highly likely that the bumps are comprised of oxidised GaSe. However, their low surface coverage of less than 0.4 % suggests that the sample will contain oxide in other forms given the relatively large XPS oxide peak in Figure (6.5b).

6.4 The Optical and Electronic Properties of GaSe

It is clear from the AFM and core-level XPS data that oxidation modifies the surface of GaSe. It is also apparent from the valence band XPS data that this modification extends to the electronic band structure of GaSe. It is possible using nano electron spectroscopy for chemical analysis (Nano-ESCA), described in Section 3.2.4, to access the valence band structure of GaSe and observe the permanent modifications induced by oxidation.

A large area GaSe sample, similar to that measured in Section 6.3, was used for these experiments. As Nano-ESCA can selectively probe a surface down to a resolution of 10 μm or less, several flakes of different thicknesses were sampled. A summary of the flakes thicknesses and surface roughness, as evaluated using AFM, of the sampled flakes is shown in Table (6.2). The 100 layer and 5 layer flakes had notably rougher surfaces than the others. For the 100 layer sample this appeared to be due to surface contamination, as revealed by AFM images. For the 5 layer sample it was instead the surface of the flake in itself which appeared noticeably rougher, possibly due to increased oxidation over the other flakes.

Table 6.2: AFM derived properties of ϵ-GaSe flakes used in the Nano-ESCA studies.

Material	Thickness (nm)	No. of Layers	RMS Roughness (pm)
GaSe	80	~100	560
GaSe	4.6	6	341
GaSe	4.0	5	751
GaSe	1.6	2	240
Substrate (Au)	-	-	270

The first tool available when utilising the Nano-ESCA is ultraviolet photoelectron spectroscopy (UPS), which works on the same principles as XPS but with incoming photons of energy $h\nu$ = 21.219 eV as opposed to $h\nu$ = 1486.7 eV. The reduced photon energy results in an increased interaction cross section with energy levels near the valence band maximum. This makes UPS particularly well suited to studying the valence band of a material as well as providing information on the work function.

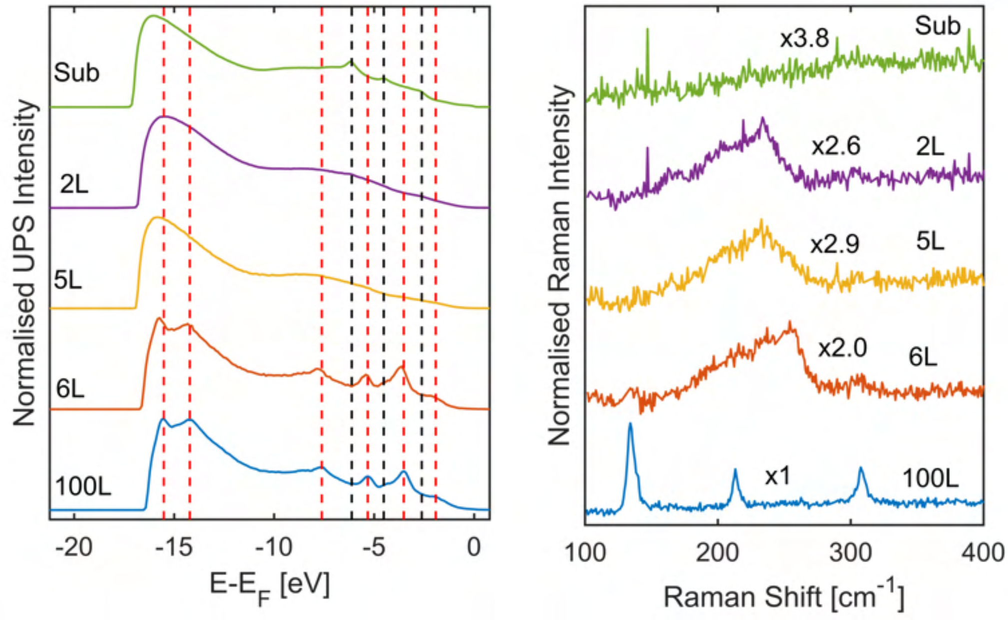

(a) (b)

Figure 6.7: (a) UPS spectra of GaSe flakes of different thickness and of the Au/Ti/SiO$_2$ substrate. The red lines correspond to the locations of significant peaks in the 100 layer bulk-like sample. The black lines correspond to the positions of significant peaks of the Au substrate. (b) Raman spectra of the same flakes studied in (a) (λ = 532 nm, T = 297 K, 1200 g/mm grating).

Figure (6.7a) shows the UPS spectra for the GaSe flakes and the Au substrate described in Table (6.2). All the spectra share some key features. Moving from left to right, the first of these features is the secondary electron cutoff characterised by a sudden increase in intensity associated with the work function of the material. Next is a large broad feature present due to the secondary electron pileup. Third is a plateau followed by a slow decline in intensity associated with the valence band states and the valence band cutoff, respectively. In some of the spectra prominent peaks can be seen. These are associated with either atomic orbitals or hybridised orbitals in the valence band. Marked in Figure (6.7a) are the positions of the most prominent peaks in the Au substrate (black vertical lines). The Au peaks are associated with the 5d band of Au and are positioned at -2.6 eV, -4.5 eV and -6.1 eV, in reasonable agreement with previously reported values (Gelius et al. (1984); Eastman and Grobman (1972)). It is possible to resolve some of the Au peaks in the 2 layer flake. In the 5 layer flake the Au peaks are no longer visible. The peaks associated with GaSe are visible in the 100 layer UPS spectrum of Figure (6.7a) and marked in red. The four features nearest the Fermi level are positioned at -1.9 eV, -3.5 eV, -5.3 eV and -7.6 eV. With reference to Figure (6.4a) and to the literature, the features at -3.5 eV and -7.6 eV are attributed to the Ga 4p-Se 4s and Ga 4p-Se 4p mixed states, respectively (D'Olimpio et al. (2020)). Two additional features are seen in the 100 layer GaSe spectrum at -14.2 ev and -15.5 eV. These peaks are attributed to the Ga 3d level (Wagner et al. (2003)). However, the difference of 1.3 eV between the two features is too great to be explained by the peak splitting of Ga 3d and instead attributed to the presence of mixed GaSe and oxidised material (D'Olimpio et al. (2020)). The GaSe peaks are also visible in the 6 layer thick sample. However, they are shifted slightly by 0.2 eV, likely due to a slight charging of the thicker 100 layer GaSe sample. In the 5 and 2 layer thick samples the peaks associated with GaSe are no longer visible.

It is not immediately obvious why the 100 layer and 6 layer GaSe flakes reveal GaSe associated UPS peaks, whilst the 5 layer and 2 layer flakes don't. An understanding of the structural properties of the various flakes achieved via Raman spectroscopy is helpful in this regard. Figure (6.7b) shows the Raman spectra gathered for each of the flakes. In the 100 layer flake three peaks are visible at Raman shifts of 134.2 cm^{-1}, 213.2 cm^{-1} and

307.5 cm^{-1}, associated with the A$_1'$(1), E$''$(2) and A$_1'$(2) Raman modes, respectively (Molas et al. (2021)). The A$_1'$(1) and A$_1'$(2) modes are still visible at a reduced intensity in the 6 layer flake. However, the E$''$(2) mode is obscured by a new broad feature between 150 cm^{-1} and 275 cm^{-1}, which is attributed to Ga_2Se_3 and amorphous selenium present due to the oxidation of GaSe (Zhao et al. (2018); Susoma et al. (2017)). With decreasing flake thickness to 5 or 2 layers the GaSe Raman peaks are no longer visible, with only the broad oxide feature remaining.

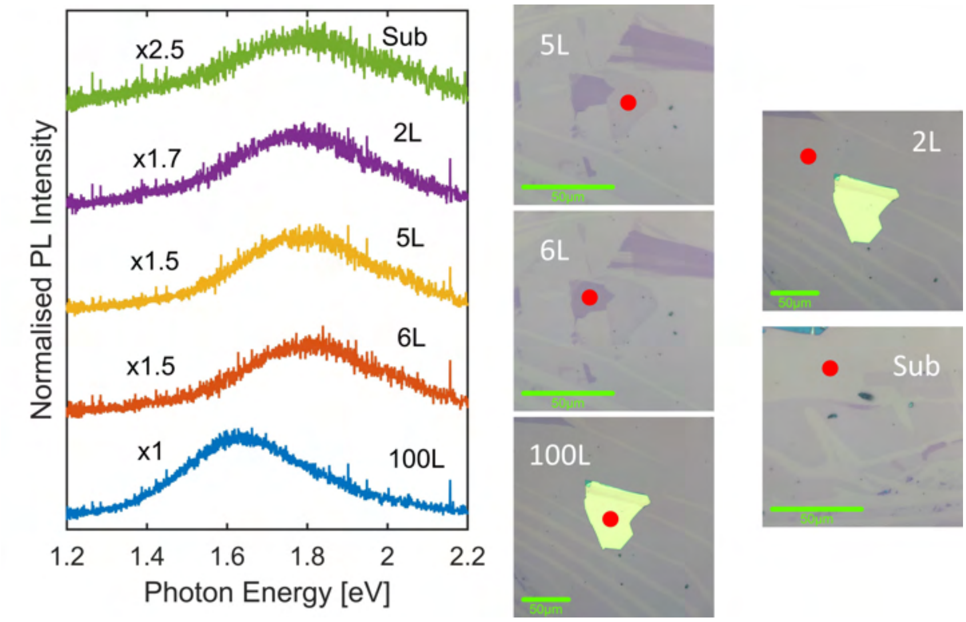

Figure 6.8: PL spectra of GaSe flakes of different thickness and of the Au/Ti/SiO_2 substrate ($\lambda = 532$ nm, $T = 297$ K, 150 g/mm grating). Optical images of the flakes are also provided with the spectra locations marked in red. These are the same locations used for the Raman and UPS measurements in Figure (6.7).

PL measurements reveal a similar trend regarding the oxidation. It would be expected for bulk-like GaSe that the room temperature PL emission would be centred at 2 eV in bulk GaSe and at 2.17 eV in 6 layer GaSe (Arutyunyan et al. (2022)). However, in the 100 layer flake the PL emission is centred at 1.63 eV, likely due to defect levels introduced in the gap via oxidation (Savchyn and Stakhira (1996)). When the thickness is reduced to 6, 5 or 2 layers, the PL emission shifts to 1.81 eV. The position of this peak aligns with that of the substrate. Thus, it corresponds to the background signal.

Another powerful tool available using the Nano-ESCA is angle resolved photoemission spectroscopy (ARPES). This, much like UPS, can selectively probe the electron energy states in a material but with additional momentum space (k-space) resolution. This information is recorded in 2D slices of the in-plane k vectors k_x and k_y at a constant energy. By stacking these slices and extracting 2D profiles, the valence band dispersion along different crystallographic orientations can be produced.

ARPES does not conserve the k_z component of momentum, it instead samples a position in k_z determined by the photon energy and projects it into a 2D image over a width in k_z, also defined by the photon energy. The width is given by Equation (3.9) and was determined to be of the order $\Delta k_z = 0.1$ Å^{-1} in the Nano-ESCA. This compares to a Brillouin zone size of 0.38 Å^{-1} along the k_z direction in GaSe. The position in k_z is given by,

$$k_z = \sqrt{\frac{2m(E_k + V_0)}{\hbar^2}}, \tag{6.1}$$

where the $\cos\theta$ term from Equation 3.8 is equal to 1 in the geometry of the Nano-ESCA. For GaSe the value of V_0 is approximately 10 eV (Plucinski et al. (2003)), and for electrons near the valence band maximum the kinetic energy is approximately 20 eV. This results in the Nano-ESCA sampling the Brillouin Zone of GaSe at $k_z = 0.04$ Å^{-1}. Given the broadening of 0.1 Å^{-1}, this range includes the Γ, M and K points. This is in agreement with previous measurements which finds a maximum in emission at Γ for normal emission with a photon energy of 23 eV (Plucinski et al. (2003)). As such, in the projected representation the points encompassing Γ, K, and M are

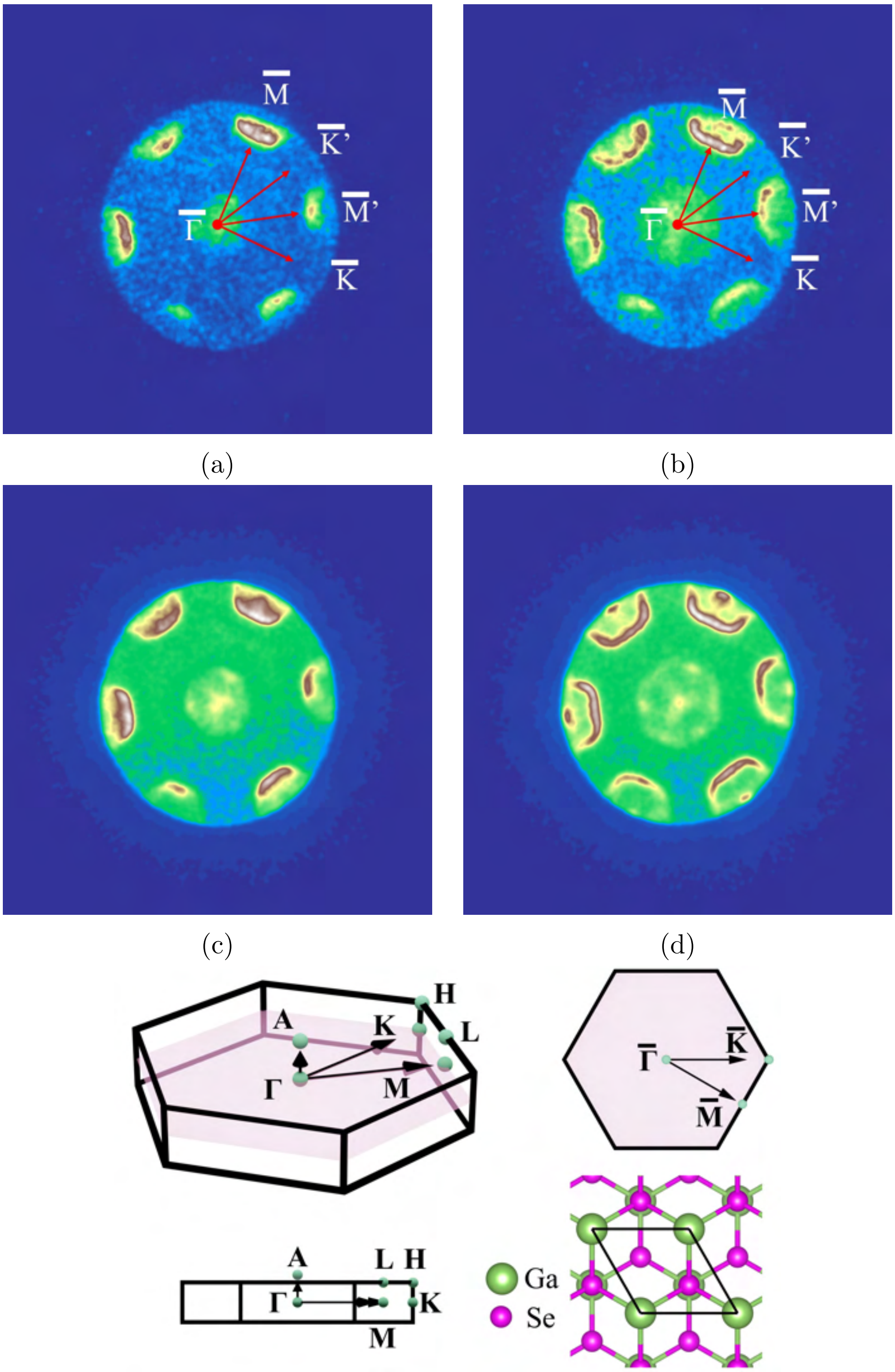

(a) (b) (c) (d) (e)

Figure 6.9: Constant energy ARPES slices of 6L GaSe at (a) 1.711 eV below the Fermi level and (b) 2.175 eV below the Fermi level. Constant energy ARPES slices of 100 layer GaSe at (c) 1.711 eV below the Fermi level and (d) 2.175 eV below the Fermi level. (e) Schematic of the 1st Brillouin zone of bulk ϵ-GaSe.

referred to as $\bar{\Gamma}$, $\bar{\mathrm{K}}$, and $\bar{\mathrm{M}}$, respectively.

Shown in Figure (6.9) are four ARPES constant energy slices recorded in 6 layer (6.9a & 6.9b) and 100 layer (6.9c & 6.9d) flakes of GaSe. With reference the 1st Brillouin zone of bulk GaSe (Figure (6.9e)) and to the literature, the high symmetry point of $\bar{\mathrm{M}}$, $\bar{\mathrm{M}}$', $\bar{\mathrm{K}}$ and $\bar{\mathrm{K}}$' alongside the position of the Γ point are marked (Chen et al. (2018b)). The M and K points are positioned 0.97 Å^{-1} and 1.12 Å^{-1} away from the Γ point, respectively. In real-space the $\bar{\mathrm{M}}$'-$\bar{\mathrm{M}}$' direction corresponds to the armchair direction in GaSe, whilst the $\bar{\mathrm{K}}$-$\bar{\mathrm{K}}$' direction corresponds to the zig-zag direction. The presence of non-degenerate $\bar{\mathrm{M}}$ and $\bar{\mathrm{M}}$' vectors is a result of a three-fold symmetry, not expected from the 6-fold symmetry present in ϵ-GaSe. As the Nano-ESCA light source is polarised, this effect is most likely due to the sample. In fact, this symmetry breaking has been reported previously and is believed to be due to differential screening of 3d orbitals located on the Ga atoms (Plucinski et al. (2003)). The differences between the 6 layer and 100 layer constant energy slices are very minimal. The primary difference in the intensity is due to the planar size difference of the flakes, allowing for the collection of electrons from a larger area in the 100 layer sample.

To properly understand the differences in the valence band structure of the two flakes, the constant energy slices must be stacked and then sections taken along the high-symmetry directions. This data is shown in Figure (6.10) for a wide field of view and over a wide energy range of up to nearly 5 eV below the Fermi level alongside the corresponding UPS data. The first thing to note is the origin of the peaks in the UPS data located at -3.57 eV and -2.07 eV in the 100 layer sample and at -3.77 eV and -2.17 eV in the 6 layer sample. These peaks are the same as those previously recorded in the wide energy range UPS (Figure (6.7a)) where the deeper of these peaks was attributed to the mixing of the Ga 4p and Se 4s states.

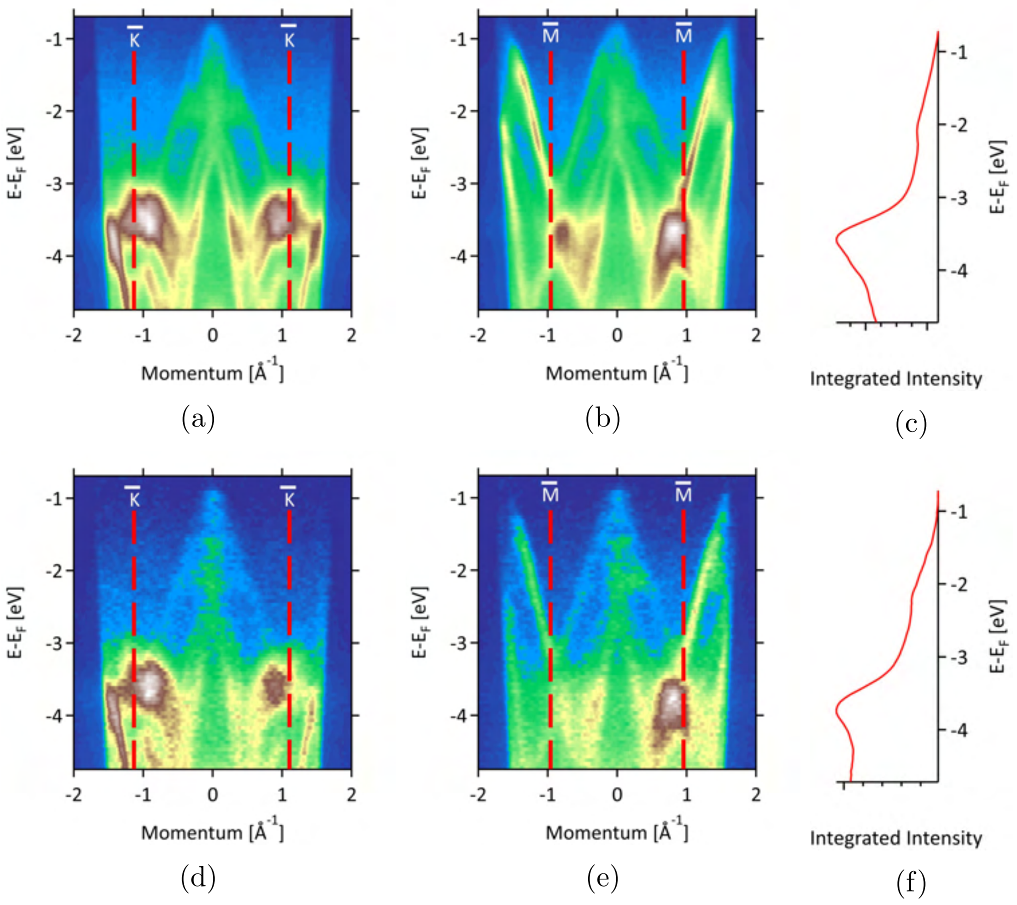

(a) (b) (c)

(d) (e) (f)

Figure 6.10: ARPES maps of the valence band dispersion of the 100 layer thick GaSe sample along the (a) $\bar{K}\bar{\Gamma}\bar{K}$' and (b) $\bar{M}\bar{\Gamma}\bar{M}$' directions. (c) UPS spectra gathered from the central ±1 Å^{-1} regions of (a) and (b). ARPES maps of the valence band dispersion of the 6 layer thick GaSe sample along the (d) $\bar{K}\bar{\Gamma}\bar{K}$' and (e) $\bar{M}\bar{\Gamma}\bar{M}$' directions. (f) UPS spectra gathered from the central ±1 Å^{-1} regions of (d) and (e). The spectra were recorded with a stepsize of 50 meV and a 6.5 Å^{-1} field of view.

The positions of the peaks in the UPS spectra can be ascribed to features in the valence band by looking at the high symmetry sections of the valence band shown in Figure (6.10). The two prominent peaks in this range at -3.57 eV and -2.07 eV in 100 layer GaSe and at -3.77 eV and -2.17 eV in 6 layer GaSe are associated with band crossings and the associated state hybridisation. This hybridisation is responsible for a high density of sates at these points. In k-space the positions of these crossing points for the 100 layer sample are at ±0.91 Å^{-1} and ±0.82 Å^{-1} along the $\bar{K}\bar{\Gamma}\bar{K}$' and

$\bar{\mathrm{M}}\bar{\Gamma}\bar{\mathrm{M}}$’ directions, respectively. For the 6 layer sample the crossing points are at ±0.90 Å^{-1} and ±0.79 Å^{-1} along the $\bar{\mathrm{K}}\bar{\Gamma}\bar{\mathrm{K}}$’ and $\bar{\mathrm{M}}\bar{\Gamma}\bar{\mathrm{M}}$’ directions, respectively.

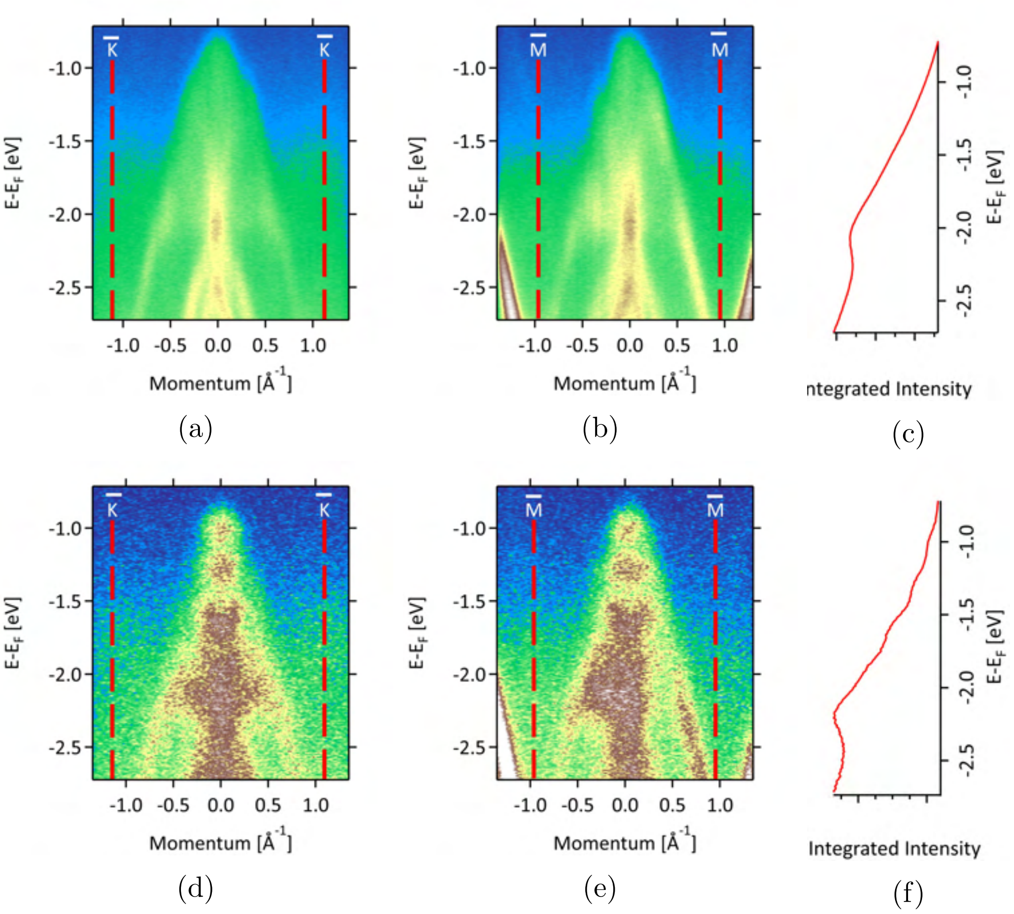

(a) (b) (c)

(d) (e) (f)

Figure 6.11: ARPES maps of the valence band dispersion of the 100 layer thick GaSe sample along the (a) $\bar{\mathrm{K}}\bar{\Gamma}\bar{\mathrm{K}}$’ and (b) $\bar{\mathrm{M}}\bar{\Gamma}\bar{\mathrm{M}}$’ directions. (c) UPS spectra gathered from the central ±1 Å^{-1} regions of (a) and (b). ARPES maps of the valence band dispersion of the 6 layer thick GaSe sample along the (d) $\bar{\mathrm{K}}\bar{\Gamma}\bar{\mathrm{K}}$’ and (e) $\bar{\mathrm{M}}\bar{\Gamma}\bar{\mathrm{M}}$’ directions. (f) UPS spectra gathered from the central ±1 Å^{-1} regions of (d) and (e). The spectra were recorded with a step size of 10 meV and a 2.7 Å^{-1} field of view.

By reducing the region of interest in ARPES to look only at those sates closer to the valence band maximum, more detail can be gathered. The resulting dispersions and reduced view UPS spectra are shown in Figure (6.11). Here, the valence maxima are at 0.78 eV and 0.91 eV below the Fermi level in the 100 layer and 6 layer flakes, respectively. By fitting a parabolic curve to the top of the valence band, the hole effective mass can be determined via the expression:

$$E(\mathbf{k}) = E_0 - \frac{\hbar^2\mathbf{k}^2}{2m^*}, \tag{6.2}$$

where $E(\mathbf{k})$ is the carrier energy at point $\mathbf{k}$ in the Brillouin zone, E_0 is the position of the valence band maximum, $\hbar$ is reduced Planck's constant and m^* is the hole effective mass. Using this expression, the hole effective mass in the 100 layer sample was found to be 1.2±0.4 m_e along both the $\bar{\mathrm{K}}\bar{\Gamma}\bar{\mathrm{K}}$' and $\bar{\mathrm{M}}\bar{\Gamma}\bar{\mathrm{M}}$' directions. Similarly, for the 6 layer sample, the hole effective mass is 1.1±0.4 m_e and 1.2±0.4 m_e along the $\bar{\mathrm{K}}\bar{\Gamma}\bar{\mathrm{K}}$' and $\bar{\mathrm{M}}\bar{\Gamma}\bar{\mathrm{M}}$' directions, respectively. The difference between the two samples is within the uncertainty of the measurement (±0.4 m_e), which is large owing to the inaccuracy inherent to directly fitting the ARPES spectrum. For a more accurate value, a more detailed study of the energy distribution curves should be made such that the band positions can be extracted for fitting. Both sets of carrier masses are above that but within the error range reported previously for pristine GaSe at $0.9m_e$, as determined via ARPES (Eremeev et al. (2020)).

Studying the UPS data in Figures (6.11c & 6.11f), a feature common to both samples can be seen at -2.08 eV and -2.19 eV in the 100 layer and 6 layer samples, respectively. This feature most likely corresponds to hybridisation of the Se p_x and p_y orbitals (Eremeev et al. (2020)) and was seen in the XPS valence band spectra at a binding energy of 1.94 eV (Figure (6.4a)). When moving closer to the valence band maxima, a difference between the 100 layer and 6 layer flakes can be observed with a series of 3 peaks present in the 6 layer sample but not in the 100 layer sample. These peaks are positioned at energies of -1.61 eV, -1.30 eV and -1.00 eV below the Fermi level. The dispersions in Figures (6.11d & 6.11e) reveal that they are centred at the Γ point. These roughly equally spaced levels in the 6 layer GaSe sample have not been reported in previous GaSe APRES band dispersion measurements (Ben Aziza et al. (2016); Eremeev et al. (2020); Aziza et al. (2018)). They likely represent band splitting as a result of quantum confinement in the layers, similar to previous results demonstrated in MoS_2 (Jin et al. (2013))

6.5 Summary

The modification of the valence band by water adsorption and water-induced oxidation of GaSe has been demonstrated. In-situ XPS measurements indicate a possible band bending of up to 0.27 eV due to the adsorbed water species. This band bending is partially reversed by illumination. The adsorbed water also modifies states deep within the valence band. These modifications are due to both adsorbed water and permanent water-induced oxidation of GaSe. As such, it is unavoidable in any solar water splitting application or any other moisture containing operating environment. The oxide is considered to partially manifests as a series of small oxide bumps on the exposed surface of GaSe. These bumps appear to grow to a thermodynamically favourable or diffusion rate limited size. The seed of the bumps is unknown, but observations via AFM may suggest surface defects as a possible cause. The ARPES measurements of bulk-like and 6 layer thick (partially oxidised) GaSe reveal some changes in the valence band structure when compared to pristine GaSe from the literature. Notably, these include a larger hole effective mass and the appearance of three high density of states features in 6 layer GaSe near the valence band maximum. It would be suspected that both of these features are relevant to the photovoltaic (carrier mass) and catalytic (new valence band states) activity of

GaSe when considered for solar water splitting.

To better understand the impact of oxidation on these properties, a further study of pristine GaSe would be desirable. The exchange of samples between the Nano-ESCA and NAP-XPS equipment under vacuum would allow for holistic studies on individual flakes. If combined with successful UPS work function measurements, this would allow for a full water splitting relevant description of the valence band of GaSe in response to water exposure.

Chapter 7

Summary, Open Questions & Outlook

This thesis explored a range of phenomena occurring when a vdW material is exposed to hydrogen. The exciting effects observed in hydrogen intercalated γ-InSe were presented; the formation of a SnS/SnS$_2$ heterostructure was demonstrated; likewise, the properties of partially oxidised ϵ-GaSe were examined in the context of solar water splitting. Here, the valence band structure and the effects of water-induced oxidation were observed. This chapter discusses the key results from chapters 4, 5 and 6, then describes currently unanswered questions before providing details of potential future work.

7.1 Summary of Results

The interactions investigated over the course of this PhD are relevant to the applications of hydrogen technologies and vdW materials modification. These results are discussed in their contexts for each of the materials systems below.

7.1.1 SnS/SnS_2

SnS_2 exhibited the most dramatic change upon exposure to H_2, with hydrogen acting to reduce SnS_2 to SnS and generate a SnS/SnS_2 heterostructure. The thickness of the heterosturcture is controllable and can be varied by altering the hydrogen exposure time. The cross-sectional TEM images of the heterostructure reveal a striking step-like interface between the SnS and SnS_2 regions. Furthermore, the basal planes of both materials are aligned and the generated SnS reveals continuous uninterrupted layers of high quality. This is unlike other similar methods of producing similar heterostructures, such as via argon plasma sputtering, which yields inclusions of SnS near the surface of SnS_2 and does not contain aligned basal layers (Kim et al. (2018)).

Thickness uniformity of the heterostructure across large distances was confirmed via Raman mapping measurements, with the ratio in the intensity of SnS to SnS_2 Raman peaks recorded over distances of several microns. The variation across regions of constant thickness was found to be less than 14 %, whilst discrepancies between regions of different thickness explained via an interference effect. The uniformity extended to the edges of the flakes. However, the XPS indicates a variation between flakes possibly due to residue left by the exfoliation process preventing conversion or by some unknown mechanism by which the conversion rate varies significantly between flakes.

The TEM and Raman results taken together provide compelling evidence for the ability of H_2 to readily reduce SnS_2 to SnS and produce a highly ordered heterostructre. Unlike alternative methods of producing such a structure, this method has fewer compromises when considering the trade-off between structural quality of the heterostructure and large area coverage. The heterostructure retained optical activity, as confirmed via PL mapping.

Under more reactive conditions (exposure to a proton beam or H_2 at > 250 °C), the further conversion of SnS to β-Sn was confirmed. The relative reactivity of hydrogen with SnS_2 under these more reactive conditions can be understood in terms of greater energy barrier to the conversion of SnS to β-Sn then for SnS_2 to SnS. By understanding this, the exposure of SnS_2 or SnS to different forms of hydrogen can be utilised to convert or etch the materials.

7.1.2 γ-InSe

γ-InSe behaves fundamentally differently to SnS_2 when exposed to both H_2 and H-ions. Instead of hydrogen accessing different crystal stoichiometries and atomic oxidation states, hydrogen acts to modify the γ-InSe crystal structure.

Exposure to a H-ion beam modifies γ-InSe. It is possible that this is caused by the bonding of hydrogen atoms to Se while retaining the crystal structure of γ-InSe. This process was confirmed via Raman spectroscopy, which revealed the modification of Raman modes qualitatively similar to theoretical predictions and consistent with an increased mass present on the Se atoms. However, it is worth noting the DFT underestimates the size of the change. The presence of the additional H-atom in the structure was found to suppress the PL signal of γ-InSe at room temperature. At low temperature (10 K) the presence of the H-atoms was found to increase the power density required to observe the onset of excitonic behaviours of γ-InSe. These two results point to hydrogen acting as a centre for non-radiative recombination in γ-InSe.

H_2 exposure of γ-InSe was performed for both powdered and bulk material. Bulk γ-InSe showed no measurable hydrogen uptake, whilst powdered γ-InSe recorded $\sim$0.2 wt.% uptake. This compares to reports of hydrogen uptake of up to 2.5 wt.% achieved electrochemically (Zhirko et al. (2007)). The gas phase uptake was found to be reversible on reducing the pressure of hydrogen in the chamber, making experimental studies of the exact nature of the incorporation difficult.

Theoretical results provided some insight to the mode of hydrogen incorporation from the gas phase. In particular, they reveal that hydrogen uptake is only favourable in γ-InSe when the vdW gap is increased by 2.5 Å or greater. This is due to the high interlayer electron density in the gap of γ-InSe owing to Se orbitals projecting into the interlayer space. In this configuration, the increased layer separation partially decouples the vdW layers and produces phonons with a more monolayer-like character. This offers an exciting method for modifying the vibrational and structural properties of γ-InSe.

7.1.3 ϵ-GaSe

ϵ-GaSe was investigated for its ability to act as a photocatalyst for solar water splitting. In particular, water exposed ϵ-GaSe becomes partially oxidised. This has been demonstrated previously (D'Olimpio et al. (2020)) and was confirmed here via NAP-XPS experiments. It is expected that the presence of oxide on the surface of ϵ-GaSe modifies its electronic band properties. This is significant as the band edge positions and band structure of a material are important factors in determining its suitability for solar water splitting.

NAP-XPS of ϵ-GaSe revealed the modification of the material via oxidation due to water exposure, with oxygen in the form of oxide and adsorbed water species observed in-situ. When illuminated via a solar simulator, the water concentration on the surface was found to decrease. A water induced band bending of up to 2.7 eV, within expectations, was also observed in the spectra. At the same time, a modification in the relative intensity of valence band states was observed. The oxide growth was also observed on the nano-scale with a series of consecutive AFM images documenting the growth of a surface oxide feature. The nature of this growth suggests defects on the surface of ϵ-GaSe as possibly initiating the oxidation process. Although the coverage of oxide bumps in AFM doesn't fully account for the oxide observed in XPS.

ARPES measurements confirmed the band dispersions of partially oxidised bulk-like and 6 layer thick ϵ-GaSe. The measured hole effective masses are higher than those reported for pristine ϵ-GaSe in the literature. Additionally, the presence of previously unreported states were observed near the valence band maximum of partially oxidised 6 layer ϵ-GaSe.

The results illustrate the modification of ϵ-GaSe by water exposure. The changes to the band structure of the material should be noted when considering ϵ-GaSe for solar water splitting applications and are relevant to other applications where the material might become oxidised.

7.2 Unanswered Questions

The detailed investigations described in this thesis have contributed to the the discovery of new phenomena of fundamental and technological interest. However, they have also raised some unanswered questions. These knowledge gaps are detailed here.

7.2.1 SnS/SnS_2

The formation of a SnS/SnS_2 heterostructure requires the permeation of hydrogen across SnS layers. However, the method of diffusion of H_2 within SnS/SnS_2 is currently unknown. If SnS and SnS_2 behave similarly to other vdW materials and are impermeable to hydrogen (Sun et al. (2020)), then the effect of grain boundaries, step-edges and defects might be important in this process. Understanding this would allow for the modification of material in such a way as to effect the rate at which SnS_2 is converted to SnS. Similarly, a better understanding of this rate would allow for devices of accurate and predictable dimensions to be produced.

The SnS/SnS_2 heterostructure produced via an interaction with hydrogen should form a *p*-*n* junction. This junction should then be able to demonstrate both current rectification and photovoltaic behaviours. However, attempts to date have failed to probe the electrical properties of such a junction. This is due to the inability to utilise polydimethylsiloxane (PDMS) to position the initial SnS_2 flake on a set of contacts. This is because it inhibits the interaction between hydrogen and SnS_2. As such, a PDMS free approach to producing a device must be sought such that the electronic properties of the junction can be evaluated.

Finally, it is currently not known if there is a preferential orientation for which the SnS aligns with SnS_2. Knowing this would be beneficial for understanding processes at the interface and the prediction of any twistronic properties.

7.2.2 γ-InSe

Powdered γ-InSe showed some hydrogen uptake when exposed to gas phase H_2. However, once the hydrogen pressure is reduced, the hydrogen uptake is reversed. In-situ measurements would be valuable here to understand the nature of the hydrogen incorporation. In-particular, to assess how the uptake compares to theoretical results predicting the increased interlayer separation and the effect that has on the phonon modes of γ-InSe.

7.2.3 ϵ-GaSe

The ϵ-GaSe experiments have thus far been limited by inability to confidently measure the band structure of unoxidised pristine ϵ-GaSe. Measurement of the same sample of GaSe before and after oxidation is important in confirming that the observed features are due to oxidation and not a batch related issue. This would also allow for the study of how a different oxide loadings on the surface of ϵ-GaSe effects any changes.

7.3 Prospects and Outlook

The currently open questions surrounding the materials and their interactions are of importance both fundamentally and to their future application. Here, are described potential future experiments answering these questions.

The facilities of the Nano-ESCA allow for the observation of the reciprocal space electronic dispersion of a material. As this retains angular information, by a comparison of constant energy slices before and after exposure to hydrogen, the relative orientation of SnS_2 and SnS layers can be determined. This is dependent on the material quality and the ability to avoid surface contamination. Utilising a NAP-XPS system, the exposure to H_2 can be monitored in-situ, and via the use of a solar simulator the open circuit voltage of the heterostructure determined, confirming the presence of a p-n junction.

The epitaxial growth and in-situ analysis of 2-dimensional semiconductors (EPI2SEM) combines the processes of molecular beam epitaxy (MBE), scanning probe microscopy (SPM) and ARPES via a vacuum system. This allows for the utilisation of these three systems without the exposure of a sample to air. ϵ-GaSe produced via MBE in this system can therefore be guaranteed oxygen free. This allows for the measurement of the valence band dispersion of pristine ϵ-GaSe. Features of partially oxidised ϵ-GaSe can then be accurately attributed to the presence of oxide.

A hydrogen cell for the in-situ measurement of electronic properties is currently under construction. This equipment will allow for the measurement of the electronic properties of any vdW material whilst exposed to hydrogen. As such, it can asses some of the change to γ-InSe under hydrogen exposure and monitor the interactions between H_2 and SnS_2.

7.4 Conclusions

Over the course of this PhD the properties and interactions of materials for various hydrogen related applications have been investigated. This includes the production of a SnS/SnS_2 heterostructure by hydrogen, the experimental and theoretical modification of the vibrational properties of γ-InSe by hydrogen, and the changing valence band structure of ϵ-GaSe by water-induced oxidation. Often surprising in their phenomenology, these interactions should prove useful to the further design of hydrogen technologies or to those looking for a means to modify the properties of vdW materials. Most importantly, the unexpected nature of many of the interactions lends credibility to the notion that the fundamental properties of the interactions between vdW materials and hydrogen should be extended to include the full diverse range of vdW materials.

Bibliography

Abay, B., Efeoğlu, H., and Yoğurtçu, Y. (1998). Low-temperature photoluminescence of n-InSe layer semiconductor crystals. *Materials Research Bulletin*, 33(9):1401–1410.

Abd Mutalib, M., Rahman, M., Othman, M., Ismail, A., and Jaafar, J. (2017). Scanning electron microscopy (sem) and energy-dispersive x-ray (edx) spectroscopy. In *Membrane characterization*, pages 161–179. Elsevier.

Akhtar, K., Khan, S. A., Khan, S. B., and Asiri, A. M. (2018). Scanning electron microscopy: Principle and applications in nanomaterials characterization. *Handbook of materials characterization*, pages 113–145.

Alekseeva, O., Pushkareva, I., Pushkarev, A., and Fateev, V. (2020). Graphene and graphene-like materials for hydrogen energy. *Nanotechnologies in Russia*, 15(3):273–300.

An, Y., Kuc, A., Petkov, P., Lozada-Hidalgo, M., and Heine, T. (2019). On the Chemistry and Diffusion of Hydrogen in the Interstitial Space of Layered Crystals h-BN, MoS_2, and Graphite. *Small*, 15(43):1901722.

Arellano, J., Molina, L., Rubio, A., and Alonso, J. (2000). Density functional study of adsorption of molecular hydrogen on graphene layers. *The Journal of Chemical Physics*, 112(18):8114–8119.

Arutyunyan, N., Rybkovskiy, D., Obraztsova, E., and Obraztsova, E. (2022). Size-induced evolution of optical properties in gallium selenide thin layers. *Journal of Luminescence*, 242:118546.

Atkins, P., Atkins, P. W., and de Paula, J. (2014). *Atkins' Physical Chemistry*. Oxford University Press.

Aziza, Z. B., Zólyomi, V., Henck, H., Pierucci, D., Silly, M. G., Avila, J., Magorrian, S. J., Chaste, J., Chen, C., Yoon, M., et al. (2018). Valence band inversion and spin-orbit effects in the electronic structure of monolayer GaSe. *Physical Review B*, 98(11):115405.

Badwal, S. P., Giddey, S. S., Munnings, C., Bhatt, A. I., and Hollenkamp, A. F. (2014). Emerging electrochemical energy conversion and storage technologies. *Frontiers in Chemistry*, 2:79.

Balakrishnan, N., Kudrynskyi, Z. R., Fay, M. W., Mudd, G. W., Svatek, S. A., Makarovsky, O., Kovalyuk, Z. D., Eaves, L., Beton, P. H., and Patanè, A. (2014). Room temperature electroluminescence from mechanically formed van der waals iii–vi homojunctions and heterojunctions. *Advanced Optical Materials*, 2(11):1064–1069.

Balakrishnan, N., Kudrynskyi, Z. R., Smith, E. F., Fay, M. W., Makarovsky, O., Kovalyuk, Z. D., Eaves, L., Beton, P. H., and Patanè, A. (2017). Engineering *p*-*n* junctions and bandgap tuning of InSe nanolayers by controlled oxidation. *2D Materials*, 4(2):025043.

Balandin, A. A. (2011). Thermal properties of graphene and nanostructured carbon materials. *Nature Materials*, 10(8):569–581.

Bauer, N. and Beach, J. (1947). Differences in Mass Spectra of H_2 and D_2. *The Journal of Chemical Physics*, 15(3):150–151.

Ben Aziza, Z., Henck, H., Pierucci, D., Silly, M. G., Lhuillier, E., Patriarche, G., Sirotti, F., Eddrief, M., and Ouerghi, A. (2016). van der Waals epitaxy of GaSe/graphene heterostructure: electronic and interfacial properties. *ACS Nano*, 10(10):9679–9686.

Bernardi, M., Ataca, C., Palummo, M., and Grossman, J. C. (2017). Optical and electronic properties of two-dimensional layered materials. *Nanophotonics*, 6(2):479–493.

Blackstone, C. and Ignaszak, A. (2021). Van der Waals Heterostructures—Recent Progress in Electrode Materials for Clean Energy Applications. *Materials*, 14(13):3754.

Boledzyuk, V., Zaslonkin, A., Kovalyuk, Z., and Pyrlya, M. (2011). Electrical properties of In_2Se_3 intercalated layered crystals. *Ukrainian Journal of Physics*, 56(4):376–380.

Brenner, D. W., Shenderova, O. A., Harrison, J. A., Stuart, S. J., Ni, B., and Sinnott, S. B. (2002). A second-generation reactive empirical bond order (REBO) potential energy expression for hydrocarbons. *Journal of Physics: Condensed Matter*, 14(4):783.

Brodie, B. C. (1859). XIII. On the atomic weight of graphite. *Philosophical transactions of the Royal Society of London*, 149:249–259.

Brudnyi, V. N., Sarkisov, S. Y., and Kosobutsky, A. V. (2015). Electronic properties of GaSe, InSe, GaS and GaTe layered semiconductors: charge neutrality level and interface barrier heights. *Semiconductor Science and Technology*, 30(11):115019.

Bunch, J. S., Verbridge, S. S., Alden, J. S., Van Der Zande, A. M., Parpia, J. M., Craighead, H. G., and McEuen, P. L. (2008). Impermeable atomic membranes from graphene sheets. *Nano Letters*, 8(8):2458–2462.

Burton, L. A. and Walsh, A. (2012). Phase stability of the earth-abundant tin sulfides SnS, SnS_2, and Sn_2S_3. *The Journal of Physical Chemistry C*, 116(45):24262–24267.

Burton, L. A., Whittles, T. J., Hesp, D., Linhart, W. M., Skelton, J. M., Hou, B., Webster, R. F., O'Dowd, G., Reece, C., Cherns, D., et al. (2016). Electronic and optical properties of single crystal SnS_2: an earth-abundant disulfide photocatalyst. *Journal of Materials Chemistry A*, 4(4):1312–1318.

Buttner, W. J., Burgess, R. M., Schmidt, K., Hartmann, K. S., Wright, H., Weidner, E., Cebolla, R. O., Bonato, C., and Moretto, P. (2017). Hydrogen safety sensor performance and use gap analysis. Technical report, National Renewable Energy Lab. (NREL).

Cavendish, H. (1766). XIX. Three papers, containing experiments on factitious air. *Philosophical Transactions of the Royal Society of London*, 56:141–184.

Chang, K., Lahn, S., and Chang, J. (2006). Growth of single-phase In_2Se_3 by using metal organic chemical vapor deposition with dual-source precursors. *Applied Physics Letters*, 89(18):182118.

Change, I. C. (2014). Synthesis Report: Contribution of working groups I. II and III to the Fifth Assessment Report. *Proceedings of the Intergovernmental Panel on Climate Change, Copenhagen, Denmark*, pages 1–167.

Chattopadhyay, T., Pannetier, J., and Von Schnering, H. (1986). Neutron diffraction study of the structural phase transition in SnS and SnSe. *Journal of Physics and Chemistry of Solids*, 47(9):879–885.

Chen, C., Chen, X., Shao, Y., Deng, B., Guo, Q., Ma, C., and Xia, F. (2018a). Valley-selective linear dichroism in layered tin sulfide. *ACS Photonics*, 5(9):3814–3819.

Chen, M.-W., Kim, H., Ovchinnikov, D., Kuc, A., Heine, T., Renault, O., and Kis, A. (2018b). Large-grain MBE-grown GaSe on GaAs with a Mexican hat-like valence band dispersion. *npj 2D Materials and Applications*, 2(1):1–7.

Cheng, H.-M., Yang, Q.-H., and Liu, C. (2001). Hydrogen storage in carbon nanotubes. *Carbon*, 39(10):1447–1454.

Cheng, W.-H., Richter, M. H., May, M. M., Ohlmann, J., Lackner, D., Dimroth, F., Hannappel, T., Atwater, H. A., and Lewerenz, H.-J. (2018). Monolithic photoelectrochemical device for direct water splitting with 19% efficiency. *ACS Energy Letters*, 3(8):1795–1800.

Chusuei, C. and Goodman, D. (2013). *Reference Module in Chemistry, Molecular Sciences and Chemical Engineering*. Elsevier.

Dalla Valle, P. and Cavassilas, N. (2022). A van der Waals heterojunction based on monolayers of MoS_2 and WSe_2 for overall solar water splitting. *Nanoscale Advances*.

Damascelli, A. (2004). Probing the electronic structure of complex systems by arpes. *Physica Scripta*, 2004(T109):61.

David, B. (2020). Ammonia: zero-carbon fertiliser, fuel and energy store. Technical report, The Royal Society.

DeGregorio, Z. P., Myers, J. C., and Campbell, S. A. (2020). Rational control of WSe_2 layer number via hydrogen-controlled chemical vapor deposition. *Nanotechnology*, 31(31):315604.

Deng, S., Sumant, A. V., and Berry, V. (2018). Strain engineering in two-dimensional nanomaterials beyond graphene. *Nano Today*, 22:14–35.

Derkachova, A., Kolwas, K., and Demchenko, I. (2016). Dielectric function for gold in plasmonics applications: size dependence of plasmon resonance frequencies and damping rates for nanospheres. *Plasmonics*, 11:941–951.

Diachenko, O. V., Dobrozhan, O. A., Opanasiuk, A. S., Kurbatov, D. I., Hrynenko, V. V., and Plotnikov, S. (2019). Efficiency modeling of solar cells based on the n-zn1-xmgxo/p-sns heterojunction.

Ding, Y., Zheng, W., Lu, X., Liang, Y., Zhu, Y., Jin, M., and Huang, F. (2020). Raman tensor of layered SnS_2. *The Journal of Physical Chemistry Letters*, 11(23):10094–10099.

DOE (2016). *Hydrogen and Fuel Cell Technologies Office Multi-Year Research, Development, and Demonstration Plan.* Department of Energy (DOE).

D'Olimpio, G., Nappini, S., Vorokhta, M., Lozzi, L., Genuzio, F., Menteş, T. O., Paolucci, V., Gürbulak, B., Duman, S., Ottaviano, L., et al. (2020). Enhanced electrocatalytic activity in GaSe and InSe nanosheets: the role of surface oxides. *Advanced Functional Materials*, 30(43):2005466.

Eastman, D. and Grobman, W. (1972). Photoemission energy distributions for au from 10 to 40 eV using synchrotron radiation. *Physical Review Letters*, 28(20):1327.

Egerton, R. F. et al. (2005). *Physical principles of electron microscopy*, volume 56. Springer.

Eidsvåg, H., Bentouba, S., Vajeeston, P., Yohi, S., and Velauthapillai, D. (2021). TiO_2 as a photocatalyst for water splitting—An experimental and theoretical review. *Molecules*, 26(6):1687.

El-Shafie, M., Kambara, S., and Hayakawa, Y. (2019). Hydrogen Production Technologies Overview. *Journal of Power and Energy Engineering*, 07(01):107–154.

Elliott, S. (1998). *The Physics and Chemistry of Solids*. Wiley.

Eremeev, S., Papagno, M., Grimaldi, I., De Luca, O., Ferrari, L., Kundu, A. K., Sheverdyaeva, P., Moras, P., Avvisati, G., Crepaldi, A., et al. (2020). Insight into the electronic structure of semiconducting ϵ- GaSe and ϵ- InSe. *Physical Review Materials*, 4(8):084603.

Ermolaev, G. A., Yakubovsky, D. I., El-Sayed, M. A., Tatmyshevskiy, M. K., Mazitov, A. B., Popkova, A. A., Antropov, I. M., Bessonov, V. O., Slavich, A. S., Tselikov, G. I., et al. (2021). Broadband optical constants and nonlinear properties of sns2 and snse2. *Nanomaterials*, 12(1):141.

Felton, J., Blundo, E., Kudrynskyi, Z., Ling, S., Bradford, J., Pettinari, G., Cooper, T., Wadge, M., Kovalyuk, Z., Polimeni, A., et al. (2022). Hydrogen-Induced Conversion of SnS_2 into SnS or Sn: A Route to Create SnS_2/SnS Heterostructures. *Small*, page 2202661.

Felton, J., Blundo, E., Ling, S., Glover, J., Kudrynskyi, Z. R., Makarovsky, O., Kovalyuk, Z. D., Besley, E., Walker, G., Polimeni, A., et al. (2020). The Interaction of Hydrogen with the van der Waals Crystal γ-InSe. *Molecules*, 25(11):2526.

Ferrer-Roca, C., Bouvier, J., Segura, A., Andrés, M. V., and Muñoz, V. (1999). Light-induced transmission nonlinearities in gallium selenide. *Journal of Applied Physics*, 85(7):3780–3785.

Fu, C.-F., Zhang, R., Luo, Q., Li, X., and Yang, J. (2019). Construction of direct Z-Scheme photocatalysts for overall water splitting using two-dimensional van der waals heterojunctions of metal dichalcogenides. *Journal of Computational Chemistry*, 40(9):980–987.

Fujishima, A. and Honda, K. (1972). Electrochemical photolysis of water at a semiconductor electrode. *Nature*, 238(5358):37–38.

Gao, L. (2017). Flexible device applications of 2D semiconductors. *Small*, 13(35):1603994.

Gelius, U., Asplund, L., Basilier, E., Hedman, S., Helenelund, K., and Siegbahn, K. (1984). A high resolution multipurpose ESCA instrument with X-ray monochromator. *Nuclear Instruments and Methods in Physics Research Section B: Beam Interactions with Materials and Atoms*, 1(1):85–117.

Gong, Y., Yuan, H., Wu, C.-L., Tang, P., Yang, S.-Z., Yang, A., Li, G., Liu, B., van de Groep, J., Brongersma, M. L., et al. (2018). Spatially controlled doping of two-dimensional SnS_2 through intercalation for electronics. *Nature Nanotechnology*, 13(4):294–299.

Gonzalez, J. M. and Oleynik, I. I. (2016). Layer-dependent properties of SnS_2 and $SnSe_2$ two-dimensional materials. *Physical Review B*, 94(12):125443.

Goodwin, R. D., Diller, D. E., Roder, H. M., and Weber, L. A. (1964). Second and third virial coefficients for hydrogen. *Physics and Chemistry*, 68(1):121–126.

Grånäs, E., Gerber, T., Schröder, U. A., Schulte, K., Andersen, J. N., Michely, T., and Knudsen, J. (2016). Hydrogen intercalation under graphene on Ir(111). *Surface Science*, 651:57–61.

Gulbransen, E. A., Andrew, K. F., and Brassart, F. A. (1965). The reaction of hydrogen with graphite at 1200° to 1650 °C. *Journal of the Electrochemical Society*, 112(1):49.

Guo, Y., Xu, K., Wu, C., Zhao, J., and Xie, Y. (2015). Surface chemical-modification for engineering the intrinsic physical properties of inorganic two-dimensional nanomaterials. *Chemical Society Reviews*, 44(3):637–646.

Halpern, J. and Lax, B. (1965). Magnetoabsorption of the indirect transition in germanium. *Journal of Physics and Chemistry of Solids*, 26(5):911–919.

Harrison, N. (2003). An Introduction to Density Functional Theory. *Computational materials science*, 187:45.

Hassan, S., Asghar, M., et al. (2010). Limitation of silicon based computation and future prospects. In *2010 Second International Conference on Communication Software and Networks*, pages 559–561. IEEE.

Herzberg, G. and Monfils, A. (1961). The dissociation energies of the H_2, HD, and D_2 molecules. *Journal of Molecular Spectroscopy*, 5(1-6):482–498.

Hohenberg, P. and Kohn, W. (1964). Inhomogeneous electron gas. *Physical review*, 136(3B):B864.

Hong, Y. K., Liu, N., Yin, D., Hong, S., Kim, D. H., Kim, S., Choi, W., and Yoon, Y. (2017). Recent progress in high-mobility thin-film transistors based on multilayer 2D materials. *Journal of Physics D: Applied Physics*, 50(16):164001.

Hu, S., Gopinadhan, K., Rakowski, A., Neek-Amal, M., Heine, T., Grigorieva, I., Haigh, S., Peeters, F., Geim, A., and Lozada-Hidalgo, M. (2018). Transport of hydrogen isotopes through interlayer spacing in van der Waals crystals. *Nature Nanotechnology*, 13(6):468–472.

Hu, S., Lozada-Hidalgo, M., Wang, F., Mishchenko, A., Schedin, F., Nair, R. R., Hill, E., Boukhvalov, D., Katsnelson, M., Dryfe, R. A., et al. (2014). Proton transport through one-atom-thick crystals. *Nature*, 516(7530):227–230.

IEA (2019). The Future of Hydrogen for G20. Technical Report June, International Energy Agency (IEA).

Ismail, A. F., Khulbe, K. C., and Matsuura, T. (2015). Gas separation membranes. *Switz. Springer*, 10:973–978.

Jiang, C., Moniz, S. J., Wang, A., Zhang, T., and Tang, J. (2017). Photoelectrochemical devices for solar water splitting-materials and challenges. *Chemical Society Reviews*, 46(15):4645–4660.

Jin, W., Yeh, P.-C., Zaki, N., Zhang, D., Sadowski, J. T., Al-Mahboob, A., van Der Zande, A. M., Chenet, D. A., Dadap, J. I., Herman, I. P., et al. (2013). Direct measurement of the thickness-dependent electronic band structure of mos 2 using angle-resolved photoemission spectroscopy. *Physical review letters*, 111(10):106801.

Johnson, D., Hilal, N., and Bowen, W. R. (2009). Basic principles of atomic force microscopy. In *Atomic force microscopy in process engineering: an introduction to AFM for improved processes and products*, pages 1–30. Elsevier.

Juodkazytė, J., Seniutinas, G., Šebeka, B., Savickaja, I., Malinauskas, T., Badokas, K., Juodkazis, K., and Juodkazis, S. (2016). Solar water splitting: efficiency discussion. *International Journal of Hydrogen Energy*, 41(28):11941–11948.

Kaminskii, V., Kovalyuk, Z., Netyaga, V., and Boledzyuk, V. (2007). Dielectric characteristics of GaSe nanocrystals intercalated with hydrogen. *Semiconductor Physics Quantum Electronics & Optoelectronics*.

Kaminskii, V., Kovalyuk, Z., Pyrlya, M., Gavrilyuk, S., and Netyaga, V. (2005). Properties of hydrogenated GaSe crystals. *Inorganic Materials*, 41(8):793–795.

Kang, S., Lee, D., Kim, J., Capasso, A., Kang, H. S., Park, J.-W., Lee, C.-H., and Lee, G.-H. (2020). 2D semiconducting materials for electronic and optoelectronic applications: potential and challenge. *2D Materials*, 7(2):022003.

Kaufman, H. R. (1961). An Ion Rocket with an Electron-Bombardment Ion Source. Technical report, National Aeronautics and Space Administration (NASA).

Kim, J. H., Yun, S. J., Lee, H. S., Zhao, J., Bouzid, H., and Lee, Y. H. (2018). Plasma-induced phase transformation of SnS_2 to SnS. *Scientific Reports*, 8(1):1–7.

Kim, T. H., Bae, J., Lee, T. H., Hwang, J., Jung, J. H., Kim, D. K., Lee, J. S., Kim, D. O., Lee, Y. H., and Ihm, J. (2016). Room-temperature hydrogen storage via two-dimensional potential well in mesoporous graphene oxide. *Nano Energy*, 27:402–411.

Klingshirn, C. F. (2012). *Semiconductor Optics*. Springer Science & Business Media.

Kudrynskyi, Z. R., Wang, X., Sutcliffe, J., Bhuiyan, M. A., Fu, Y., Yang, Z., Makarovsky, O., Eaves, L., Solomon, A., Maslyuk, V. T., et al. (2020). Van der Waals $SnSe_{2(1-x)}S_{2x}$ Alloys: Composition-Dependent Bowing Coefficient and Electron–Phonon Interaction. *Advanced Functional Materials*, 30(9):1908092.

Kumagai, Y., Burton, L. A., Walsh, A., and Oba, F. (2016). Electronic structure and defect physics of tin sulfides: SnS, Sn_2S_3, and SnS_2. *Physical Review Applied*, 6(1):014009.

Kumar, P., Singh, S., Hashmi, S., and Kim, K.-H. (2021). MXenes: Emerging 2D materials for hydrogen storage. *Nano Energy*, 85:105989.

Lang, O., Pettenkofer, C., Sánchez-Royo, J. F., Segura, A., Klein, A., and Jaegermann, W. (1999). Thin film growth and band lineup of In_2O_3 on the layered semiconductor InSe. *Journal of Applied Physics*, 86(10):5687–5691.

Laursen, A. B., Varela, A. S., Dionigi, F., Fanchiu, H., Miller, C., Trinhammer, O. L., Rossmeisl, J., and Dahl, S. (2012). Electrochemical hydrogen evolution: Sabatier's principle and the volcano plot. *Journal of Chemical Education*, 89(12):1595–1599.

Le, T. N.-M., Chiu, C.-c., and Kuo, J.-L. (2020). From the perspectives of DFT calculations, thermodynamic modeling, and kinetic Monte Carlo simulations: the interaction between hydrogen and Sc_2C monolayers. *Physical Chemistry Chemical Physics*, 22(8):4387–4401.

Lee, C., Wei, X., Kysar, J. W., and Hone, J. (2008). Measurement of the elastic properties and intrinsic strength of monolayer graphene. *Science*, 321(5887):385–388.

Leitch, A., Alex, V., and Weber, J. (1998). Raman spectroscopy of hydrogen molecules in crystalline silicon. *Physical Review Letters*, 81(2):421.

Levi, P., Vass, T., Mandová, H., and Gouy, A. (2020). Tracking Industry 2020. Technical report, IEA: International Energy Agency.

Li, M., Wu, Y., Li, T., Chen, Y., Ding, H., Lin, Y., Pan, N., and Wang, X. (2017a). Revealing anisotropy and thickness dependence of Raman spectra for SnS flakes. *RSC Advances*, 7(77):48759–48765.

Li, M., Zhu, Y., Li, T., Lin, Y., Cai, H., Li, S., Ding, H., Pan, N., and Wang, X. (2018). One-step CVD fabrication and optoelectronic properties of SnS_2/SnS vertical heterostructures. *Inorganic Chemistry Frontiers*, 5(8):1828–1835.

Li, S., Wang, Y., Cheng, P., Feng, B., Chen, L., and Wu, K. (2021). Realization of Large Scale, 2D van der Waals Heterojunction of SnS_2/SnS by Reversible Sulfurization. *Small*, 17(37):2101154.

Li, W., Poncé, S., and Giustino, F. (2019). Dimensional crossover in the carrier mobility of two-dimensional semiconductors: the case of InSe. *Nano Letters*, 19(3):1774–1781.

Li, X., Li, X., Zang, X., Zhu, M., He, Y., Wang, K., Xie, D., and Zhu, H. (2015). Role of hydrogen in the chemical vapor deposition growth of MoS_2 atomic layers. *Nanoscale*, 7(18):8398–8404.

Li, Y., Li, Y.-L., Sa, B., and Ahuja, R. (2017b). Review of two-dimensional materials for photocatalytic water splitting from a theoretical perspective. *Catalysis Science & Technology*, 7(3):545–559.

Lin, S., Carvalho, A., Yan, S., Li, R., Kim, S., Rodin, A., Carvalho, L., Chan, E. M., Wang, X., Castro Neto, A. H., et al. (2018). Accessing valley degree of freedom in bulk Tin (II) sulfide at room temperature. *Nature Communications*, 9(1):1–7.

Lipson, A., Lipson, S. G., and Lipson, H. (2010). *Optical physics*. Cambridge University Press.

Liu, Y., Pharr, M., and Salvatore, G. A. (2017). Lab-on-skin: a review of flexible and stretchable electronics for wearable health monitoring. *ACS Nano*, 11(10):9614–9635.

Lozada-Hidalgo, M., Hu, S., Marshall, O., Mishchenko, A., Grigorenko, A., Dryfe, R., Radha, B., Grigorieva, I., and Geim, A. (2016). Sieving hydrogen isotopes through two-dimensional crystals. *Science*, 351(6268):68–70.

Madelung, O., Rössler, U., and Schulz, M. (1998). IV-VI2compounds, general tables crystal structure, lattice parameters, chemical bond of SnS_2, $SnSe_2$, $SnS_{(x)}Se_{(2-x)}$: Datasheet. *Landolt-Börnstein - Group III Condensed Matter*, 41C:1–3.

Mead, D. and Irwin, J. (1976). Raman spectra of SnS_2 and $SnSe_2$. *Solid State Communications*, 20(9):885–887.

Meng, J., Wang, J., Wang, J., Li, Q., and Yang, J. (2022). β-SnS/GaSe heterostructure: a promising solar-driven photocatalyst with low carrier recombination for overall water splitting. *Journal of Materials Chemistry A*, 10(7):3443–3453.

Miró, P., Audiffred, M., and Heine, T. (2014). An atlas of two-dimensional materials. *Chemical Society Reviews*, 43(18):6537–6554.

Mitsuhashi, T., Minohara, M., Yukawa, R., Kitamura, M., Horiba, K., Kobayashi, M., and Kumigashira, H. (2016). Influence of k broadening on arpes spectra of the (110) and (001) surfaces of srvo 3 films. *Physical Review B*, 94(12):125148.

Mohr, M., Maultzsch, J., Dobardžić, E., Reich, S., Milošević, I., Damnjanović, M., Bosak, A., Krisch, M., and Thomsen, C. (2007). Phonon dispersion of graphite by inelastic x-ray scattering. *Physical Review B*, 76(3):035439.

Molas, M. R., Tyurnina, A. V., Zólyomi, V., Ott, A. K., Terry, D. J., Hamer, M. J., Yelgel, C., Babiński, A., Nasibulin, A. G., Ferrari, A. C., et al. (2021). Raman spectroscopy of GaSe and InSe post-transition metal chalcogenides layers. *Faraday Discussions*, 227:163–170.

Moulder, J. F., Stickle, W., Sobol, P., and Bomben, K. (1992). Handbook of X-ray Photoelectron Spectroscopy: Physical Electronics Division. *Perkin-Elmer Corporation, Eden Prairie, MN, USA*.

Nakayama, M., Hirao, T., and Hasegawa, T. (2010). Photoluminescence properties of exciton-exciton scattering in a GaAs/AlAs multiple quantum well. *Physica E: Low-dimensional Systems and Nanostructures*, 42(10):2644–2647.

Naumis, G. G., Barraza-Lopez, S., Oliva-Leyva, M., and Terrones, H. (2017). Electronic and optical properties of strained graphene and other strained 2D materials: a review. *Reports on Progress in Physics*, 80(9):096501.

Ng, B.-J., Putri, L. K., Kong, X. Y., Teh, Y. W., Pasbakhsh, P., and Chai, S.-P. (2020). Z-scheme photocatalytic systems for solar water splitting. *Advanced Science*, 7(7):1903171.

Novoselov, K. S., Geim, A. K., Morozov, S. V., Jiang, D.-e., Zhang, Y., Dubonos, S. V., Grigorieva, I. V., and Firsov, A. A. (2004). Electric field effect in atomically thin carbon films. *Science*, 306(5696):666–669.

Pallecchi, E., Lafont, F., Cavaliere, V., Schopfer, F., Mailly, D., Poirier, W., and Ouerghi, A. (2014). High Electron Mobility in Epitaxial Graphene on 4H-SiC(0001) via post-growth annealing under hydrogen. *Scientific Reports*, 4(1):1–7.

Papon, R., Sharma, S., Shinde, S. M., Thangaraja, A., Kalita, G., and Tanemura, M. (2015). Formation of graphene nanoribbons and Y-junctions by hydrogen induced anisotropic etching. *RSC Advances*, 5(44):35297–35301.

Peramanu, S., Cox, B., and Pruden, B. (1999). Economics of hydrogen recovery processes for the purification of hydroprocessor purge and off-gases. *International Journal of Hydrogen Energy*, 24(5):405–424.

Pierucci, D., Henck, H., Ben Aziza, Z., Naylor, C. H., Balan, A., Rault, J. E., Silly, M. G., Dappe, Y. J., Bertran, F., Le Fèvre, P., et al. (2017). Tunable doping in hydrogenated single layered molybdenum disulfide. *ACS Nano*, 11(2):1755–1761.

Plucinski, L., Johnson, R., Kowalski, B., Kopalko, K., Orlowski, B., Kovalyuk, Z., and Lashkarev, G. (2003). Electronic band structure of GaSe(0001): Angle-resolved photoemission and ab initio theory. *Physical Review B*, 68(12):125304.

Popov, I. V., Görne, A. L., Tchougréeff, A. L., and Dronskowski, R. (2019). Relative stability of diamond and graphite as seen through bonds and hybridizations. *Physical Chemistry Chemical Physics*, 21(21):10961–10969.

Ramirez-Vidal, P., Canevesi, R. L., Sdanghi, G., Schaefer, S., Maranzana, G., Celzard, A., and Fierro, V. (2021). A step forward in understanding the hydrogen adsorption and compression on activated carbons. *ACS Applied Materials & Interfaces*, 13(10):12562–12574.

Reddy, V. R. M., Gedi, S., Park, C., Miles, R., and KT, R. R. (2015). Development of sulphurized SnS thin film solar cells. *Current Applied Physics*, 15(5):588–598.

Richardson, D. (1977). A calculation of van der Waals interactions in and between layers of atoms: application to graphite. *Journal of Physics C: Solid State Physics*, 10(17):3235.

Roth, L. M., Lax, B., and Zwerdling, S. (1959). Theory of optical magneto-absorption effects in semiconductors. *Physical Review*, 114(1):90.

Rushchanskii, K. (2004). The influence of hydrostatic pressure on the static and dynamic properties of an InSe crystal: A first-principles study. *Physics of the Solid State*, 46(1):179–187.

Rybkovskiy, D., Arutyunyan, N., Orekhov, A., Gromchenko, I., Vorobiev, I., Osadchy, A., Salaev, E. Y., Baykara, T., Allakhverdiev, K., and Obraztsova, E. (2011). Size-induced effects in gallium selenide electronic structure: The influence of interlayer interactions. *Physical Review B*, 84(8):085314.

Ryu, S., Han, M. Y., Maultzsch, J., Heinz, T. F., Kim, P., Steigerwald, M. L., and Brus, L. E. (2008). Reversible basal plane hydrogenation of graphene. *Nano letters*, 8(12):4597–4602.

Sánchez-Royo, J. F., Muñoz-Matutano, G., Brotons-Gisbert, M., Martínez-Pastor, J. P., Segura, A., Cantarero, A., Mata, R., Canet-Ferrer, J., Tobias, G., Canadell, E., et al. (2014). Electronic structure, optical properties, and lattice dynamics in atomically thin indium selenide flakes. *Nano Research*, 7(10):1556–1568.

Savchyn, V. and Stakhira, J. (1996). Cathodoluminescence studies of thermally oxidized cleaved surfaces of gallium selenide layered crystals. *physica status solidi (a)*, 156(1):113–118.

Schafhaeutl, C. (1840). Ueber die Verbindungen des Kohlenstoffes mit Silicium, Eisen und andern Metallen, welche die verschiedenen Arten von Gusseisen, Stahl und Schmiedeeisen bilden. *Journal für praktische Chemie*, 19(1):159–174.

Schorer, L., Schmitz, S., and Weber, A. (2019). Membrane based purification of hydrogen system (MEMPHYS). *International Journal of Hydrogen Energy*, 44(25):12708–12714.

Shafique, A., Samad, A., and Shin, Y.-H. (2017). Ultra low lattice thermal conductivity and high carrier mobility of monolayer SnS_2 and $SnSe_2$: a first principles study. *Physical Chemistry Chemical Physics*, 19(31):20677–20683.

Sheng, Y., Tan, H., Wang, X., and Warner, J. H. (2017). Hydrogen addition for centimeter-sized monolayer tungsten disulfide continuous films by ambient pressure chemical vapor deposition. *Chemistry of Materials*, 29(11):4904–4911.

Shubina, T., Desrat, W., Moret, M., Tiberj, A., Briot, O., Davydov, V. Y., Platonov, A., Semina, M., and Gil, B. (2019). InSe as a case between 3D and 2D layered crystals for excitons. *Nature communications*, 10(1):1–8.

Sneed, M. C. and Brasted, R. C. (1958). *Comprehensive Inorganic Chemistry*, volume 7. D. Van Nostrand.

Srinivas, G., Zhu, Y., Piner, R., Skipper, N., Ellerby, M., and Ruoff, R. (2010). Synthesis of graphene-like nanosheets and their hydrogen adsorption capacity. *Carbon*, 48(3):630–635.

Sriv, T., Kim, K., and Cheong, H. (2018). Low-frequency Raman spectroscopy of few-layer 2H-SnS_2. *Scientific Reports*, 8(1):1–7.

Stoicheff, B. (1957). High resolution Raman spectroscopy of gases: IX. Spectra of H_2, HD, and D_2. *Canadian Journal of Physics*, 35(6):730–741.

Strocov, V. (2003). Intrinsic accuracy in 3-dimensional photoemission band mapping. *Journal of Electron Spectroscopy and related phenomena*, 130(1-3):65–78.

Sugiyama, M., Shimizu, T., Kawade, D., Ramya, K., and Ramakrishna Reddy, K. (2014). Experimental determination of vacuum-level band alignments of sns-based solar cells by photoelectron yield spectroscopy. *Journal of Applied Physics*, 115(8):083508.

Sun, P., Yang, Q., Kuang, W., Stebunov, Y., Xiong, W., Yu, J., Nair, R. R., Katsnelson, M., Yuan, S., Grigorieva, I., et al. (2020). Limits on gas impermeability of graphene. *Nature*, 579(7798):229–232.

Sun, Q., Wang, J., Hao, J., Zheng, S., Wan, P., Wang, T., Fang, H., and Wang, Y. (2019). SnS_2/SnS p-n heterojunctions with an accumulation layer for ultrasensitive room-temperature NO_2 detection. *Nanoscale*, 11(29):13741–13749.

Sun, Y., Luo, S., Zhao, X.-G., Biswas, K., Li, S.-L., and Zhang, L. (2018). InSe: a two-dimensional material with strong interlayer coupling. *Nanoscale*, 10(17):7991–7998.

Susoma, J., Lahtinen, J., Kim, M., Riikonen, J., and Lipsanen, H. (2017). Crystal quality of two-dimensional gallium telluride and gallium selenide using Raman fingerprint. *Aip Advances*, 7(1):015014.

Sutter, P., Komsa, H.-P., Krasheninnikov, A., Huang, Y., and Sutter, E. (2017). Luminescence of defects in the structural transformation of layered tin dichalcogenides. *Applied Physics Letters*, 111(26):262102.

Tashie-Lewis, B. C. and Nnabuife, S. G. (2021). Hydrogen production, distribution, storage and power conversion in a hydrogen economy-a technology review. *Chemical Engineering Journal Advances*, 8:100172.

Tedeschi, D., Blundo, E., Felici, M., Pettinari, G., Liu, B., Yildrim, T., Petroni, E., Zhang, C., Zhu, Y., Sennato, S., et al. (2019). Controlled Micro/Nanodome Formation in Proton-Irradiated Bulk Transition-Metal Dichalcogenides. *Advanced Materials*, 31(44):1903795.

Van de Walle, C. G. and Neugebauer, J. (2006). Hydrogen in semiconductors. *Annu. Rev. Mater. Res.*, 36:179–198.

Vidal, J., Lany, S., d'Avezac, M., Zunger, A., Zakutayev, A., Francis, J., and Tate, J. (2012). Band-structure, optical properties, and defect physics of the photovoltaic semiconductor SnS. *Applied Physics Letters*, 100(3):032104.

Wagner, C., Naumkin, A., Kraut-Vass, A., Allison, J., Powell, C., and Rumble Jr, J. (2003). NIST standard reference database 20, Version 3.4 (Web version). *National Institute of Standards and Technology: Gaithersburg, MD*, 20899.

Wang, S., Wang, W., Fong, W., Yu, Y., and Surya, C. (2017). Tin compensation for the sns based optoelectronic devices. *Scientific reports*, 7(1):1–10.

Wang, T., Li, J., Zhao, Q., Yin, Z., Zhang, Y., Chen, B., Xie, Y., and Jie, W. (2018). High-quality GaSe single crystal grown by the Bridgman method. *Materials*, 11(2):186.

Watanabe, K., Uchida, K., and Miura, N. (2003). Magneto-optical effects observed for gase in megagauss magnetic fields. *Physical Review B*, 68(15):155312.

Watts, J. F. and Wolstenholme, J. (2019). *An introduction to surface analysis by XPS and AES*. John Wiley & Sons.

Weng, Q., Li, G., Feng, X., Nielsch, K., Golberg, D., and Schmidt, O. G. (2018). Electronic and optical properties of 2D materials constructed from light atoms. *Advanced Materials*, 30(46):1801600.

Whittles, T. J., Burton, L. A., Skelton, J. M., Walsh, A., Veal, T. D., and Dhanak, V. R. (2016). Band alignments, valence bands, and core levels in the tin sulfides SnS, SnS_2, and Sn_2S_3: experiment and theory. *Chemistry of Materials*, 28(11):3718–3726.

Wickramaratne, D., Zahid, F., and Lake, R. K. (2014). Mexican hat and rashba bands in few-layer van der waals materials. *arXiv preprint arXiv:1412.2090*.

Xia, J., Li, X.-Z., Huang, X., Mao, N., Zhu, D.-D., Wang, L., Xu, H., and Meng, X.-M. (2016). Physical vapor deposition synthesis of two-dimensional orthorhombic SnS flakes with strong angle/temperature-dependent Raman responses. *Nanoscale*, 8(4):2063–2070.

Xiao, Z., Ran, F.-Y., Liao, M., Hiramatsu, H., Ide, K., Hosono, H., and Kamiya, T. (2018). Multiple states and roles of hydrogen in p-type SnS semiconductors. *Physical Chemistry Chemical Physics*, 20(32):20952–20956.

y Blancá, E. P., Svane, A., Christensen, N., Rodriguez, C., Cappannini, O., and Moreno, M. (1993). Calculated static and dynamic properties of β-Sn and Sn-O compounds. *Physical Review B*, 48(21):15712.

Yang, Q., Tang, K., Wang, C., Zhang, D., and Qian, Y. (2002). The synthesis of SnS_2 nanoflakes from tetrabutyltin precursor. *Journal of Solid State Chemistry*, 164(1):106–109.

Yang, R., Zhang, L., Wang, Y., Shi, Z., Shi, D., Gao, H., Wang, E., and Zhang, G. (2010). An anisotropic etching effect in the graphene basal plane. *Advanced Materials*, 22(36):4014–4019.

Yang, Z., Wang, X., Felton, J., Kudrynskyi, Z., Gen, M., Nomura, T., Wang, X., Eaves, L., Kovalyuk, Z. D., Kohama, Y., et al. (2021). Heavy carrier effective masses in van der Waals semiconductor Sn (SeS) revealed by high magnetic fields up to 150 T. *Physical Review B*, 104(8):085206.

Zappia, M. I., Bianca, G., Bellani, S., Serri, M., Najafi, L., Oropesa-Nuñez, R., Martín-García, B., Bouša, D., Sedmidubskỳ, D., Pellegrini, V., et al. (2020). Solution-Processed GaSe Nanoflake-Based Films for Photoelectrochemical Water Splitting and Photoelectrochemical-Type Photodetectors. *Advanced Functional Materials*, 30(10):1909572.

Zhang, Y., Rubio, A., and Le Lay, G. (2017). Emergent elemental two-dimensional materials beyond graphene. *Journal of Physics D: Applied Physics*, 50(5):053004.

Zhao, Q., Frisenda, R., Gant, P., Perez de Lara, D., Munuera, C., Garcia-Hernandez, M., Niu, Y., Wang, T., Jie, W., and Castellanos-Gomez, A. (2018). Toward air stability of thin GaSe devices: avoiding environmental and laser-induced degradation by encapsulation. *Advanced Functional Materials*, 28(47):1805304.

Zhao, Q., Frisenda, R., Wang, T., and Castellanos-Gomez, A. (2019). InSe: a two-dimensional semiconductor with superior flexibility. *Nanoscale*, 11(20):9845–9850.

Zhirko, Y. I., Kovalyuk, Z., Pyrlja, M., and Boledzyuk, V. (2007). Application of layered InSe and GaSe crystals and powders for solid state hydrogen storage. In *Hydrogen Materials Science and Chemistry of Carbon Nanomaterials*, pages 325–340. Springer.

Zhuang, H. L. and Hennig, R. G. (2013a). Single-layer group-III monochalcogenide photocatalysts for water splitting. *Chemistry of Materials*, 25(15):3232–3238.

Zhuang, H. L. and Hennig, R. G. (2013b). Theoretical perspective of photocatalytic properties of single-layer SnS_2. *Physical Review B*, 88(11):115314.

Zou, M., Ma, Y., Yuan, X., Hu, Y., Liu, J., and Jin, Z. (2018). Flexible devices: from materials, architectures to applications. *Journal of Semiconductors*, 39(1):011010.